Space Sci Rev (2007) 132: 433–509
DOI 10.1007/s11214-007-9232-0

Processes that Promote and Deplete the Exosphere of Mercury

Rosemary Killen · Gabrielle Cremonese · Helmut Lammer · Stefano Orsini · Andrew E. Potter · Ann L. Sprague · Peter Wurz · Maxim L. Khodachenko · Herbert I.M. Lichtenegger · Anna Milillo · Alessandro Mura

Received: 2 February 2007 / Accepted: 5 June 2007 / Published online: 30 October 2007

Abstract It has been speculated that the composition of the exosphere is related to the composition of Mercury's crustal materials. If this relationship is true, then inferences regarding the bulk chemistry of the planet might be made from a thorough exospheric study. The most vexing of all unsolved problems is the uncertainty in the source of each component. Historically, it has been believed that H and He come primarily from the solar wind (Goldstein, B.E., et al. in J. Geophys. Res. 86:5485–5499, 1981), Na and K come from volatilized materials partitioned between Mercury's crust and meteoritic impactors (Hunten, D.M., et al. in Mercury, pp. 562–612, 1988; Morgan, T.H., et al. in Icarus 74:156–170, 1988; Killen, R.M., et al. in Icarus 171:1–19, 2004b). The processes that eject atoms and molecules into the exosphere of Mercury are generally considered to be thermal vaporization, photon-stimulated desorption (PSD), impact vaporization, and ion sputtering. Each of these processes has its own temporal and spatial dependence. The exosphere is strongly influenced by Mercury's highly elliptical orbit and rapid orbital speed. As a consequence the surface undergoes large

---

R. Killen (✉)
Department of Astronomy, University of Maryland, College Park, USA
e-mail: rkillen@astro.umd.edu

G. Cremonese
Osservatorio Astronomico-INAF, Padova, Italy

H. Lammer · M.L. Khodachenko · H.I.M. Lichtenegger
Space Research Institute, Austrian Academy of Sciences, Graz, Austria

S. Orsini · A. Milillo · A. Mura
Istituto di Fisica dello Spazio Interplanetario-CNR, Rome, Italy

A.E. Potter
National Solar Observatory, Tucson, AZ, USA

A.L. Sprague
Lunar and Planetary Laboratory, University of Arizona, Tucson, USA

P. Wurz
Physics Institute, University of Bern, Bern, Switzerland

fluctuations in temperature and experiences differences of insolation with longitude. Because there is no inclination of the orbital axis, there are regions at extreme northern and southern latitudes that are never exposed to direct sunlight. These cold regions may serve as traps for exospheric constituents or for material that is brought in by exogenic sources such as comets, interplanetary dust, or solar wind, etc. The source rates are dependent not only on temperature and composition of the surface, but also on such factors as porosity, mineralogy, and space weathering. They are not independent of each other. For instance, ion impact may create crystal defects which enhance diffusion of atoms through the grain, and in turn enhance the efficiency of PSD. The impact flux and the size distribution of impactors affects regolith turnover rates (gardening) and the depth dependence of vaporization rates. Gardening serves both as a sink for material and as a source for fresh material. This is extremely important in bounding the rates of the other processes. Space weathering effects, such as the creation of needle-like structures in the regolith, will limit the ejection of atoms by such processes as PSD and ion-sputtering. Therefore, the use of laboratory rates in estimates of exospheric source rates can be helpful but also are often inaccurate if not modified appropriately. Porosity effects may reduce yields by a factor of three (Cassidy, T.A., and Johnson, R.E. in Icarus 176:499–507, 2005). The loss of all atomic species from Mercury's exosphere other than H and He must be by non-thermal escape. The relative rates of photoionization, loss of photo-ions to the solar wind, entrainment of ions in the magnetosphere and direct impact of photo-ions to the surface are an area of active research. These source and loss processes will be discussed in this chapter.

Keywords Mercury · Exosphere · Surface composition · Particle release processes

1 Observations of the Mercury Exosphere

Early ground-based efforts to detect an atmosphere on Mercury were unsuccessful, leading only to successively smaller upper limits for the atmospheric density. The first real information about the Mercury atmosphere came with the Mariner 10 flybys (Broadfoot et al. 1976). Atomic hydrogen, helium and atomic oxygen were detected by the Mariner 10 ultraviolet photometers from sunlight scattered from these atoms.

A comprehensive discussion of the Mariner 10 measurements is given in "The Mercury Atmosphere" by Hunten et al. (1988), and the reader is referred to this source for details. Subsolar point densities were estimated at 6,000 atoms/cm^3 for helium, and 230 atoms/cm^3 for the thermal component of atomic hydrogen. A nonthermal component of hydrogen with a scale height of about 70 kilometers was observed near the limb above the subsolar point, providing a total number density of 23 atoms/cm^3 at the surface. Atomic oxygen was detected in the third flyby at a level of 44,000 atoms/cm^3, the number being dependent on the assumed scale height. This chapter is concerned with Mercury atmospheric observations made after the Mariner 10 flybys, all from ground-based observations.

1.1 Sodium in Mercury's Exosphere

In 1985, Drew Potter and Tom Morgan were at the McDonald Observatory of the University of Texas measuring the spectrum of light reflected from the Moon. They were looking for the "filling-in" of reflected solar lines caused by interactions of solar radiation with the lunar surface. It occurred to them that Mercury was similar in many ways to the Moon, and should show similar "filling-in" effects. The first solar lines they observed on Mercury were

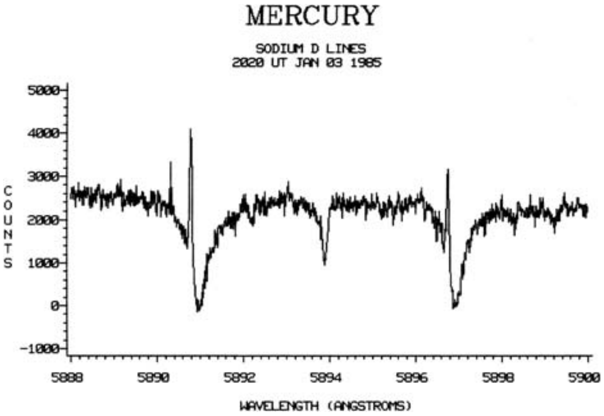

Fig. 1 Sodium discovery spectrum showing D_1 and D_2 sodium resonance emission lines within the solar Fraunhofer absorption lines reflected from the Mercury surface. Measured at the Harlan Smith telescope at the McDonald Observatory of the University of Texas

the pair of sodium Fraunhofer lines at 5,890 and 5,896 angstroms. They were astonished to find that the spectra of these features showed bright emission lines that extended well above the continuum. The wavelengths of the lines identified them as resonance scattering lines of sodium in the exosphere of Mercury. The discovery spectrum is shown in Fig. 1 (Potter and Morgan 1985).

The calculation of sodium column content from the spectra first requires that the emission intensity be extracted from the combination of surface reflection and sodium atom emission. The common practice has been to interpolate the solar Fraunhofer continuum from one side of the emission to the other, and subtract it to obtain the sodium emission line. Procedures that fit the Fraunhofer absorption line with a combination of Voigt profiles give the best results for defining the Fraunhofer background to be subtracted. However, Hunten and Wallace (1993) pointed out that this procedure underestimates the sodium emission, since about a fifth of the sodium light is hidden in a depression in the continuum caused from extinction by the sodium atoms.

Once the sodium emission intensity is determined, two methods have been used to calculate the column content of sodium atoms. The ratio of D_2 to D_1 emissions is a function of both temperature and the column content of sodium and the surface albedo (e.g. Killen 2006), so by assuming a value for temperature, the column content can be calculated from the ratio. This procedure was used to estimate the column content of sodium atoms in the discovery spectrum. However, this procedure is subject to large uncertainties. A better method is to use the planet itself as a “standard candle” to calibrate the sodium emission, since the solar continuum reflected from the planetary surface is available in each spectrum. The reflectance of Mercury can be calculated using the Hapke formulation for reflectivity with the optical constants for the Mercury surface. (The most recent set of optical constants was provided by Mallama et al. (2002).) It is then necessary to take into account the effect of atmospheric blurring of the Mercury image, which reduces the surface brightness as seen by ground-based observers.

Since the discovery of sodium emission, there have been a number of additional observations. Table 1 shows a summary of the observations that have been reported to date. These observations show that average sodium column densities computed from emission spectra seen above the planetary surface range between $1\text{–}10 \times 10^{11}$ atoms/cm^2. Column densities measured from absorption spectra seen during solar transit are smaller, in the range $1\text{–}3 \times 10^{10}$. However, these densities are measured at the evening terminator, where sodium densities are normally seen to be small.

Table 1 Column densities of sodium in the Mercury exosphere

Observer	Column content, atoms/cm^2	Remarks
	$8.1 \pm 1.0 \times 10^{11}$*	Slit spectra
Potter and Morgan (1987)	$1.9 \pm 1.4 \times 10^{11}$	Slit spectra
Potter and Morgan (1985)	$2.8–3.8 \times 10^{11}$	Slit spectra
Potter and Morgan (1997)	$4.4–6.0 \times 10^{11}$	$5'' \times 5''$ image slicer, peak values
Sprague et al. (1997)	Min. $<1 \times 10^{10}$ equatorial	Slit spectra
	Max. 15.0×10^{11}	Slit spectra
	Avg. $1.20 \pm 1.49 \times 10^{11}$	Slit spectra
Sprague et al. (1998)	8.6×10^{11}	Northern spot, slit spectra
	8.0×10^{11}	Southern spot, slit spectra
Potter et al. (1999)	$0.84 \times 2.9 \times 10^{11}$	$10'' \times 10''$ image slicer, average values
Barbieri et al. (2004)	$0.43–1.97 \times 10^{11}$	Slit spectra
		Scanning Fabry Perot
Schleicher et al. (2004)	$3.4 \pm 0.1 \times 10^{10}$	North pole
		Scanning Fabry Perot
	$3.0 \pm 0.1 \times 10^{10}$	South pole
		Scanning Fabry Perot
	$1.5 \pm 0.1 \times 10^{10}$	West equatorial
		Scanning Fabry Perot
	$<0.2 \times 10^{10}$	East equatorial
		Scanning Fabry Perot
Leblanc et al. (2006)		Slit spectra, terminator low, solar limb high
Potter et al. (2007)	$1.5–3.5 \times 10^{11}$	$10'' \times 10''$ image slicer, average values**

*Calibration from D_2/D_1 ratio. Other observations, except Schleicher et al. (2004), were calibrated from the Mercury reflectance signal

**Sodium seen in absorption. Column content derived from equivalent width

***Average values from 10 × 10 arc second slicer were scaled to the approximate area of planet

1.2 Temperature of the Sodium Exosphere

The velocity distribution of sodium atoms in the exosphere is an important indicator of the source of the sodium. Source processes such as photon-stimulated desorption and ion sputtering will produce non-Maxwellian velocity distributions (e.g. Madey et al. 1998). Subsequent interaction of the atoms with the surface can relax the distribution back towards Maxwellian. Thus, analysis of the velocity distribution can provide information on source

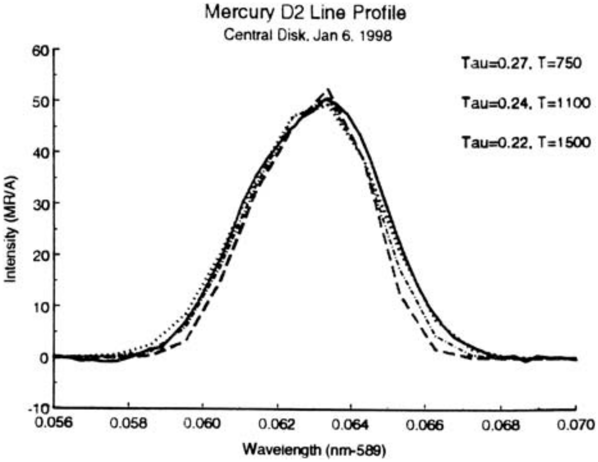

Fig. 2 The sodium D_2 line profile for the central disk of Mercury observed with the Anglo-Australian telescope on January 6, 1998 (*solid line*). A 1,500 K Maxwellian velocity distribution is plotted as a dotted line, an 1,100 K distribution is plotted as a *dot-dash line*, and a 750 K distribution is plotted as a *long-dash line*. The best fit to the line profile is given by the 1,500 K distribution (Killen et al. 1999)

processes and surface interactions. The measurable quantity that is related to the velocity distribution is the spectral profile of the emission line, which can be compared with line profiles computed assuming combinations of Gaussian velocity profiles for the atomic transitions. An initial effort was reported by Potter and Morgan (1987), who obtained a somewhat noisy line profile of the sodium D_2 emission at a dispersion of 7.2 mÅ per step. They concluded that the half-width of the line was consistent with a thermalized gas at a temperature of 500 K. A subsequent analysis that took into account the wings of the line emission suggested that the line profile was better fit by a temperature of about 1,000 K (Shemansky and Morgan 1991). Measurements at higher resolution and better signal-to-noise were reported by Killen et al. (1999). Line profiles were measured at the McDonald Observatory of the University of Texas at a dispersion of 1.98 mA per step, and at the Anglo-Australian Telescope (AAT) at Coonabarabran, Australia at a dispersion of 3.14 mÅ per step. The line profiles from the AAT were fit assuming a Chamberlain-type exosphere, summing the Gaussian line profiles for each of the hyperfine levels of the sodium resonance transition. An example showing three trial fits to the line profile of the central disk of Mercury observed is shown in Fig. 2.

The best fit to the central disk profile was given by assuming a 1,500 K Maxwellian velocity distribution. Line profiles from above the north and south pole were best fit by a 750 K gas. In all cases, the gas temperature appeared to be everywhere hotter than the surface temperature by 600–700 K. The importance of high signal-to-noise is evident in this plot, where the differences between profiles for different temperatures are small, becoming evident only in the wings of the emission profile.

Another approach to measuring the velocity profile is to measure the altitude distribution of the atoms. The observations by Schleicher et al. (2004) of Mercury in transit across the Sun measured the altitude distribution of sodium above the terminator. These data provide direct measures of scale heights and consequently temperatures. They also measured the width of the absorption line, finding that it corresponded to a Doppler temperature of 3,540 K. This apparent high temperature might be the consequence of sputtering over the polar regions and/or radiation acceleration, since the view of sodium atoms during a transit is such that velocity changes caused by radiation acceleration should be detectable (Potter et al. 2007). Their results are compared with the line profile estimates of scale height and temperature shown in Table 2. The temperatures from line profiles and estimated altitude distributions are in fair agreement near the center of the planet, but differ considerably at

Table 2 Temperatures and scale heights for the Mercury sodium exosphere

Observer/author	Location	Temperature, K
Shemansky and Morgan (1991)	Planetary average	1000
Killen et al. (1999)	North polar region	750
	Center	1500
	South polar region	750
Schleicher et al. (2004)	North polar region	1380 ± 307
	South polar region	1330 ± 307
	West edge	1540
	East edge	1540
	Planetary average	1540

the poles. The temperatures from altitude distribution are almost twice those derived from line profile data. The difference might be the result of slight differences in location of the observations near the poles.

The high temperature sodium absorptions in the polar regions reported by Schleicher et al. (2004) were at a maximum in regions offset towards the dawn terminator by about 15 degrees. In polar regions, 15 degrees *away* from the dawn terminator, the altitude distribution is much shorter, and the temperature is obviously much lower. Consequently, the AAT and transit observations may not have viewed the same regions of the exosphere near the poles, and temporal variations are certainly important. Recalling that the subsolar surface temperature of Mercury is about 700 K, and polar temperatures are much lower, the results summarized in Table 2 show that sodium is produced by an energetic process, and is not completely thermally accommodated. A planet-wide average temperature of 1,000 K for sodium corresponds to a scale height of about 97 km. For this scale height, the surface concentrations of sodium derived from the column densities of Table 1 would be in the range 1–10 × 10^4 atoms/cm^3.

1.3 Spatial Variation of Sodium Emission

One of the first things that investigators of the sodium emission noticed was that it was not uniform over the surface of Mercury and did not conform to the distribution expected for a classical exosphere. This is illustrated in Fig. 3 by profiles of the sodium emission across the planet taken with a slit spectrograph (Potter et al. 2006).

A similar set of profiles for the period April 3–6, 1988, were analyzed by Killen et al. (1990) using radiative transfer theory to make profiles of simple smooth models of a uniform exosphere. The observations could not be fit by these models. Compared to the models, the observed sodium emissions were concentrated in the sunward direction with polar enhancements. Several north–south distributions showed more sodium at the north polar regions than could be explained by a simple model. Furthermore, the distribution changed noticeably from one day to the next.

1.4 North–south Emission Peaks

Two-dimensional images of sodium distribution over the surface were obtained by Potter and Morgan (1990), using a 5″ × 5″ (arcsec) image slicer. Images from two different

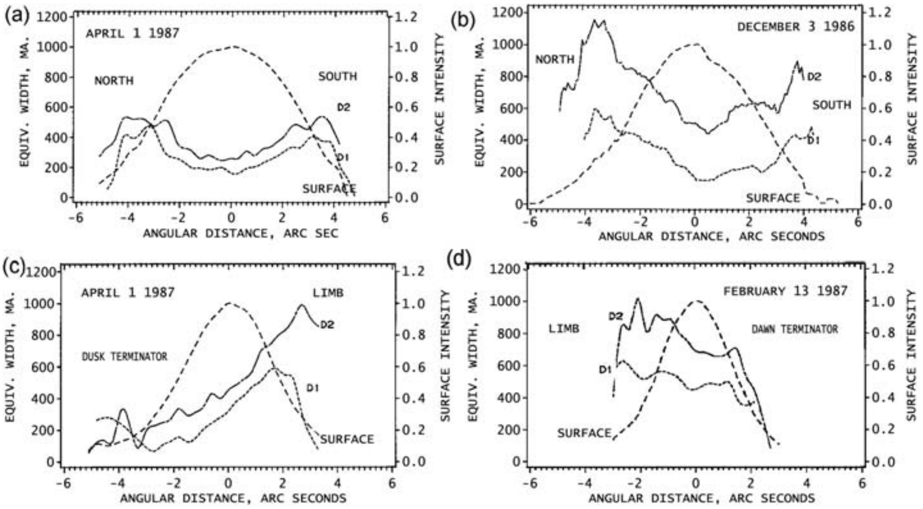

Fig. 3 Profiles of sodium emission (*solid lines*) and surface continua (*dotted lines*) across Mercury. The upper left profile (**a**) from April 1, 1987, shows symmetric limb brightening at the north and south polar regions. At the *upper right* (**b**), there is a north–south profile from December 3, 1986, that shows excess emission in the north polar region. At the *lower left* (**c**), there is a profile that starts at the dusk terminator and proceeds to the bright limb. Sodium emission is effectively nonexistent at the dusk terminator, in contrast to the *lower right profile* (**d**), which shows a terminator-to-limb profile for the case that the dawn terminator is in view. Here, the sodium emission decreases only about 30% as the terminator is approached

Fig. 4 Maps of the sodium D_2 emission from Mercury on July 7, and August 23, 1989

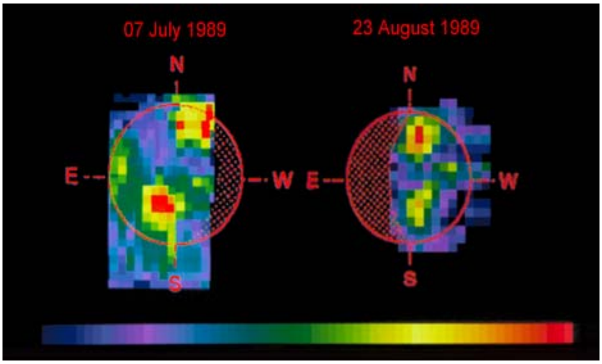

dates (July 7, 1989, and August 23, 1989) are shown in Fig. 4. These maps confirmed the long slit observations that the sodium is not distributed uniformly over the surface. Excess sodium emission was seen at both polar regions, plus some excess sodium near the subsolar point. Almost all the maps showed north–south excess sodium, and a sequence of three images from July 16–18, 1989, showed variations from one day to the next. The combination of north–south excess sodium emission and daily variability suggested to the authors that sodium was produced, at least in part, by sputtering at high latitudes by solar wind particles precipitated to the surface in the cusps of the magnetosphere.

The images shown in Fig. 4 view approximately opposite sides of the planet. Both images show emission peaks at north and south high latitudes and a smaller peak in the vicinity of the subsolar point. The peak values of sodium emission are 3.8 MR and 1.2 MR, respectively. The difference in peak intensity between the two images is due in large part to the difference of radial velocity. The July image was taken at a time when the radial velocity was about −4.7 km/sec, while the August image was taken near aphelion, when the radial velocity was about 0.69 km/sec. The peak values of atomic sodium density in the two images are similar. The images were made using a 5″ × 5″ image slicer having 0.5″ slices to yield 5 arc second square images, each having 10 × 10 pixels of 0.5″. To cover the whole planet, two such images offset from one another were combined, registered to one another by matching the surface reflection signals. The directions shown in this figure are those seen by a ground-based observer, and the terminator is the dusk terminator for the July image, and the dawn terminator for the August image.

The July image displays longitudes in the range from 270° (terminator) to 360° and 0° to 47° (limb). This range includes the high latitude radar- and optical-bright albedo spots B (north) and A (south) (reported by Slade et al. 1992; Butler et al. 1993; Harmon 1997), as well as the relatively freshly excavated Kuiper-Murasaki crater complex on the eastern limb. There is excess sodium in the vicinity of these features. The August image displays longitudes in the range 71° (limb) to 175° (terminator), approximately the opposite side of the planet from the July image. The sodium-bright spot pattern is similar to that seen for the July image, but there are no obvious anomalous geographic features in this case, other than the far eastern edge of Caloris Basin.

Sprague et al. (1997) made an extensive series of Mercury sodium measurements using a long-slit spectrograph. The slit provided three to five spatial resolution elements across the planet and, by stepping the slit across the planet, they were able to obtain low-resolution maps. They found that high-latitude enhancements of sodium emission were common, with the added characteristic that there was usually more at one hemisphere than the other. They observed notable sodium enhancements when the spectrograph slits were placed over the radar-bright spots B and A which are centered near at 355°W longitude and 55°N and 25°S latitude, respectively. In a repetition of the measurements on October 4, 1996, they again found sodium enhancements at the approximate locations of the radar-bright spots (Sprague et al. 1998). They also observed an exceptionally high emission value, corresponding to a column content of 15×10^{11} atoms/cm^2 at a location close to the Caloris Basin. Similar enhancements close to these locations were also observed by Potter and Morgan (1990), and the sodium map for July 7, 1989, shown in Fig. 4 includes the region of the radar-bright spots. Sprague et al. (1994, 1993) proposed that these sodium-bright spots were the result of a special quality of the radar-bright regions and Caloris Basin—most likely a surface composition rich in sodium as the result of geologic processes.

Potter et al. (2006) used a 10 × 10 element image slicer having 1″ slices to produce 10″ × 10″ images with 1″ pixels. Many of the images showed high latitude emission enhancements in one hemisphere relative to the other, and many showed enhancements in both hemispheres. The ratio of north to south hemispheric emission intensity was calculated for each image and the results are plotted in Fig. 5 as a function of the longitude of the center of the surface reflection image. The ratios appear to be random with respect to longitude, and there is no concentration of excess sodium emission in the northern hemisphere near the longitude of the Caloris Basin centered at latitude 22° north and longitude W 180°.

A correlation of high or low ratios shown in Fig. 5 with any specific longitude would suggest that specific sodium-rich areas of the planet were responsible for excess sodium at that longitude. However, there do not appear to be any strong correlations with specific longitudes. Images in which bright spots appeared in both hemispheres were of special interest in view of the possibility that the north–south radar-bright spots are sources of sodium

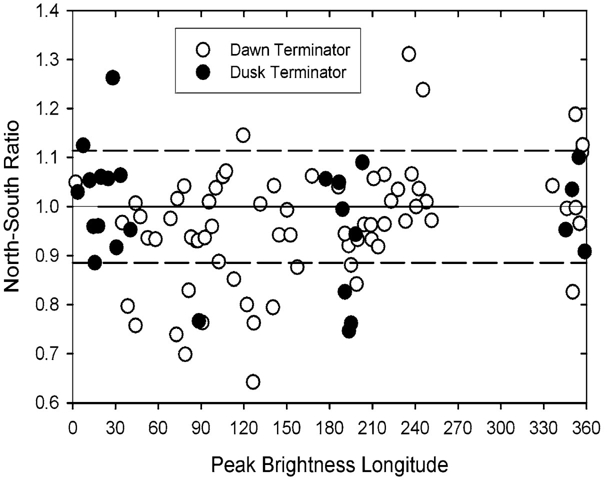

Fig. 5 Ratios of the northern hemisphere emission to the southern hemisphere emission plotted against longitude of peak brightness in the continuum reflection image

Table 3 Sodium images that show bright symmetric north–south emission peaks (Potter et al. 2006)

Date	Terminator	True anomaly, degrees	Radiation acceleration, cm/sec^2	Terminator longitude, degrees	Bright limb longitude, degrees
Aug. 31, 1999	Dusk	39.4	166.9	270.1	65.0
Feb. 6, 2000	Dawn	315.9	170.6	89.0	320.5
May 30, 2000	Dawn	81.5	157.8	281.1	181.0
Jun. 3, 2000	Dawn	98.4	135.1	289.9	200.7
Jan. 6, 2002	Dawn	297.7	172.2	85.3	325.0
Nov. 6, 2001	Dusk	68.8	173.1	96.2	225.7
Apr. 9, 2003	Dawn	113.4	113.4	269.3	162.6

emission. A selection of images from Potter et al. (2006) that showed bright spots in both hemispheres is listed in Table 3. For three of the observations listed in Table 3 (Aug. 31, 1999, Feb. 6, 2000, and Jun. 6, 2000) the radar-bright spots at 355° longitude are in view.

However, they are not in view for the remaining four observations. These images shared high values of solar radiation acceleration and, in fact, images measured at high values of radiation acceleration almost always showed bright spots in both hemispheres. Ip (1990) modeled the effect of radiation acceleration on the planetary sodium distribution, and showed that high values of radiation acceleration would push sodium towards the terminator. At the poles, the terminator and bright limb meet, so that at the poles, we expect to see limb brightening enhanced by sodium pushed to the terminator by radiation acceleration.

North–south excess sodium has also been observed in absorption against the Sun. Schleicher et al. (2004) observed the sodium D_2 line in absorption against the surface of the Sun during the transit of 2003. As shown in Fig. 6, sodium absorptions were observed at high northern and southern latitudes, in agreement with all the emission observations that find high latitude concentrations of sodium. This was the case despite the fact that radiation acceleration was not high, about 13.2% of surface gravity. Sodium absorption is observed along the western equatorial region, but not along the eastern equatorial region. It is puz-

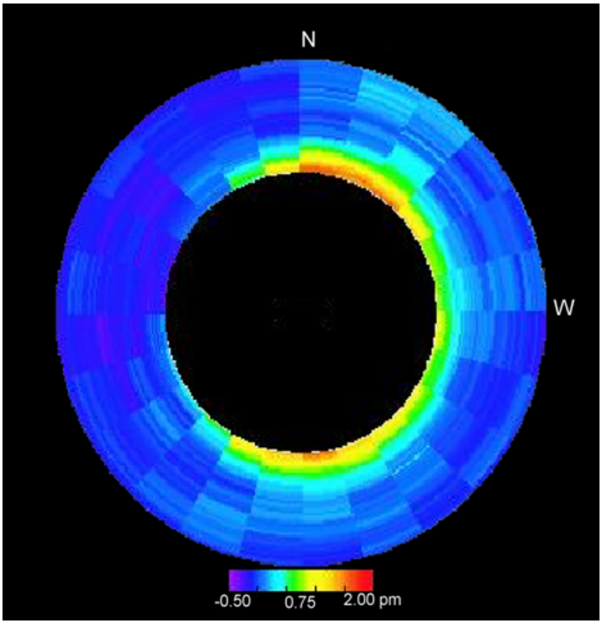

Fig. 6 Distribution of sodium D_2 absorption around the disk of Mercury seen in transit across the Sun. Concentrations of sodium vapor exist at high north and south latitudes. Sodium absorption is seen along the west equatorial limb (dawn), but not along the east equatorial limb (dusk). The true anomaly angle was 149.2° and radiation acceleration was 49.3 cm/sec^2, or about 13.2% of surface gravity. Figure from Schleicher et al. (2004)

zling to note that almost no sodium is observed over most of the eastern half of the planet. Observations of sodium emission do not show much, if any, deficit of emission on the dusk hemisphere of the planet. The temperatures derived from the altitude distribution of the sodium absorption are listed in Table 2.

Conclusions from this discussion are: (1) Excess sodium emissions often appear in either the northern or southern hemisphere, usually both. Sometimes they appear over the bright-albedo regions A and B. (2) Near the peak values for radiation acceleration, symmetric north–south spots tend to appear, which may be the result of the pile-up of sodium near the terminator pushed there by radiation acceleration. (3) North–south excess emissions sometimes appear even when radiation acceleration is relatively low (see Fig. 4). In addition to radiation acceleration effects, causes suggested for the appearance of sodium-bright spots include sodium-rich areas and high-latitude sputtering effects.

1.5 Diurnal Variation of Sodium Distribution

Sprague et al. (1997) reported a diurnal variation in sodium emission, such that the sodium abundance increased as the sunrise terminator was approached. This is illustrated in Fig. 7 (Fig. 4b from Sprague et al. 1997), where a bar chart shows the average sodium column abundance as a function of Mercury's local time. Bin 1 = early morning, 2 = mid-morning, 3 = mid day, 4 = mid afternoon, 5 = late afternoon. By mid- and late- afternoon the Na abundance is down by close to a factor of 3. Sprague et al. (1997) proposed that this effect results from evaporation of cold-trapped and ion implanted Na that is released as the sun rises and heats the surface of Mercury.

The ratio of terminator to limb emission over a range of true anomaly angles was reported by Potter et al. (2006). To calculate this ratio, sodium emission on the terminator side of the image was summed, and divided by the sum of sodium emission on the limb side of the image. For terminator-to-limb distributions where the emission falls to low values at

Fig. 7 The variation of sodium column content is shown at hourly intervals past sunrise (Fig. 4b from Sprague et al. 1997). This bar chart shows that the column content of sodium in bins of Mercury's local time: bin *1* = early morning, *2* = mid-morning, *3* = mid day, *4* = mid afternoon, *5* = late afternoon

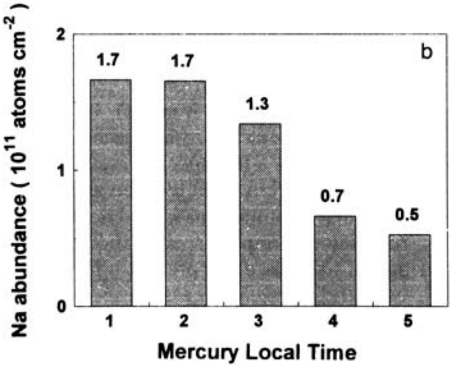

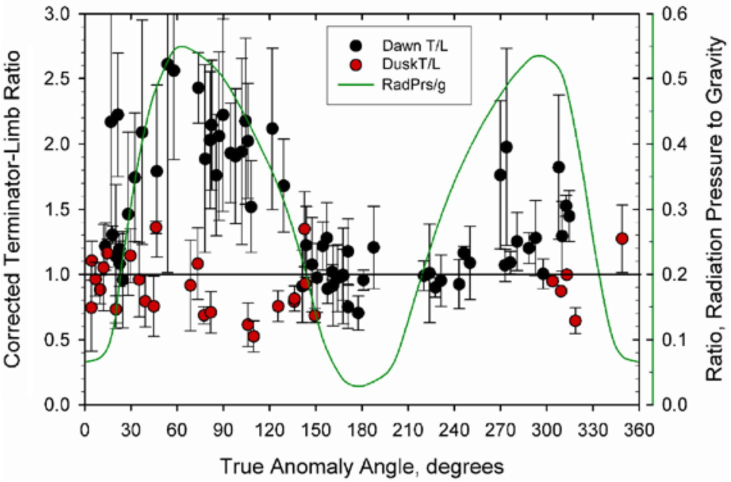

Fig. 8 The terminator-to-limb ratio variation with true anomaly angle is shown for cases when the dawn terminator is in view, and when the dusk terminator is in view Potter et al. (2006). The strength of solar radiation acceleration is plotted for comparison

the terminator (as seen in Fig. 3c), the terminator-to-limb ratio will be less than unity. For terminator-to-limb distributions where there is appreciable sodium at the terminator (as seen in Fig. 3d), the ratio will be unity or larger. Figure 8 shows a plot of this ratio against true anomaly angle. The ratio of radiation acceleration to surface gravity is also plotted.

For dawn-side observations on the "out" leg of the orbit, where true anomaly angles (TAA) $< 180°$, the ratios appear to be consistent with the hypothesis that dawn enhancement from evaporation of sodium occurs. The dawn-side ratio is larger than unity, indicating enhancement of sodium at the terminator. The dawn-side ratios are largest near maximum radiation acceleration. For values of TAA larger than 140°, the ratios for dawn-side observations drop down to near-unity values, coincident with the decrease of radiation acceleration. This change is inconsistent with evaporative enhancement of sodium near the terminator. It is reasonable to expect that the rate of evaporation of condensed sodium and hence the amount of sodium vapor near the terminator should depend on the rate of exposure of new surface at the terminator. In other words, the amount of excess sodium should depend on the rate of terminator advancement. The rate of terminator advancement is about -0.2 degrees/day at perihelion, rising to a maximum value of +3.38 degrees/day at aphelion. Consequently, one expects that the maximum amount of dawn enhancement should be found near aphelion, rather than near maximum radiation acceleration, but this does not occur. For the "in" leg of the orbit (TAA $> 180°$), the effect is much less pronounced. There are only a few dusk-side ratios. On average, the ratio values scatter around unity, with some below unity near maximum radiation acceleration.

Although some of the observations are consistent with the explanation that dawn enhancement occurs from evaporation of condensed sodium, it seems reasonable to expect that radiation acceleration could also play a role by pushing sodium towards the terminator, thus producing an excess of sodium there (see Ip 1990). This would explain why the effect is largest near maximum radiation acceleration.

The transit observations reported by Schleicher et al. (2004) (shown above in Fig. 6), found sodium emission clearly evident along the western equatorial region, which is the dawn terminator. Little or no sodium was visible along the dusk terminator on the eastern equatorial region. This observation is consistent with the existence of a dawn terminator enhancement of sodium vapor. Dawn/dusk asymmetries can also be caused by an asymmetric magnetosphere, with resulting asymmetric ion-sputtering and preferential re-implantation of photoions on the dawnside (Killen et al. 2004a).

1.6 Variation of Sodium Emission with Time

Sodium emissions sometimes vary in an apparently random fashion. An example was published by Potter and Morgan (1990), who observed the distribution of sodium over the planetary disk to change over a three-day period, from February 16 to 18, 1989. A bright spot appeared in the southern hemisphere on February 17, and disappeared the next day. The peak emission intensities rose from 2.2 MR on February 16 to 3.4 MR on February 17, and then dropped back to 2.2 MR on February 18.

Sprague et al. (1997) reported similar behavior. During the October 10–15, 1987 observing sequence, they saw a dramatic onset of north–south enhancement, followed by its total disappearance. The sodium abundance at high northern and southern latitudes exceeded equatorial values by a factor of 2 on October 14, while before and after this date, the abundance was similar at all latitudes.

Potter et al. (1999) reported observations of Mercury sodium over six days during the period November 13–20, 1997. Daily changes took place in both the total amount of sodium and its distribution over the planet. The cause of these variations is unknown, but their episodic nature suggests some connection with solar activity, or heating of the surface, both of which are known to change over short periods of time. Sprague et al. (1997) were unable to find any correlation between changes in sodium emission and the F10.7 cm solar radio flux. Likewise, Potter et al. (1999) found no correlation between the variations in their November 1997 data and F10.7 cm solar flux. They did note that there were a number of coronal mass ejection (CME) events at this time, some of which were directed towards the general area of Mercury, and suggested a possible connection with the changes observed on Mercury.

In addition to the random variations, there is a secular trend of sodium emission from one day to the next. This is illustrated in Fig. 9 (from Potter et al. 2007) which shows a plot of the planet-wide averaged emission intensity against true anomaly angle. The intensity is seen to change from day to day, mostly in a regular fashion, and is closely correlated to emission rate calculated for an individual sodium atom, caused by a variation in the continuum at the rest frequency of a sodium atom in the exosphere.

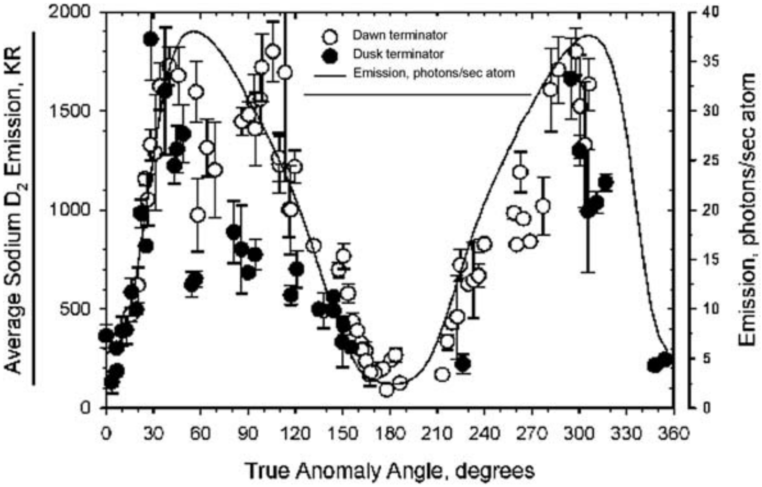

Fig. 9 The planetary average sodium emission was measured using a 10″ × 10″ image slicer over the period from 1997 to 2003, and is plotted here against the true anomaly angle. Depending on the true anomaly angle, the average sodium emission can change up to 20% per day. The calculated rate of emission from a single sodium atom is also shown in the plot (*solid line*)

The observed emission intensity shown in Fig. 9 tracks the calculated emission very well except for regions near maximum radiation acceleration. On the "out" leg of the orbit (TAA $< 180°$), there is a minimum just past the maximum acceleration at 50°. On the "in" leg of the orbit (TAA $> 180°$) there are deviations from the calculated curve both before and after the maximum radiation acceleration.

In large part, the secular changes of sodium emission intensity illustrated in Fig. 9 are the result of changes in the intensity of solar radiation in the rest frame of the sodium atoms as the radial velocity of Mercury changes.

However, changes in sodium column content also affect the emission intensity, and the deviations noted from the calculated emission curve may be due to changes in the sodium column content. By normalizing the emission intensities to a constant value of solar radiation intensity it is possible to separate the changes due to solar radiation from those due to sodium column content. Figure 10 shows the data from Fig. 9 normalized to the solar intensity seen by sodium atoms on Mercury at a true anomaly angle of 150.26°.

The maximum values of normalized emission, and hence of sodium column densities, occurs near perihelion and aphelion, where solar radiation acceleration effects are nearly negligible. In between perihelion and aphelion, there is a decrease of nearly a factor of three. The most likely cause for this decrease is the effect of radiation acceleration, which reaches a maximum as the normalized emission reaches a minimum, most clearly evident for the "out" leg of the orbit (TAA $< 180°$).

1.7 Effects of Radiation Acceleration on Sodium Emission

As noted in the previous paragraph, radiation acceleration appears to affect the amount of sodium visible on Mercury. Previous observations of the effect of radiation acceleration were inconsistent. Potter and Morgan (1987) found a decrease in column content as radiation acceleration increased. The average column content of sodium decreased by about 30% when the radiation acceleration relative to gravity increased from about 15% to 45%.

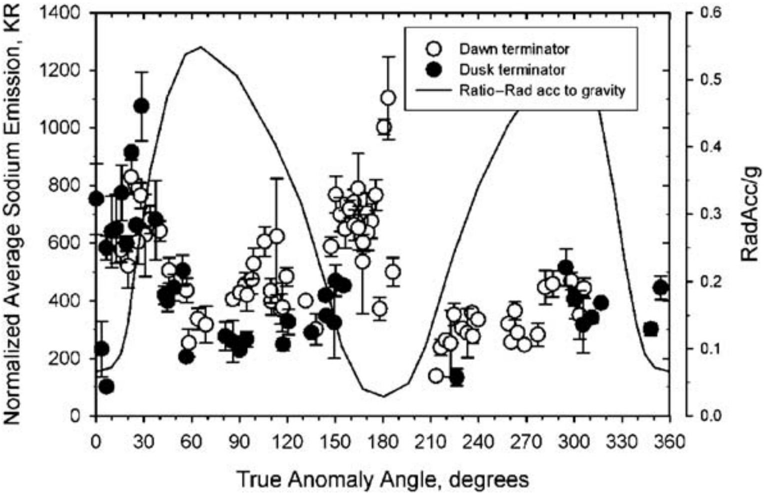

Fig. 10 Sodium emission intensities have been normalized to the values they would have at a constant value of solar radiation intensity (that seen by Mercury at a true anomaly angle of 150.26°). The normalized intensities are proportional to the average column content of sodium, in the absence of any secondary effects of radiation acceleration. The normalized emission shows maxima near perihelion and aphelion. The ratio of solar radiation acceleration to surface gravity (*solid curve*; axis RHS) reaches maximum values near true anomaly angles of 60 and 300 degrees

Fig. 11 The normalized sodium emission plotted against radiation acceleration. Dawn terminator observations are shown as *open circles* and dusk terminator observations as *filled circles*. There is a wide scatter of the data. A linear fit to the data yields an R-square value of 0.2

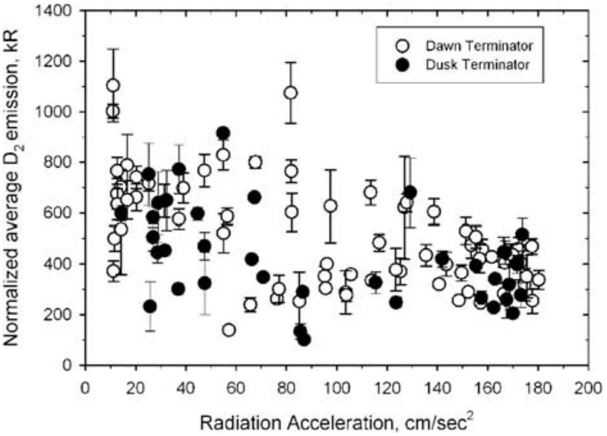

However, Sprague et al. (1997) found no correlation at all between column content and radiation acceleration. Recently, Potter et al. (2007) used the data shown in Fig. 10 to examine the effect of radiation acceleration. The data points from Fig. 10 are replotted against radiation acceleration in Fig. 11. There is no consistent trend with radiation acceleration. There are some sequences where the normalized emission intensity actually increases with increasing radiation acceleration.

Potter et al. (2007) found that most of the data scatter was not random, but could be explained by assuming that the sodium atoms on Mercury were exposed to the accelerating effects of sunlight for about 1,700 seconds. The effect of radiation acceleration was different whether the "out" leg or the "in" of the orbit was observed. There is a positive feedback loop

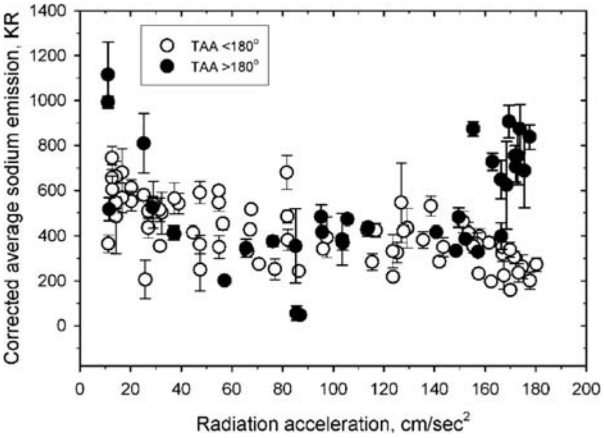

Fig. 12 The normalized sodium observations were corrected for the effect of solar radiation acceleration. The wide scatter of data points seen in the uncorrected emission values shown in Fig. 11 has diminished. A linear fit to the data yields an R-square value of 0.015 compared to 0.2 prior to the correction. An initial decrease is followed by a wide region of near-constant corrected emission, with changes near the end of the plot at maximum radiation acceleration. Near the end, there is a sharp increase of about 20% for observations on the "in" leg of the orbit. This effect may be real, or it might be an artifact of the simplified concept used for the correction

in the "out" leg of the orbit, such that radiation acceleration increases the solar continuum intensity seen by the atoms, and a negative feedback loop in the "in" leg of the orbit, such radiation acceleration decreases the continuum intensity. The result of this effect is that the emission intensity per sodium atom is increased over the non-accelerated value on the "out" leg of the orbit, and is decreased on the "in" leg of the orbit. The emission values corrected for this effect showed much less scatter, with a general trend of about 30% to lower values from minimum to maximum radiation as shown in Fig. 12.

After the correction for the secondary effects of radiation acceleration, the emission intensities should be truly proportional to the column content. To obtain column content values, the corrected emission intensities were multiplied by 9.712, which is the g-factor at a true anomaly angle of 150.26°. The results were plotted against true anomaly angle with the result shown in Fig. 13.

The results are compared with the theoretical predictions of Smyth and Marconi (1995) in Fig. 13. For true anomaly angles less than 180°, most of the data fall near the line predicted for perfectly elastic collisions with the surface ($\beta = 0$), suggesting that the interaction of sodium atoms with the surface is weak. The negative change in continuum with increasing radiation pressure at true anomaly angles greater than 180° causes the intensity per atom to decrease, so that the emission is actually under-corrected at true anomaly angles between 300 and 330 degrees of true anomaly angle. The curve should in fact be compressed, so that the atoms have a similar emission rate per atom in the entire region between 330 and 360 degrees of true anomaly angle.

Comparison of column densities at aphelion with those at perihelion is important, because at these two points, the effect of radiation acceleration is negligible. The column content at aphelion was larger than at perihelion by a factor of about 1.3, suggesting that the source processes for sodium do not quite keep up with loss processes as Mercury approaches the Sun, falling short by about 30%.

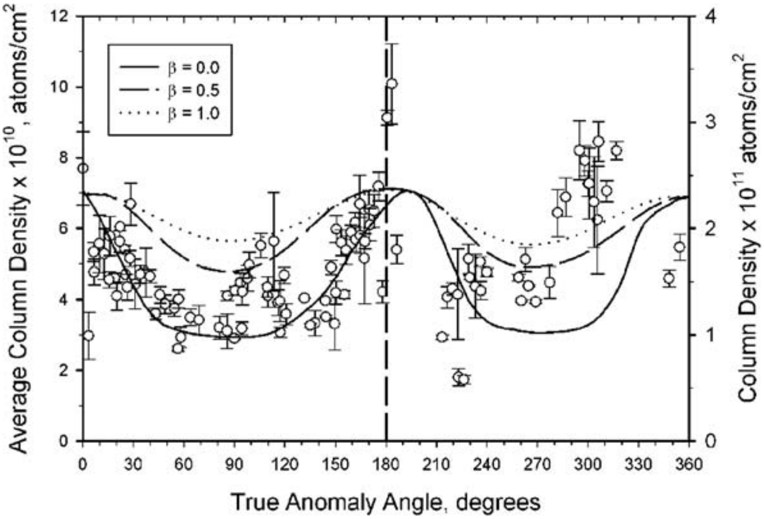

Fig. 13 Average column content data computed from the acceleration-corrected data of Fig. 12 is compared with predictions of Smyth and Marconi (1995). (Note that this average is taken over the area of the entire 10 × 10 arc second image slicer. The angular area of Mercury in view is about a third of this value, so densities referred to the Mercury surface would be about three times larger.) There are three overlays on this plot, taken from Fig. 15 of the Smyth and Marconi (1995) paper, in which they took into account radiation acceleration and the interaction of the sodium atoms with the surface

These results show that radiation acceleration can alter the emission intensity without any change in the column content of sodium. Consequently, the effect of radiation acceleration on emission intensities should be taken into account if column densities are to be calculated from emission intensities.

1.8 The Sodium Tail of Mercury

Models of the Mercury sodium exosphere published by Ip (1986) and Smyth and Marconi (1995) predicted that radiation acceleration could sweep sodium completely off the planet into a down-sun tail, depending on the energy of the atoms. Potter et al. (2002b) were able to observe the sodium tail of Mercury in twilight, mapping it downstream to a distance of about 40,000 km, as shown in Fig. 14. At that point, the velocity of the sodium had increased to about 11 km/sec as the result of solar radiation acceleration. The cross-section of the tail at 17,500 km downstream had a half-width of about 20,000 km, which implied transverse velocities of sodium in the tail of 2 to 4 km/sec. These velocities imply source velocities from the planet of the order of 5 km/sec. The total integrated flux of sodium in the tail was approximately 10^{23} atoms/sec, which corresponds to 1 to 10% of the estimated total production rate of sodium on the planet.

Considering that Smyth and Marconi (1995) estimated that atoms with velocities in excess of 2.1 km/sec could escape the planet into the tail, it appears the solar radiation acceleration can provide this velocity over a considerable range of the orbit. The radial velocity at which the observed tail disappears would be a measure of the initial velocity of the sodium atoms, but this would be different on the inbound and outbound legs of the orbit, on account of the fact that the effect of radiation acceleration is different for the inbound and outbound legs.

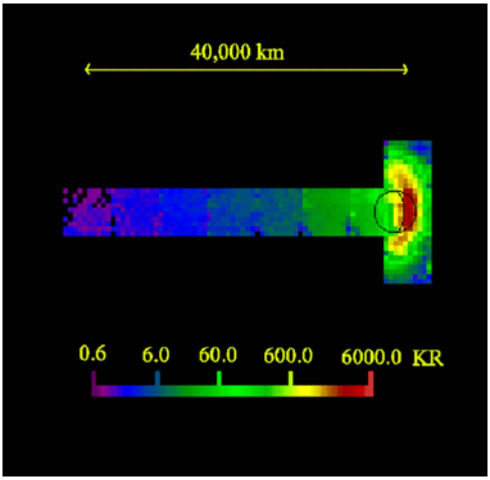

Fig. 14 The sodium tail of Mercury as observed May 26, 2001. A 10 × 10 arc second image slicer was used to capture square sections of the tail downstream from the planet

1.9 Potassium in the Exosphere of Mercury

Potassium in the exosphere of Mercury was reported by Potter and Morgan (1986). Sodium and potassium are chemically and physically very similar, so the appearance of potassium is not surprising.

The discovery spectrum is shown in Fig. 15, where it is seen that the emission line is very much weaker than for sodium. The abundance of potassium is much less than that of sodium. In the discovery spectra, the average column content of potassium was estimated to be about 10^9 atoms/cm^2, about 1% of the column abundance of sodium. Potassium observations reported by Sprague et al. (1990) found typical potassium abundances of 5.4×10^8 atoms/cm^2.

When they placed the slit over the longitudes of the "hot poles" where the Sun is overhead at perihelion, they found enhanced potassium abundance over the Caloris Basin and its antipode, as shown in Fig. 16.

Sprague et al. (1990) suggested that the potassium enhancements are consistent with an increased source of potassium from the well-fractured crust and regolith associated with the fractures in the basin floor and the hummocky terrain at the antipode. Killen et al. (1991)

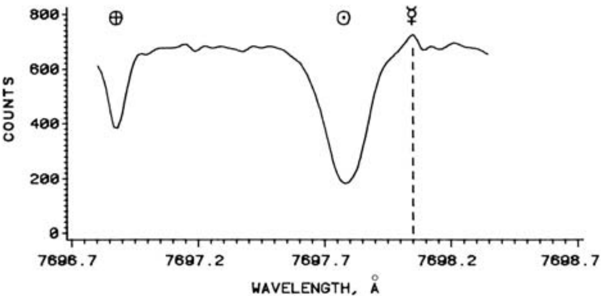

Fig. 15 Mercury reflectance spectrum showing emission from the potassium D_1 line at 7698.05 Å, Doppler-shifted from its rest wavelength of 7698.98 Å. The stronger D_2 emission line can only be observed when the Doppler shift is such as to move it out from under an atmospheric oxygen absorption line

Fig. 16 Potassium observations (Sprague et al. 1990) showed an enhanced column abundance when the spectrograph slit was over the longitude of Caloris Basin and over the antipodal terrain 180° away. These longitudes are both under the Sun during perihelion

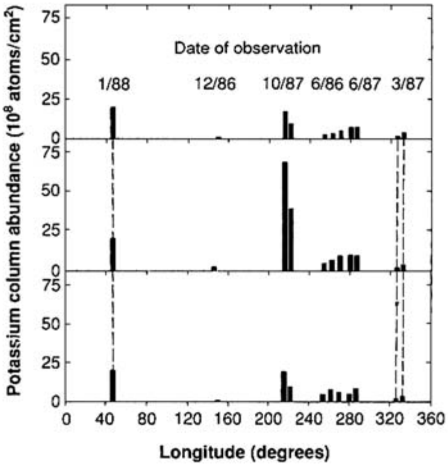

Fig. 17 Potassium observations of Sprague et al. (1990) show higher abundance in morning than in afternoon. This is explained in Sprague (1992) as a result of K ion implant into regolith materials during the long Hermean night with subsequent release to the exosphere the following morning. By afternoon, the source of implanted K ions is diminished

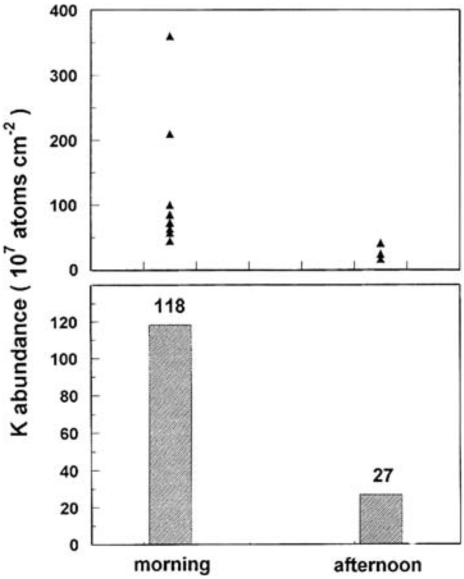

presented an alternate interpretation of the observation: because the localized sources of sodium could not be consistently correlated with specific locations on Mercury's, she noted that potassium sources may also not be consistently correlated with hermeographic locations either.

Sprague (1992) noted that potassium observations showed a marked morning/afternoon asymmetry (Fig. 17), similar to that observed for sodium, and presented a model in which potassium ions implant on the nightside of the planet where the footprint of the magnetosheath intersects the surface. In the morning the potassium is released by heating and thermal desorption.

Hunten and Sprague (2002) summarized all their data concerning the diurnal variation of potassium column content, and concluded that potassium would evaporate from the surface

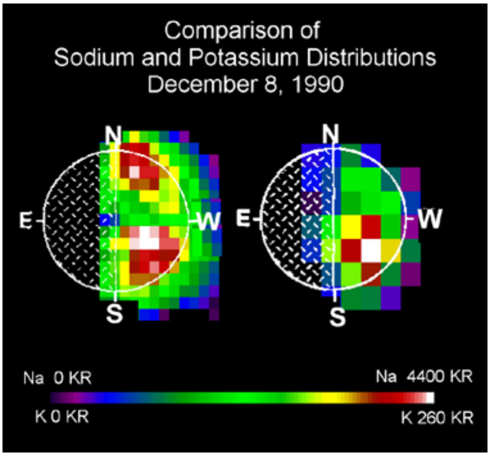

Fig. 18 Same-day maps of the sodium and potassium emission over the surface of Mercury. The sodium emission is on the left side of the image, potassium on the right. The resolution elements of the sodium image are 0.5″ square, while those of the potassium image are 1″ square. The weaker signal from the potassium exosphere required use of a lower resolution. Both sodium and potassium show excess emission in the southern hemisphere. Sodium also shows emission in the northern hemisphere equivalent to that in the southern hemisphere, while the potassium emission in the northern hemisphere is weak compared to that of the southern hemisphere. The phase angle was about 90°. The terminator is located at about 85°W longitude, and the limb at about 348°W longitude. The radar-bright spots are centered near 355°W longitude at about 55°N and 28°S, about 7° towards the center of the planet from the bright limb. True anomaly was about 284° and the radial velocity was near maximum at −9.8 km/sec. The enhancements for sodium are in the region of the radar- and albedo-bright spots A (south) and B (north). The potassium enhancement is over bright spot A

at temperatures of 400 K and higher. The chemical and physical similarity of sodium and potassium suggests that they should behave similarly on Mercury.

A comparison of sodium and potassium images supports this view. Same-day images of sodium and potassium emissions were measured by Potter and Morgan (1997) over a five-day period from December 6–10, 1990. Both the sodium and potassium emission were more intense at high northern and southern latitudes, and varied from one day to the next. The distributions of sodium and potassium emission over the Mercury surface were similar (but not identical), supporting the view that they are generated by similar processes. For this series of observations, the ratio of peak sodium intensity to peak potassium intensity was about 190. An example of the sodium and potassium images is shown in Fig. 18.

A series of sodium and potassium observations reported by Potter et al. (2002a) showed that the ratio of sodium to potassium was highly variable. This is illustrated in Fig. 19, where the ratios of planetary averages of sodium to potassium column densities are plotted against the potassium column densities.

Table 4 compares the Na/K ratio in different solar system bodies.

The ratio is found to vary from a low of 2 in the Earth's crust to a high of up to 190 in Mercury's exosphere. It is instructive to note that the highest values of this ratio are both seen in atmospheres (Earth) or exospheres (Mercury), indicative of differential loss. In the atmosphere of the Earth, the source of sodium is primarily sea salt, which is enriched in sodium due to differential solubility of Na/K in water. Thus a factor of 3 enrichment in the atmosphere must be attributed to removal of K, which is the heavier of the two. A low value of Na/K in the Earth's crust indicates dissolution of Na salt in the seawater, which is ultimately subducted to the mantle. In Mercury's case, we do not know the initial Na/K

Fig. 19 The ratio of sodium to potassium emission plotted as a function of potassium column content. Although the average ratio of sodium to potassium is about 100, there are significantly higher and lower values. The ratio decreases with increasing potassium density, suggesting that sodium and potassium densities can vary independently of one another

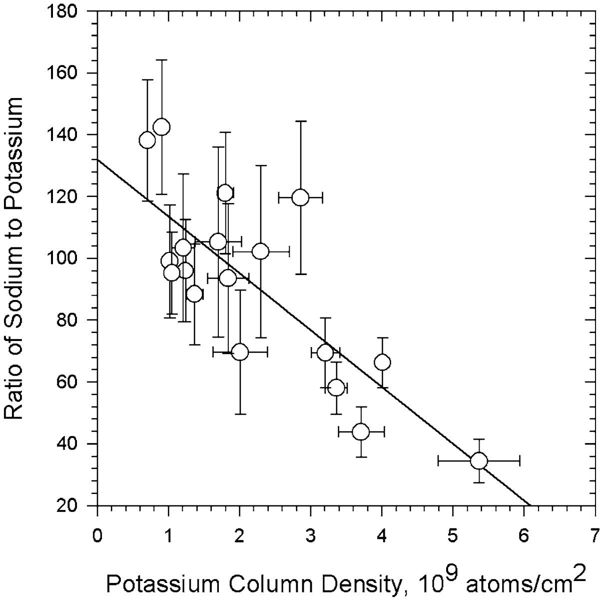

Table 4 Sodium to potassium ratios in the solar system

Object	Na/K	Source
Mercury exosphere	40–140	Potter et al. (2002a)
Io exosphere	10	Brown (2001)
Europa exosphere	25	Brown (2001)
Moon exosphere	6	Potter and Morgan (1988)
Lunar crust	7–9	Lodders and Fegley (1998, p. 177)
Meteorites	7–14	Lodders and Fegley (1998, p. 311)
Earth atmosphere	20–150	Gault and Rundle (1969)
Earth seawater	27	Lodders and Fegley (1998, p. 164)
Earth crust	2	Lodders and Fegley (1998, p. 143)
Solar system	15	Lodders and Fegley (1998, p. 80)

ratio in the crust. However, radiation acceleration is higher for potassium than for sodium, and the shape of the Fraunhofer lines are different. Consequently, the effect of radiation acceleration on emission intensity will be different for the two species, and that may be the cause of the variations of Na/K ratio observed. There also may also be ion/wave resonances that increase the loss rate of potassium ions. At present this is speculation, but measurement of wave modes by the upcoming missions should investigate these processes.

1.10 Calcium in the Exosphere of Mercury

Sprague et al. (1993) reported an unsuccessful search for calcium emissions at 4226.73 Å, estimating an upper limit for calcium of 7.4×10^8 atoms/cm^2. A tenuous calcium exosphere at Mercury at a density of 1–1.5×10^8 atoms/cm^2, principally seen in the polar regions, was first observed in July 1998, using the High Resolution Echelle Spectrograph (HIRES) at the W.M. Keck I telescope (Bida et al. 2000). Figure 20 shows results for calcium observations

Fig. 20 Variation of column abundance and velocity for calcium as a function of radial distance from Mercury (Killen et al. 2005). Data are shown for three dates: July 19, 1998, June 30, 1999, and June 9, 2000

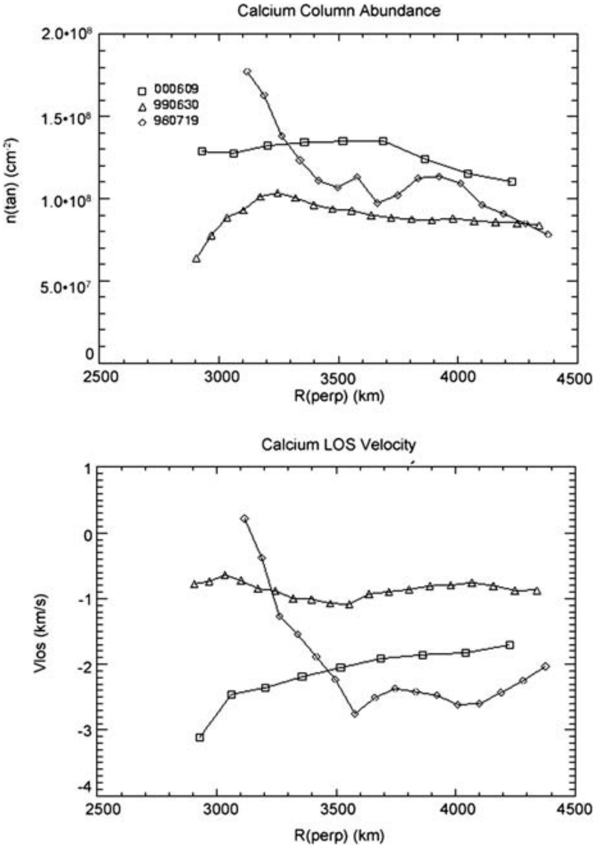

in 1998, 1999, and 2000. The emission was observed off the disk, but near the poles of Mercury.

Killen et al. (2005) summarized four years of observations of the calcium exosphere of Mercury. As seen in Fig. 20, the observations show a persistent but spatially variable blue shift, indicating an excess velocity toward the observer of up to 3 $\mathrm{km\,s^{-1}}$, with an average excess velocity of 2.2 $\mathrm{km\,s^{-1}}$ above the south pole. In addition, the line profiles reveal a hot corona at the equivalent of 12,000–20,000 K in a thermalized atmosphere, indicating a large range of motion with respect to the observer. The calcium is not confined to the polar-regions: rare and low Ca abundance is seen in the equatorial regions. Strong emission was seen anti-sunward on May 3, 2002. Apparent weak emission on the sunward hemisphere may be due to scattered light from the surface, or may indicate a high latitude source. Sputtering and impact vaporization could introduce calcium into the exosphere from Mercury's crust.

Killen et al. (2005) suggested that the likely source of the calcium is either impact vaporization in the form of CaO and clusters, which are subsequently photo-dissociated, or ion-sputtering of atoms, molecules and ions. The column abundance is somewhat, but not strongly, correlated with solar activity but data are sparse. Koehn and Sprague (2007) explore the possibility that the Sun is the primary source of O and Ca in Mercury's exosphere, a result of highly ionized atoms of $\mathrm{O^{+6}}$ and $\mathrm{Ca^{+11}}$ delivered by the Sun to Mercury.

1.11 Unknown Exospheric Components and Surface Composition

Despite several unpublished searches for visible and near-infrared emission from other elements in the Mercury exosphere, none have been found. Sprague et al. (1996) reported a search for lithium in the Mercury exosphere, with negative results. They estimated the upper limit for lithium abundance to be 8.4×10^7 atoms/cm^2. It is expected that the observed species represent only a small fraction of Mercury's exosphere, because at the surface the total pressure, derived from the sum of these known species, is almost two orders of magnitude less than the exospheric pressure of approximately 10^{-10} mbar, obtained by the Mariner 10 occultation experiment (Fjeldbo et al. 1976; Hunten et al. 1988). The surface composition plays a crucial role in the production and composition of Mercury's exosphere. To try to understand the importance of various processes that may be at work on Mercury one can initially use a suite of several possible surface compositions to bound the exospheric models.

The properties of Mercury's surface, especially its composition, age, origin and evolution, are not known precisely at the moment, due to the lack of sufficient remote and in situ investigations. Therefore, the surface composition can only be estimated, based on modeling and comparison with the Moon. Several scientific efforts have been made to estimate the surface composition of Mercury using spectral reflectance measurements in comparison with spectra of analog materials in laboratory studies.

Since the 1960s considerable optical and near-infrared spectra have been obtained, as discussed by Warell (2003). The measurements were improved with infrared detectors in the 1980s. The infrared spectra of Mercury, combined with laboratory studies of terrestrial, Lunar and meteoritic materials, indicate that the rock composition is dominated by feldspars and low iron pyroxene (Warell and Blewett 2004). Possible Mercurian surface compositions range from Lunar meteorites up to mixtures of Mercury analog materials such as labradorite and enstatite.

Burbine et al. (2002) used synthetic Mercury analogs to compare low-FeO anorthositic compositions with that of partial melts, derived from melting experiments on the EH4 chondrite Indarch (enstatite-rich chondrite). The goal of their work was to relate the compositions of basaltic partial melts and their residual aubritic materials to that of the Hermean crust and mantle, respectively. Blewett et al. (1997) in previous experiments used lunar anorthositic breccia MAC 88105, which is related to lunar meteoroid material, as analog to rocks of the Hermean crust. The synthetic Mercury composition used by Burbine et al. (2002) is depleted in FeO relative to the lunar anorthosite MAC 88105. However, to produce the observed spectral reddening of the surface by space weathering, surface soils should contain at least a few wt% of FeO in the bulk (Hapke 2001; Burbine et al. 2002). Mid-infrared spectral studies of Mercury's surface indicate Na-rich feldspars and pyroxene (Sprague and Roush 1998) and alkali basalt (Sprague et al. 1994). In addition, clino-pyroxene was identified (Sprague et al. 2002).

Mercury soil analogs which mirror the spectroscopic observations and range from Lunar meteorites up to mixtures of Mercury analog materials like labradorite and enstatite can be summarized as the following:

Synthetic Mercury: Burbine et al. (2002) compared low-FeO anorthositic compositions with that of partial melts, derived from melting experiments on the EH4 chondrite Indarch which is an enstatite-rich chondrite. The aim of their work was to relate the compositions of basaltic partial melts and their residual aubritic materials to that of the Hermean crust and mantle, respectively.

Lunar anorthositic breccia MAC 88105: This soil composition relates Lunar meteoroid material to rocks of the Hermean crust (Blewett et al. 1997). The Synthetic Mercury composition (Burbine et al. 2002) is depleted in FeO relative to Lunar anorthosite MAC 88105. However, to produce the observed spectral reddening of the surface by space weathering, surface soils should comprise at least a few wt% of FeO in the bulk (Hapke 2001).

$by75 + en25$, $la75 + en25$ (Bytownite–enstatite mixtures and labradorite–enstatite mixtures): Warell and Blewett (2004) investigated several mixtures of Mercury analog materials by means of visible near infrared (VNIR) reflectance spectroscopy. The best spectral fit was reached with a mixture of labradorite and enstatite (3 : 1) with about 0.1 wt% of submicroscopic metallic iron to simulate spectral reddening due to weathering. The USGS feldspar sample, which was used in the Warell and Blewett (2004) study.

$an75 + en25$, $ol75 + en25$ (Andesine–enstatite mixtures and oligoclase–enstatite mixtures): VNIR reflectance spectra show clear spectroscopic features related to electronic effects among transition elements, but is insensitive for thorough discrimination among plagioclase components. Therefore, the range was extended to andesine- and oligoclase-rich compositions.

VNIR reflectance spectra show clear spectroscopic features related to electronic effects among transition elements, but are insensitive for thorough discrimination among plagioclase components. Therefore, one cannot exclude andesine- and oligoclase-rich compositions. However, a mixture of andesine and enstatite adjusted to ratios of observed surface elements in the exosphere may be a good analog for Mercury's geochemical surface composition which contains most likely Si, Ti, Al, Fe, Mg, Ca, Na, K, Mn and O.

The presently observed and various expected exospheric species are shown in Table 5. Note that some of the reported species (e.g., N_2, O_2, CO_2 and H_2O) are just estimated as upper limits.

One should also note that the composition of Mercury's exosphere is non-stoichiometric with respect to the surface composition (Morgan and Killen 1997). The composition and temporal variability of the exosphere in part help to explain the weathering rate of the surface, and the volatile redistribution rate over both short and long time scales. What resides on the surface at this epoch is not the pristine surface, but a highly space-weathered surface that has been overturned by meteoroid bombardment, and desiccated of volatile content by many processes including photon-stimulated processes, ion sputtering and vaporization. The relative importance of these processes and their effectiveness at redistributing volatiles either to space or to high-latitude cold traps or to the nightside can be addressed by studying the exosphere (e.g., Leblanc and Johnson 2003).

2 Exospheric Sources and Their Models

2.1 Impact Vaporization

Impacting particles of small sizes (<100 μm) constantly rain onto Mercury's surface at a mean velocity of 20 km/s (Cintala 1992), churning the regolith and vaporizing the surface. Larger meteors impact more sporadically, but with higher mean velocity (Marchi et al. 2005). Many minor species, which are refractory during vaporization of silicates in vacuum, are highly volatile during hypervelocity impacts due to high temperatures and pressures during impacts (Gerasimov et al. 1998). Therefore the vapor ejected from impact vaporization will be the most representative of the surface composition.

Table 5 Expected abundances in Mercury's exosphere (Milillo et al. 2005)

Species	Surface abundance (cm^{-3})	Total Zenith Column (cm^{-2})
H	23; 230[a]	3×10^{9}[h]
He	6.0×10^{3}[a]	$<3 \times 10^{11}$[h]
Li		$<8.4 \times 10^{7}$[n]
O	4.0×10^{4}	$<3 \times 10^{11}$[h]
^{20}Ne	6×10^{3} day[c]	
	7×10^{5} night[c]	
Na	$1.7–3.8 \times 10^{4}$[a]	2×10^{11}[i]
Mg	7.5×10^{3}[d]	3.9×10^{10}[d]
Al	654[c]	3.0×10^{9}[d]
Si	2.7×10^{3}[d]	1.2×10^{10}[d]
S	5×10^{3}[d]	2.0×10^{10}[d]
	6×10^{5}[g]	2.0×10^{13}[g]
Ar	$<6.6 \times 10^{6}$[a]	$<9 \times 10^{14}$[b]
		1.3×10^{9}[k]
K	3.3×10^{2}[b]	2×10^{9}[b]
	5×10^{2}[h]	
Ca	387[d]	$<1.2 \times 10^{9}$[d]
	<239[f]	$<7.4 \times 10^{8}$[c]
		1.1×10^{8}[j]
Fe	340[d]	7.5×10^{8}[d]
H_2	$<1.4 \times 10^{7}$[p]	$<2.9 \times 10^{15}$[p]
O_2	$<2.5 \times 10^{7}$[p]	$<9 \times 10^{14}$[p]
N_2	$<2.3 \times 10^{7}$[p]	$<9 \times 10^{14}$[p]
OH	1.4×10^{3}[d,e]	1×10^{10}[d,e]
CO_2	$<1.6 \times 10^{7}$[p]	$<4 \times 10^{14}$[p]
H_2O	$<1.5 \times 10^{7}$[p]	$<1 \times 10^{12}$[c] $<8 \times 10^{14}$[p]

[a] Hunten et al. (1988): measurements or upper limits

[b] Potter and Morgan (1997)

[c] Hodges (1974): model abundance

[d] Morgan and Killen (1997): model abundances

[e] Morgan and Killen (1997): model abundances

[f] Sprague et al. (1993): measured upper limit

[g] Sprague et al. (1996, 1995): prediction

[h] Shemansky (1988): Mariner 10 measurements

[i] Killen et al. (1990): measured abundance

[j] Bida et al. (2000)

[k] Killen (2002): model abundance

[l] Killen and Ip (1999)

[m] Huebner et al. (1992) ionisation rates: experimental (e); theoretical (t) for quiet and active Sun

[n] Sprague et al. (1996): model abundance

[p] Broadfoot et al. (1976)

[q] Cremonese et al. (1997)

In addition, macro-meteors impact Mercury but at an unknown rate. Marchi et al. (2005) provided the distribution of impact probability as a function of impactor radius, up to objects of 100 m in radius. In particular, meteoritic impactors coming from the Main Asteroid Belt are expected to impact on Mercury. The contribution by these larger meteorites to the global Hermean exosphere is negligible; nevertheless, their impact is expected to produce strong, localized, but temporary increases in the exospheric density, enriched by material coming from deeper layers (Mangano et al. 2007). The impact frequency of such objects (especially in the lower size range) at Mercury is not negligible relative to the nominal duration of the BepiColombo mission (one year nominal plus one year extension).

Regardless of the size of the impactor, the initial ejecta from an impact will be high-temperature vapor (∼5,000 K). This will quickly be followed by the "liquid and vapor" at a slightly lower temperature (2,500 K). However, only the vapor ejected from Comet Tempel I in the first milliseconds was hot, followed quickly by thermalized vapor. This suggests that impact vapor may be much cooler than previously supposed.

Impact events probe to a depth of several diameters of the impacting body. Because meteorite impacts probe much deeper than any process other than venting, and because the energy density of the process is very high, the exospheric products of this emission

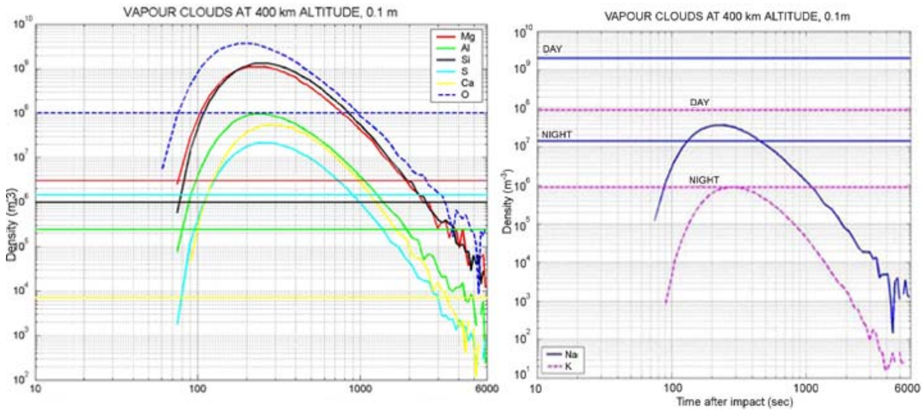

Fig. 21 Density versus time for an impacting object of 0.1 m radius, at 400 km altitude for the species whose mean density value does not change between day- and nighttime (*left*); separately, for Na and K (*right*). *Horizontal lines* represent the exospheric background for each species (from Mangano et al. 2007)

Table 6 Vaporization rates for sodium at Mercury due to micrometeoritic bombardment

Reference	Orbital position	Projectile → target	Total vaporization rate (g cm^{-2} s^{-1})	Vaporization rate Na (atoms cm^{-2} s^{-1}), with $f(\mathrm{Na}) = 0.005$
Morgan et al. (1988)	aphelion	combination	1.74×10^{-15}	2.27×10^{5}
	perihelion	combination	6.42×10^{-15}	8.40×10^{5}
Cintala (1992)	aphelion	diabase → regolith	8.18×10^{-15}	1.07×10^{5}
		regolith → regolith	7.25×10^{-16}	0.95×10^{5}
	perihelion	diabase → regolith	2.75×10^{-15}	3.60×10^{5}
		regolith → regolith	2.46×10^{-15}	3.22×10^{5}

process most closely represent the surface composition as a whole. Simulations performed by Mangano et al. (2007), analyze the effects in terms of the gaseous cloud produced by impacts of objects in the range 1 cm – 1 m. Particularly noticeable is the case of 10-cm meteor for which the enhancement, depending on the considered species, varies from 1 to 4 orders of magnitude higher than the mean exospheric background values (see Fig. 21). Figure 21 shows density versus time for an impacting object of 0.1 m radius, at 400 km altitude.

Durations are generally larger than 2,000 s, and their extension larger than 50° (calculated with respect to the center of the planet). Estimated vaporization rates from various groups are summarized in Table 6. A considerable variation in estimated rates results from uncertainties in the physical state of the surface as well as the impact flux as discussed in the following.

2.2 Interplanetary Space at Mercury's Orbit

The impact flux onto Mercury (as well as on other planets) is the consequence of several different physical processes which produce bodies on planetary crossing orbits. Detailed studies for the Earth have shown that the range of sizes impacting with our planet span over more than eight orders of magnitude: from µm up to hundreds of meters. There is no reason to doubt that the same is true also for the other terrestrial planets. Such a flux of material onto Mercury has several effects, like the formation of craters and the well-known "maturation" of the soils, for example. The role of the meteoroid flux on Mercury's exosphere is not well known.

A small fraction of volatiles released to the exosphere is thought to be produced by impact vaporization of meteoritic material. The composition of the Hermean exosphere thus reflects the chemical composition of the surface, and of meteorites impacting Mercury, mixed with traces of solar wind. Unfortunately, the meteoritic gardening and the impact history of the Mercury surface is presently unknown because it depends on variables related to the composition of the surface and the flux of meteoroids. The meteoroid flux used in literature for Mercury studies are roughly derived from estimate at the Earth's heliocentric distance, then extrapolated to the inner Solar System. It means we may not have a good estimate of the statistics on the number of impacts and the velocity distribution of the meteoroids. Cintala (1992) published very nice calculations on meteoroid impacts, but his work was restricted to sizes less than 1 cm, which are subject to Poynting–Robertson drag. His calculations cannot be directly extrapolated to larger bodies. Particles having a larger size follow a completely different dynamical evolution (Marchi et al. 2005).

The radiation pressure force deflects small particles directly antisunward. They may leave the Solar System after they are ejected from a comet or formed by collision, the exact condition depending on the initial orbital parameters. Particles for which solar gravity amounts to more than twice the radiation pressure may stay in bound orbits, and they form the main content of the interplanetary dust cloud. The radiation pressure influences the orbital evolution of this latter component mainly through the Poynting–Robertson effect. The momentum transfer caused by radiation falling onto a moving particle includes, when seen in the reference frame of the Sun, a small component anti-parallel to the particle's velocity that stems from the Lorentz transformation of radiation pressure force in the frame of the particle. This is the case for particles that move in orbital motion about the Sun and are exposed to the photon flux that is directed radially outward. The small deceleration that is induced by the anti-parallel component is denoted as the Poynting–Robertson effect. Thus a drift toward the Sun is superimposed on the motion in Keplerian orbits which limits the lifetime of the dust particles, just as collisions do.

Although the Poynting–Robertson effect may vary strongly with the size, composition, and structure of particles, the radial drift of the particles that it causes is small compared to the orbital velocities. The deceleration of particles by the Poynting–Robertson effect reduces the eccentricities and semi-major axes of their orbits. This leads to an increase of dust number density with decreasing solar distance.

The particles having size larger than 1 cm are not dominated by the Poynting–Robertson effect and they have to be studied following a different dynamical approach. Most of the meteoroids arriving on the terrestrial planets come from the asteroid main belt and the main delivery routes are the well-known resonances. Among them, the most efficient in ejecting material toward the inner Solar System are the 3 : 1 and $\nu 6$ (Morbidelli and Gladman 1998; Bottke et al. 2002).

2.3 Impacts of Meteoroids

Following the description of the meteoroid fluxes at the Mercury orbit we infer that we have to take into account two different populations of meteoroids based on their size and consequently different dynamical evolution.

In the case of the smaller particles Cintala (1992) provided a very good model of meteoroid impact vaporization considering objects with radii in the range 10^{-8}–10^{-2} m, that has been used by Cremonese et al. (2005, 2006) to calculate the differential number of impacts and the mass distribution to obtain the mass of the vapor produced by the impacts. Although the larger particles have been studied in a specific dynamical model realized for Mercury (Marchi et al. 2005), the size distribution of impactors on Mercury has been calibrated with the flux observed on the Earth, for which reliable data are available (Brown et al. 2002).

Indeed, in their numerical simulations, they estimated the ratio of impacts on Mercury versus the Earth for each projectile size, and they used this ratio to scale the impact rate with Mercury relative to that observed for the Earth. For this reason the dynamical model has been obtained for meteoroid in the size range of 10^{-2}–10^{2} m, but we have to consider here only those impacts that are relevant for the daily production of the exosphere's elements that can affect the ground-based observations, limiting the size range to 10^{-2}–10^{-1} m.

The most important result concerning the velocity distribution of large particles is the wide range of impact velocities on Mercury: the mean impact velocity is about 30 $\mathrm{km\,s^{-1}}$, but the tails span from about 15 to 80 $\mathrm{km\,s^{-1}}$. For comparison, the Moon's impact distributions are much narrower with a maximum impact velocity of about 50 $\mathrm{km\,s^{-1}}$ (see Fig. 22).

Moreover, Mercury's impact distributions depend on the impactor sizes—that is, on the simplification $f(v,r) = f(v)$—used in some works (e.g., Cintala 1992), which does not hold in this case. To quantify the effects of the impactor sizes, we note that the percentage of high velocity impactors (defined as those having $v > 50\ \mathrm{km\,s^{-1}}$) are 25% and 19% for $r = 1$ and 10^{-2} m, respectively. Note that indeed on Earth it is possible to have impacts with velocities up to 80 $\mathrm{km\,s^{-1}}$, but they are sporadic events related to retrograde swarm of fragments, presumably of cometary origin. Figure 23 shows $f(v,r)$ onto Mercury's surface as a function of the projectile velocity, averaged in the size range 10^{-2} and 10^{-1} m, in the average and perihelion cases.

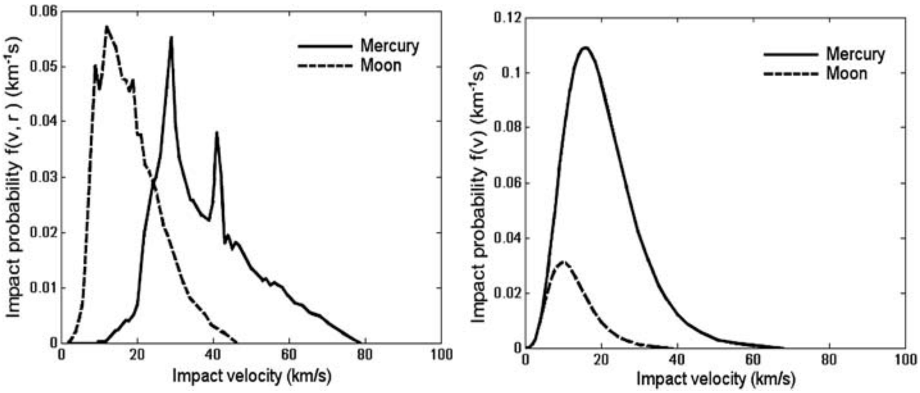

Fig. 22 *Left panel*: Impact probability $f(v,r)$, as a function of the projectile velocity, averaged over the large meteoroids range (10^{-2}–0.15 and 10^{-2}–0.10 m for Moon and Mercury, respectively). *Right panel*: Impact probability $f(v)$ as a function of the projectile velocity for small meteoroids (10^{-8}–10^{-2} m for Moon and Mercury, respectively)

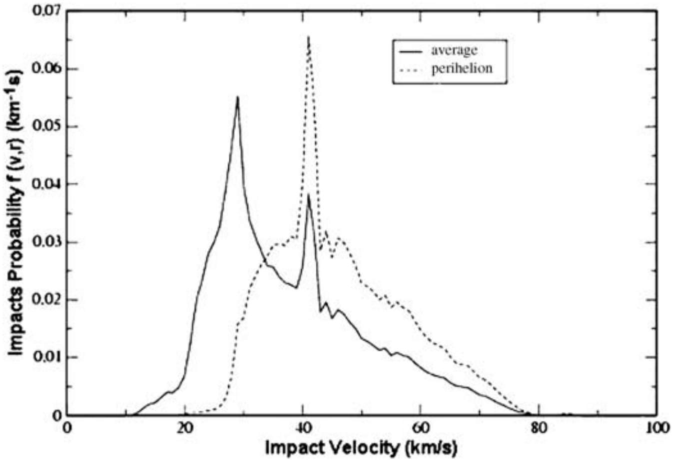

Fig. 23 Impact probability $f(v,r)$ onto Mercury's surface as a function of the projectile velocity, averaged in the size range 10^{-2} and 10^{-1} m, in the average and perihelion cases

Since the orbit of Mercury is quite eccentric ($e = 0.2$) there is some variation from the mean impact rate along its orbit. According to the model of Marchi et al. (2005) the distribution obtained for aphelion is almost the same as in the average case. On the contrary, for the perihelion case, the impact distribution is quite different and the relative number of high-velocity impacts is about 43% and 33%, respectively for $r = 1$, 10^{-2} m. Thus, impacts at perihelion happen at considerably greater velocity than the average case. Moreover, asymmetries in the rate of impacts onto planets or satellites have been widely studied for synchronous rotating bodies (e.g., see Horedt and Neukum 1984; Marchi et al. 2005) and for non-synchronous rotating bodies, like Mercury, the same considerations hold, but the asymmetry is related to the morning-evening (*am*/*pm*) hemispheres instead of to leading-trailing ones.

Following the model of Marchi et al. (2005) in the average case the ratio am/pm is greater than 1 except for $r < 13$ cm, while at perihelion the ratio is always $am/pm > 1$. The increase of the am/pm ratio with particle size is normal, as already pointed out by Morbidelli and Gladman (1998). It is due to the more numerous meteoroids having small semi-major axis, increasing the density of particles inside the Mercury's orbit, which typically tend to fall on the morning hemisphere. Also, it is normal that the *am*/*pm* ratio is larger for Mercury at perihelion, because the orbital velocity of the planet is higher, and the planet tends to catch up the meteoroids, rather than being caught up by them.

In the size range of 10^{-2}–10^{-1} m, the dynamical model by Marchi et al. (2005) estimates at perihelion $am/pm = 1.2$, while at aphelion $am/pm = 0.8$. Figure 23 shows the impact probability $f(v,r)$ in the average and perihelion cases.

The precise calculation of the amount of neutral atoms refilling the exosphere due to the impacts is not possible. Recent models that calculated the amount of vapor produced during the impact possibly represent an upper limit. The evaluation of the contribution to the exosphere requires the knowledge of the partitioning of the kinetic energy of the impact in the elements composing the vapor, allowing inference of the velocity distribution of the neutral atoms. The models considered by Cintala (1992) and Cremonese et al. (2005, 2006) treat vertical impacts of spherical projectiles into a regolith, with the shock behavior depending on the composition of the target and the meteoroid.

The quantity of melted and vaporized regolith produced by each impactor type is a function of the impact velocity and target temperature. An impact event of sufficiently high velocity creates what can be visualized ideally as a spheroidal volume, centered below the impact point, that grades from vapor through a liquid and vapor field into a completely liquid phase and on until a solid–liquid region merges into highly shocked, unfused target material. In this context it is clear that a smaller increase in internal energy will be required to initiate fusion in a hot target than a cold one, simply because the former is closer to its melting point. According to Cintala (1992) the effects of target temperature are not trivial, but they are secondary to the role played by impact velocity.

The above-mentioned models have been used to estimate the production rate of sodium, the main element observed with ground-based telescopes. That of potassium can be inferred from the ratio between the two atoms, in the composition assumed. It must be borne in mind that the cause of the high variability of Na/K observed in the exosphere is unknown. In the following we will report this calculation for the sodium.

Given the assumed velocity distribution of micro-meteors at Mercury, Cintala (1992) concluded that 1.2 projectile masses of vapor and 8.6 projectile masses of melt would be produced by a micro-meteor impact onto Mercury, whereas Morgan et al. (1988) calculated 5.4 projectile masses of vapor. As pointed out by Cintala Morgan et al. (1988) used a spatial density which was a factor or four greater than that used by Cintala, 1.8 $\mathrm{g\,cm^{-3}}$, a velocity distribution with a higher mean impact velocity, and a lower sound speed than recommended by O'Keefe and Ahrens (1986). Without these differences, Morgan et al. (1988) would have obtained 0.63 projectile masses of vapor, only half that calculated by Cintala. Given these unknowns, the exact vaporization rate must be considered to be very uncertain. An additional factor that must be kept in mind when discussing the results of impact vaporization calculations is that, for micrometeoritic impact onto a regolith, the impactors are of the order of μm and the regolith particles are of the order of 100 μm in diameter. One might imagine that a certain fraction of the energy would go into angular velocity of the regolith particles, and in addition, that the vapor produced would be largely directed downward, and would fill voids in the regolith. Therefore our knowledge of the rate and temperature of the vapor ejected into the exosphere is rudimentary at best.

2.4 Physics of the Evaporation and Production Rate

The volume of target (regolith) material vaporized by a spherical projectile of radius, r, and impacting velocity, v, can be estimated using the relation of Cintala (1992)

$$V_{\mathrm{vap}}(v,r)=\frac{4}{3}\pi r^3\left(c+dv+ev^2\right). \tag{1}$$

The constants c, d ($\mathrm{km^{-1}\,s}$) and e ($\mathrm{km^{-2}\,s^2}$) depend on target temperature and projectile composition (Cintala 1992, Table 3, page 952). In these computations the constant values have been obtained for a diabase projectile and the target at 400 K. Equation (1) was derived by Cintala (1992) for meteoroids smaller than 10^{-2} m. Cremonese et al. (2005, 2006) assumed that (1) is valid up to 10^{-1} m, and for a regolith target with a modal composition similar to those of the basalt-derived soils from the Taurus Littrow floor (Ahrens and Cole 1974): pyroxene $\sim$60%, plagioclase $\sim$30%, olivine $\sim$5% and ilmenite $\sim$0.2%. In doing so the model is based on a regolith target with a modal composition having a higher plagioclase/pyroxene ratio. It follows that (1) should underestimate the amount of material vaporized with respect to the model of Cremonese et al. (2005, 2006) using a different composition. In fact, the energy needed to vaporize the plagioclase is lower than that needed to vaporize the pyroxene (i.e., Ahrens and O'Keefe 1972). Therefore, under the same conditions of stress, plagioclase-rich rocks produce more vapor than pyroxene-rich rocks.

The total mass of the vapor produced from the infalling of meteoroids on Mercury's surface can be obtained by using (1) given the flux of bodies impacting the planet, Φ, and their velocity distribution and size distribution

$$\Phi = \iint \phi(v, r) \cdot \mathrm{d}r \cdot \mathrm{d}v, \tag{2}$$

where $\phi(v, r)$ is the differential number of impacts as a function of the meteoroid velocity and radius. Several authors (Cintala 1992; Cremonese et al. 2005; Marchi et al. 2005) used the following relation

$$\phi(v, r) = f(v) h(r), \tag{3}$$

where $f(v, r)$ is the differential velocity distribution of meteoroids (km^{-1} s), and $h(r)$ is the differential number of impacts per year and per unit of impactor radius on the entire surface of the planet (year^{-1} m^{-1}). These functions can be taken from Cintala (1992), for small meteoroids (10^{-8}–10^{-2} m), as follows

$$f(v) = \kappa d^{0.2} \left[\frac{v}{\sqrt{d(v^2 - v_{MEe}^2) + v_{Ee}^2}} \right]^3 e^{-\gamma \sqrt{d(v^2 - v_{MEe}^2) + v_{Ee}^2}}, \tag{4}$$

where $\kappa = 3.81$, $\gamma = 0.247$ (km^{-1} s), d is Mercury's orbital distance in AU, $v_{MEe} = 4.25$ km s^{-1} is the escape velocity at the surface of Mercury and $v_{Ee} = 11.1$ km s^{-1} is the escape velocity for the Earth at 100 km altitude; and

$$h(r) = -\frac{3 S_M T}{4 \rho_P \pi r^3 F_1} \left[\sum_{i=1}^{11} i c_i \ln\left(\rho_P \frac{4}{3} \pi r^3 \right)^{(i-1)} \right] \exp\left[\sum_{i=0}^{11} c_i \ln\left(\rho_P \frac{4}{3} \pi r^3 \right)^{i} \right], \tag{5}$$

where $F_1 = 0.373$ and the constants c_i ($i = 0, 1, \ldots, 11$) were reported by (Cintala 1992, Table A1, page 968), S_M is the area of the planet surface, and T is the number of seconds in 1 year. ρ_P is the meteoroid density, which is assumed to be 2.5 g cm^{-3} consistent with the measurements of the densities of stratospheric cosmic dust particles (Rietmeijer 1998) and with densities data of S-type igneous asteroids (e.g., Krasinsky et al. 2002), which are the main constituents of the inner part of the Main Belt. Equation (4) simply assumes that the flux is governed by the gravity field.

In the case of the large meteoroids (10^{-2}–10^{-1} m), $h(r)$ was given by (Marchi et al. 2005; Cremonese et al. 2005) as

$$h(r) = \frac{a_1}{r^{a_2}} \left[1 - a_3 \exp\left(-a_4 r^{0.5} \right) \right], \tag{6}$$

where $a_1 = 1.22$, $a_2 = 3.7$, $a_3 = 0.511$, $a_4 = 0.85$. Equation (6) is valid for a large size range, but the calculations have been limited to an upper limit of 0.1 m, because meteoroids with radius larger than 0.1 m are not relevant to the daily production of the exosphere. Figure 24 shows the differential distribution $h(r)$ of number of impacts per year and per unit of projectile radius in the case of large meteoroids.

The vapor composition is determined by the target compositions impact velocity (i.e., Flynn and Stern 1996), then the production rate (atoms cm^{-2} s^{-1}) of the neutral Na, S_{Na}, is

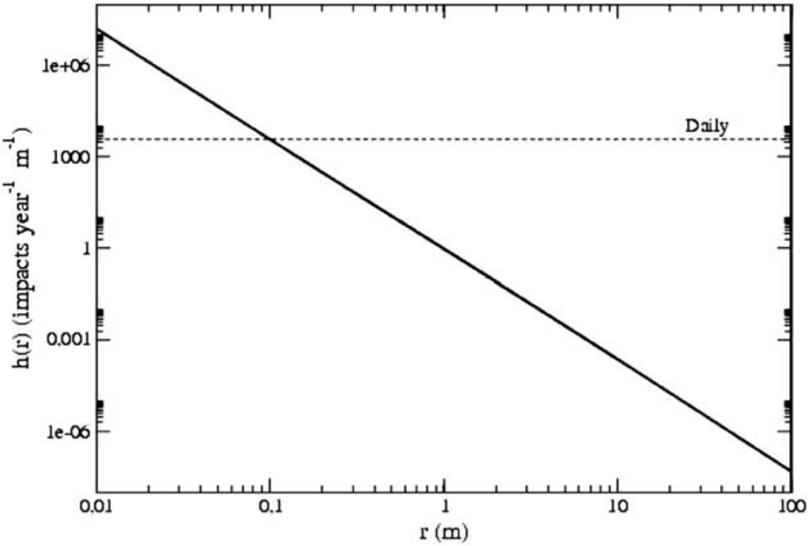

Fig. 24 The differential distribution $h(r)$ of number of impacts per year and per unit of projectile radius (on the entire surface of the planet) in the case of large meteoroids. The *horizontal line* corresponds to impacts that occur with a daily time scale

calculated by the following relation (Morgan and Killen 1997)

$$S_{\mathrm{Na}} = M_{\mathrm{vap}} \left(\frac{f_{\mathrm{Na}}}{m_{\mathrm{Na}}} \right) N_{\mathrm{A}}, \tag{7}$$

where M_{vap} is the vapor production rate (g cm^{-2} s^{-1}), m_{Na} is the atomic weight of Na, N_{A} is the Avogadro's number and f_{Na} is the mass fraction of Na in the regolith. M_{vap} has been calculated by solving the following equation

$$M_{\mathrm{vap}} = \frac{\rho}{S_M T} \int_{v_{\min}}^{v_{\max}} \int_{r_{\min}}^{r_{\max}} \phi(v, r) V_{\mathrm{vap}}(v, r)\, \mathrm{d}v\, \mathrm{d}r, \tag{8}$$

where ρ is the target density (1.8 g cm^{-3}), $v_{\min} = 4.25$ km s^{-1} and $v_{\max} = 114$ km s^{-1}, $r_{\min} = 10^{-8}$ m and $r_{\max} = 0.1$ m.

Assuming that $f_{\mathrm{Na}} = 0.038$, the Na production rate at mean orbit due to impact of meteoroids in the entire range considered (10^{-8}–0.1 m), is 1.82×10^6 atoms cm^{-2} s^{-1}, corresponding to 1.36×10^{24} s^{-1} reported in Fig. 25 as a function of the minimum meteoroid size (Cremonese et al. 2005).

The contribution of sodium to the exosphere due to large meteoroids, 10^{-2}–0.1 m, is less than 1%, and only the 7% of the Na comes from the impacts of meteoroids larger than 10^{-3} m. The number of impacts on the surface of Mercury are 6.69×10^{-7} impacts cm^{-2} s^{-1} in the size range of 10^{-8}–10^{-2} m and 2.59×10^{-21} impacts cm^{-2} s^{-1} in the range of 10^{-2}–10^{-1} m (Cremonese et al. 2005).

To estimate the contribution of the meteoroids to the production of Na the mass of meteoroids impacting the surface, for the entire size range, per unit of time and unit of surface

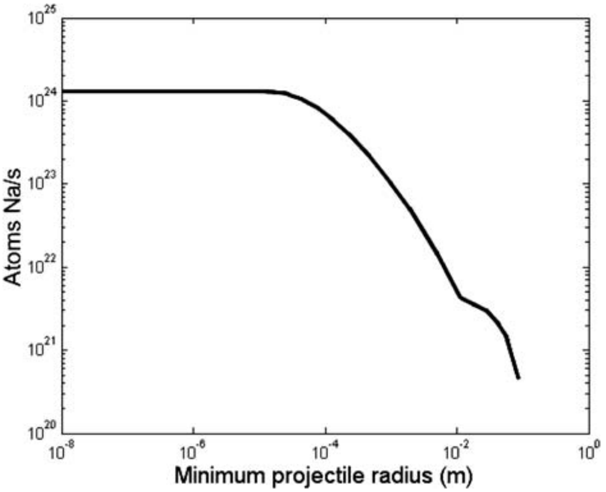

Fig. 25 Cumulative production rate of the neutral sodium atoms released in the vapor for the complete meteoroid size range, as a function of the minimum meteoroid radius. Each production rate value is due to all the meteoroids having a size larger than the corresponding radius in the x-axis. The rapid decline in the production rate at larger radius (at about 10^{-3} m) underlines the fact that the main contribution to the sodium production comes from this radius range

has been calculated as follows (Bruno et al. 2006)

$$F = \int_{v_{\min}}^{v_{\max}} \psi(v)\,\mathrm{d}v, \tag{9}$$

F is meteoritic flux in $\mathrm{g\,cm^{-2}\,s^{-1}}$, and $\psi(v)$ is the differential meteoritic flux in $\mathrm{g\,cm^{-2}\,s^{-1}}$ $\mathrm{(km/s)^{-1}}$

$$\psi(v) = \left(\frac{4\pi\rho_p}{3S_M T}\right)\int_{r_{\min}}^{r_{\max}} r^3\phi(v,r)\,\mathrm{d}r, \tag{10}$$

Figure 25 shows the cumulative production rate of the neutral sodium atoms released in the vapor for the complete meteoroid size range, as a function of the minimum meteoroid radius. Cremonese assumed that the atomic fraction of sodium in the regolith is $f_{\mathrm{Na}} = 0.038$ (Cremonese et al. 2005) which yields a source rate of $2.91 \times 10^{-16}\ \mathrm{g\,cm^{-2}\,s^{-1}}$. By assuming that the meteoroids are completely vaporized and have the same regolith composition ($f_{\mathrm{Na}} = 0.038$), the Na derived from the meteoroid material is 5.3×10^5 atoms $\mathrm{cm^{-2}\,s^{-1}}$. By adding this quantity to the previous one, they obtained a Na production of $\sim 2.3 \times 10^6$ atoms $\mathrm{cm^{-2}\,s^{-1}}$ if $f_{\mathrm{Na}} = 0.038$, or 3.0×10^5 if $f_{\mathrm{Na}} = 0.005$. This value of sodium production rate calculated by Cremonese et al. (2005, 2006) is higher than those reported by Hunten et al. (1988), 1.34×10^4 atoms $\mathrm{cm^{-2}\,s^{-1}}$, but lower than that reported by Leblanc and Johnson (2003), 6.7×10^5 atoms $\mathrm{cm^{-2}\,s^{-1}}$. It is in fair agreement with the upper limits given by Morgan et al. (1988), 1.9×10^6 atoms $\mathrm{cm^{-2}\,s^{-1}}$. Killen et al. (2001) used $f_{\mathrm{Na}} = 0.005$, and obtained a sodium source rate of 2.2×10^6 atoms $\mathrm{cm^{-2}\,s^{-1}}$ at perihelion and 1.15×10^5 at aphelion. Normalizing to the same composition, Cremonese et al. (2005) would have obtained a source rate for Na of 3.0×10^5 at mean orbit, in good agreement with the Killen et al. (2001) results.

3 Exospheric Sources and Their Models

3.1 Photon and Electron Stimulated Desorption of Surface Elements

In addition to the solar wind, plasma related to Coronal Mass Ejections (CMEs), cosmic rays and solar energetic particles, Mercury's surface environment is continuously bombarded by solar radiation and electrons. Solar radiation in the form of infrared and visible and energetic photons is absorbed by the surface and causes heating and alteration of the dayside surface area. This heating can reach dayside temperatures on Mercury of up to about 700 K at the planet's equator, which is relevant for thermal desorption. Moreover, solar photons with energies $\geq$4 eV can induce bond-breaking, which is important for photon-stimulated desorption (PSD) of absorbed elements. Lower energy electrons in the order of tens of eV are also important in addition to surface charging because they can cause electronic excitations that also lead to electron stimulated desorption (ESD) of adsorbed elements from the planetary surface. In the following subsections we describe these processes and their expected role in refilling Mercury's exosphere in more detail.

3.2 Photon-Stimulated Desorption

Photon-stimulated desorption (PSD) corresponds to the desorption of surface elements as a result of electronic excitation by a photon of a surface atom. Madey and Yakshinskiy (1998) showed that this process efficiently ejects alkalis from surfaces under laboratory conditions. Yakshinskiy and Madey (2004, 1999) found from their laboratory experiments with Na-covered lunar basalt samples that UV photons with energies of about 3–5 eV or greater than 5 eV cause desorption of "hot" Na atoms. This process acts through electronic transitions such as band gap excitation, valence electron excitation, or core excitation. Near-UV photons with energies $\leq$4 eV caused little or no detectable desorption of Na. Yakshinskiy and Madey (2004) estimated the PSD cross-section σ at photon energies of $\approx$5 eV to be about 10^{-20} cm^2, which is about seven times larger than that used by Killen et al. (2001). They found from their experiments that the desorbed Na atoms are suprathermal with a velocity peak in the PSD distribution of about 900 m s^{-1}. It was also discovered that desorption of Na varies with surface temperature and increased by a factor of 10 after the sample was heated from about 100 K to about 470 K (Yakshinskiy and Madey 2004). Cassidy and Johnson (2005) estimated that desorption from a regolith is reduced by about a factor of about three from that on a flat surface.

Bombardment of lunar silicates by UV photons ($\lambda < 300$ nm) was found to produce efficient desorption of Na atoms (Yakshinskiy and Madey 1999). The flux of atoms of species X desorbed by PSD can be given by

$$\phi_X = f_X N_\mathrm{S} \int \phi_{ph}(\lambda) Q_X(\lambda)\, \mathrm{d}\lambda, \tag{11}$$

$$\phi_\mathrm{Na}^\mathrm{PSD} = \frac{1}{4}\phi_{ph} Q_\mathrm{Na} f_\mathrm{Na} N_\mathrm{S}, \tag{12}$$

where ϕ_{ph} is the solar UV flux at Mercury, $Q_X(\lambda)$ is the PSD cross-section for species X at wavelength, λ, f_X is the fraction of species X in the regolith, and N_s is the total regolith surface density in number of atoms cm^{-2}/mean free path. The experimental PSD cross section for Na has been given as $Q_\mathrm{Na} = 1\text{–}3 \times 10^{-20}$ cm^2, integrated over the effective wavelength range, 250–400 nm (Yakshinskiy and Madey 1999). However, the actual yield in a regolith

Table 7 Solar UV flux at Earth's orbit compared with periherm (0.29 AU) and apoherm (0.44 AU)

Solar photons	1 AU [$\mathrm{cm}^{-2}\,\mathrm{s}^{-1}$]	0.44 AU [$\mathrm{cm}^{-2}\,\mathrm{s}^{-1}$]	0.29 AU [$\mathrm{cm}^{-2}\,\mathrm{s}^{-1}$]
UV-A (3.1–3.9 eV)	2×10^{16}	1×10^{17}	2.4×10^{17}
UV-B (3.9–4.4 eV)	2.5×10^{15}	1.3×10^{16}	3×10^{16}
UV-C (4.4–12.4 eV)	1×10^{14}	5.15×10^{14}	1.2×10^{14}

is reduced, perhaps by a factor of three (Cassidy and Johnson 2005) due to the possibility that ejected atoms will stick to grain surfaces before they can emerge from the regolith. The regolith surface number density is often assumed to be $N_\mathrm{s} = 7.5 \times 10^{14}\ \mathrm{cm}^{-2}$/MFP, where MFP is the photon mean free path. The solar UV flux at Mercury integrated from 100–318 nm is $\phi_{ph} = 3.31 \times 10^{15}\ \mathrm{cm}^{-2}\,\mathrm{s}^{-1}/R_\mathrm{m}^2$, where R_m is Mercury's orbital distance from the Sun in AU. The sodium fraction in the lunar regolith is 0.0053, and this value has been extensively assumed for the sodium fraction in Mercury's regolith.

Photon-stimulated desorption is induced by electronic excitations rather than by thermal processes or momentum transfer. However, a temperature dependence in the yield was found and attributed to diffusion rates to the extreme surface (Yakshinskiy and Madey 2004). The velocity distribution of emitted atoms can be described by a Weibull distribution, which has a high-velocity tail. The energy distribution of the emitted atoms from electron stimulated desorption (ESD) has been given by Johnson et al. (2002) as

$$f_\mathrm{PSD}(E) = \beta(1+\beta)\frac{EU^\beta}{(E+U)^{2+\beta}}, \tag{13}$$

where E is the energy of the emitted particle, U is the characteristic energy for PSD of a given species, and β is the shape parameter of the distribution. The shape parameters for Na and K were given by Johnson et al. (2002) as $\beta_\mathrm{Na} = 0.7$ and $\beta_\mathrm{K} = 0.25$. The peak of the Na velocity distribution from a PSD source is similar to that for a 1,100 K gas (Yakshinskiy and Madey 1999), corresponding to a $U = 0.0098$ eV in (13).

The temperature dependence for PSD, as given by the Yakshinskiy and Madey data, was fit by the following expression $(1.1448\mathrm{E}\text{-}5T^2 - 0.00163T + 0.02128)/1.8$ (Killen, in preparation) where the maximum surface temperature used in this correction is 475 K. The desorption rate from a plane surface probably differs from that of a regolith due to the probability that a desorbed atom in a regolith will collide with a surface element before reaching the extreme surface (Cassidy and Johnson 2005). PSD is not effective in ejecting refractory species.

To investigate the PSD-induced release of atoms from the surface of Mercury, the variation of solar UV photons incident on the planetary surface over the planet's orbit have to be considered. The solar flux at Mercury's eccentric orbit differs substantially from the average condition present at 1 AU. Table 7 shows the solar UV-A, UV-B and UV-C flux at periherm of about 0.29 AU and apoherm at about 0.44 AU. One can see from Table 7 that the solar UV flux is about a factor 11 higher at the periherm and more than five times higher at apoherm than that at the Earth's orbit in 1 AU.

Lammer et al. (2003), studied the PSD-induced release of Na and K atoms along Mercury's orbit. The flux of desorbed Na atoms by incoming solar UV photons could be calculated by using (12) (Yakshinskiy and Madey 1999; Lammer et al. 2003). The study of Lammer et al. (2003) showed clearly that the largest PSD fluxes of released Na occur near equatorial latitudes at periherm, where the flux could reach values depending on used PSD

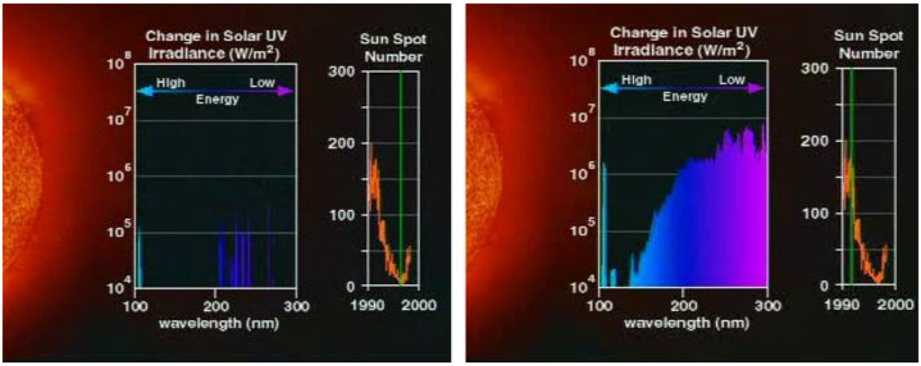

Fig. 26 The *left panel* shows the solar UV irradiance at Earth's orbit during low solar activity, while the *right panel* shows the solar UV irradiance at Earth's orbit during high solar activity where the irradiance could be up to 100 times higher than during quiet solar periods (M. Schoeberl and H. Mitchell, UARS/SUSIM, NASA-GSFC/SVS)

cross-section of about $4.5 \times 10^6 - 3.15 \times 10^7$ cm^{-2} s^{-1}. At apoherm the Na flux values at the equatorial regions are about three times lower.

The PSD-induced Na fluxes at latitudes higher than 75° are lower. Lammer et al. (2003) concluded that there should not be any noticeable PSD sources at Mercury's polar areas. The PSD-induced Na fluxes at the equatorial regions at apoherm and periherm of Lammer et al. (2003) are lower than the estimated fluxes of McGrath et al. (1986) of about 2.0×10^7–2.0×10^8 cm^{-2} s^{-1} but larger than the estimated average flux value of about 2.0×10^7 cm^{-2} s^{-1} by Killen et al. (2001) and Killen and Ip (1999). A reason for the larger fluxes estimated by McGrath et al. (1986) could be that the fluxes estimated by these authors are overly optimistic since they were based on data for alkali halides (Killen and Morgan 1993).

By estimating the PSD-induced Na source rates one obtains between periherm and apoherm values in the order of about 1.0×10^{24} s^{-1}, which is in agreement with the observations by Killen et al. (2001) who found 7.6×10^{23} s^{-1} for November 13 and 1.4×10^{24} s^{-1} for November 20, 1997.

However, as one can see in Fig. 26 the solar UV flux increases up to about 100 times from low solar activity to active solar periods or during flare events. Therefore, one may expect that the Na PSD flux could reach values during high solar activity periods or flare interaction with Mercury of the order of about $\geq 10^8$ cm^{-2} s^{-1}.

A second element that can be desorbed from Mercury's surface due to solar UV radiation is K. Laboratory experiments by Madey et al. (1998) regarding the desorption of alkalis on oxide surfaces yield PSD cross-sections for K atoms which vary between $1.4 \pm 0.6 \times 10^{-20}$ cm^2 and $1.9 \pm 0.8 \times 10^{-21}$ cm^2 for wavelengths between 247.5 nm (5.0 eV) and 365 nm (3.5 eV). The most efficient cross-section in their experiments is about 1.8×10^{-20} cm^2 at 253.7 nm (4.9 eV). The exospheric observation by Potter and Morgan (1997) give an upper limit to Na/K ratio of about 200, which corresponds to PSD-induced K fluxes in the order of about 10^4 cm^{-2} s^{-1} for K atoms corresponding to the observed Na/K fractionation along a latitude strip that is directly facing the Sun. Because the Na/K ratio is extremely variable in the exosphere (Potter et al. 2002a) it is likely that loss rates play a role as well as source rates.

However, note that real regolith on Mercury's surface is different from the material studied by Madey et al. (1998). Since it has been irradiated, the alkali binding could be altered, the porosity of the material is unknown and sticking could be an efficient process. These factors can cut down the cross-section by more than an order of magnitude. Further, the surface layer can be depleted in alkali (Hapke 2001; Madey et al. 1998).

3.3 Electron-Stimulated Desorption

In addition to PSD experiments with adsorbed Na and K atoms on lunar silicates, Yakshinskiy and Madey (1999, 2004) also studied electron-stimulated desorption (ESD). They found that exposure of Na covered surfaces by low energetic electrons with energies from 3–50 eV causes also desorption of "hot" Na atoms. Generally there are intimate connections between ESD and PSD because similar electronic processes cause desorption of the atoms via electron or photon excitation. The release of Na via ESD is strongly temperature dependent. The observed average ESD cross-section for Na atoms and 10–50 eV electrons is about $1\text{–}2 \times 10^{-19}$ cm^2 (Yakshinskiy and Madey 1999, 2004). The experimentally determined ESD cross-section for atomic Na has its initial threshold at about 4 eV, which is comparable with the PSD threshold. Furthermore, the desorption cross-sections have a similar magnitude for electron energies of about 5 eV and there is a resonance like feature at about 11 eV (Yakshinskiy and Madey 1999). If one assumes quasi-neutral solar wind plasma, then electron fluxes for electrons with energies of about 12 eV are about $5 \times 10^9 - 2 \times 10^9$ cm^{-2} s^{-1} at periherm and apoherm, respectively. The flux of adsorbed elements like Na or K due to ESD can be calculated by

$$\Phi_{\mathrm{ESD}} = \Omega \Phi_e \sigma_{\mathrm{ESD}} f, \tag{14}$$

where Ω is the area where the electrons can reach the planetary surface divided by the whole planetary surface, Φ_{e} is the electron flux at Mercury's environment, σ_{ESD} is the ESD photon cross-section and f is the composition of the regolith abundance for instance of Na in Mercury's surface. Because Φ_{e} is several orders of magnitude smaller than the photon flux Φ_v, ESD during ordinary solar wind conditions will not be an efficient release process for adsorbed surface elements like Na or K compared to PSD, sputtering or micrometeoroid evaporization.

Leblanc et al. (2003b) considered a particular SEP event with particle energies larger than 10 keV. The event was observed in detail at the Earth's orbit (Reames et al. 1997) and rescaled to Mercury's orbit. Generally SEPs can reach Mercury before or few hours after the arrival of the shock and a magnetic cloud usually associated with a Coronal Mass Ejection (CME) that is for an unperturbed Mercury's magnetosphere for quiet solar wind conditions. Leblanc et al. (2003b) studied test particles representative of the energy flux distribution for each SEP ion species and for the electrons. They launched the particles from the magnetopause and followed them inside Mercury's magnetosphere and surface by using a magnetospheric model of Luhmann et al. (1998). They found that these particles can cause ESD of Na atoms and, because they penetrate more than the solar wind ions or UV photons, they can enhance the supply of Na atoms to the surface where it can be desorbed by thermal or PSD.

3.4 Particle Surface Sputtering

The impact of energetic ions on a solid surface (e.g., Mercury's surface) will cause the release of particles via momentum transfer, which is called sputtering, or more precisely physical sputtering. Particle sputtering will release all species from Mercury's surface into space, reproducing more or less the local surface composition on an atomic level. Preferential sputtering of the different elements of a compound will lead to a surface enrichment of those elements with low sputtering yields in the top-most atomic layers. However, the steady-state composition of the flux of sputtered atoms will reflect the average bulk composition. Thus, particle sputtering, when operative, will give us compositional information about the refractory elements of the bulk surface.

The normalized energy distribution for particles sputtered from a solid, $f(E_e)$, with the energy E_e of the sputtered particle, has been given as (Sigmund 1969)

$$f(E_e) = \frac{6E_b}{3 - 8\sqrt{E_b/E_c}} \frac{E_e}{(E_e + E_b)^3} \left(1 - \sqrt{\frac{E_e + E_b}{E_c}}\right), \tag{15}$$

where E_b is the surface-binding energy of the sputtered particle and E_c the cut-off energy for sputtered atoms. The cut-off E_c, which is the maximum energy that can be imparted to a sputtered particle by a projectile particle with energy E_i, is given by the limit imposed by a binary collision between a projectile atom, m_1, and the target atom, m_2, (to be sputtered) as

$$E_c = E_i \frac{4m_1 m_2}{(m_1 + m_2)^2}. \tag{16}$$

Figure 27 shows the normalized energy distribution for several elements. Note that the maximum of the energy distribution is at $E_{\max} = E_b/2$, with E_b ranging from fractions of an eV to several eV depending on species and mineral/matrix. At higher energies the distribution falls off with E_e^2 until the energy E_e approaches the cut-off energy E_c.

The polar angle distribution of sputtered atoms, $f(\alpha)$, for polycrystalline surfaces is best described by a quadratic angular dependence, $f(\alpha) \propto \cos^2\alpha$ for laboratory experiments (Hofer 1991). By modeling the details of sputtering in loosely packed regolith grains, Cassidy and Johnson (2005) found that for a fine-grained and porous regolith a better choice is $f(\alpha) = \cos\alpha$. For the azimuth angle a uniform distribution over 2π is a suitable description. Having the energy, the azimuth, and elevation angle one can calculate all three components of the initial particle velocity, **v**, and the trajectory of each sputtered particle in the exosphere. Using many such trajectories a vertical density profile $N_i(h)$ can be calculated (Wurz and Lammer 2003; Wurz et al. 2007). The density profile can easily be integrated to obtain the column content, which is the typical measurement obtained from telescopic observations of the exosphere. Either the exospheric density at the surface or the column content can be used to compare with observational data. The flux Φ_i of atoms sputtered from the planetary

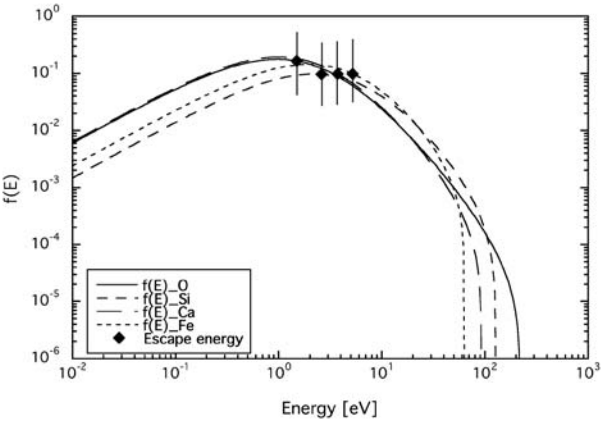

Fig. 27 Normalized energy distributions for sputtered O, Si, Ca, and Fe atoms by impact of protons of 1 keV energy using (1). The *symbols* indicate the energy corresponding to the escape velocity of each sputtered atom

surface can be calculated as

$$\Phi_i = \Phi_{\text{ion}} Y_i^{\text{tot}} = \Phi_{\text{ion}} Y_i^{\text{rel}} C_i, \tag{17}$$

where Φ_{ion} is the energetic ion flux onto the surface and Y_i^{tot} the total sputter yield of species i; that is, the number of released surface atoms per incoming ion, from the surface with a given elemental composition. The total sputter yield Y_i^{tot} can be broken up into a relative sputter yield Y_i^{rel} and C_i the atomic abundance of species i on the surface. The total sputter flux of species i can also be written as

$$\Phi_i = N_i(0)\langle v_i \rangle, \tag{18}$$

with $N_i(0)$ the exospheric particle density at the surface ($h = 0$), and $\langle v_i \rangle$ the average velocity of sputtered particles. Combining (17) and (18), the exospheric density at the surface resulting from the sputter process for species i is

$$N_i(0) = \Phi_{\text{ion}} Y_i^{\text{tot}} \frac{1}{\langle v_i \rangle}, \tag{19}$$

$N_i(0)$ can be used in a calculation as a starting point to derive a quantitative density profile from the sputtering process for a given surface composition. The average release velocity is derived from the sputter distribution, (1), as

$$\langle v_i \rangle = \frac{3\pi}{4} \sqrt{\frac{2E_{b,i}}{m_2}}, \tag{20}$$

where $E_{b,i}$ is the binding energy of species i in the particular chemical/mineralogical mix of the surface (Wurz et al. 2007). Note that the most probable velocity is $v_{mp} = \sqrt{E_{b,i}/m_2}$, which is lower than the average release speed by a factor of about 3.3. These velocities have to be compared to the Hermean escape speed of 4.250 $\text{km}\,\text{s}^{-1}$. If we take oxygen as an example, with a binding energy of $E_b = 2.0$ eV, we get $\langle v_i \rangle = 11.57$ $\text{km}\,\text{s}^{-1}$, which exceeds the escape velocity considerably. The same is true for other elements. Thus, many sputtered atoms escape Mercury's gravity field. This can been seen in Fig. 27 where the energy corresponding to the escape speed is indicated in the energy distribution of sputtered atoms.

Therefore, if the flux of ions impinging the planetary surface, Φ_{ion}, is known one can calculate ab initio, with the sputter yields Y_i^{tot} for a particular surface composition, the sputtered flux, the surface density, the density profile, and the column content and compare these numbers with the observations. This has been done for the Moon recently (Wurz et al. 2007).

In addition to atoms, clusters of two and more atoms can be released from the solid surface via sputtering. For metallic surfaces the release of metallic dimers, trimers, etc. with yields of about $10^{-1}, 10^{-2}, \ldots$ with respect to the atomic sputter yield, has been observed in the laboratory (Gnaser and Hofer 1989; Wurz et al. 1990, 1991; Hansen et al. 1998). For oxide surfaces, which are more representative to the mineralogical surface of Mercury, one observes monoxides like SiO or CaO and larger oxide molecules, with yield ratios up to [Me/MeO] ~ 1 (Oechsner et al. 1978; Wucher and Oechsner 1986; Wurz et al. 1990). The sputter yield of such dimers (metallic and oxides) depends strongly on the chemical environment on the surface, mostly on the surface being oxidized or metallic. This has been investigated by performing sputter experiments on clean metallic surfaces that were oxidized in a controlled way (Wurz et al. 1990; Hansen et al. 1999).

It was found that the oxide molecule yields correlated strongly with the oxygen coverage, with the sputtered monoxide yield as large as the atom yield at maximum oxygen coverage, and the metal clusters anticorrelated with the oxygen coverage. The energy distribution of sputtered clusters is similar to the energy distribution of sputtered atoms, as given in (1) (Wucher and Oechsner 1986; Hansen et al. 1998), but the fall-off at higher energy of sputtered particles is $f(E_e) \propto E_e^{-n}$ with $n > 2$ (Coon et al. 1993; Betz and Husinsky 2004).

Since sputtering is a quite energetic process sputtered clusters have temperatures of several 1,000 K when released, which limits their stability against falling apart. So far clusters of sputtered atoms have not been observed directly in Mercury's exosphere, but it has been proposed that a significant contribution to the Ca exosphere arises from sputtered CaO molecules that fall apart at high altitudes (Killen et al. 2005).

A fraction of the sputtering atoms are positive or negative ions. The ion fraction of the sputtered atoms can be in the range between 10^{-4} and a few 10^{-1}, depending on element, matrix, and primary ion (Benninghoven et al. 1987). Sputtered ions were used for compositional analysis of ground-up sample simulants of mare and highland soils to mimic the sputtering behavior of lunar regolith (Elphic et al. 1993). Because of the lack of an atmosphere and ionosphere for Mercury, sputtered ions immediately are picked up by the electro-magnetic fields of Mercury's magnetosphere or escape with the solar wind.

Large areas on Mercury's surface are exposed to solar wind even during regular solar wind conditions, and solar wind ions are the most important ion population causing sputtering from Mercury's surface. Solar wind velocities are in the range of 300 to 800 km/s (slow and fast solar wind), which translates to energies of 0.5 to 3.3 keV/amu, and with a typical value of 1 keV/amu. Note that the sputter yield has a maximum around ion energies of 1 keV/amu. In the solar wind, protons and alpha particles make up more than 99% of the ions, and heavy ions (from carbon to iron and up) together are about 0.1% of the solar wind ions in the number flux (Wurz 2005, and references therein).

For the lunar surface total sputter yields are about 0.07 surface atoms per impinging ion for the typical H/He mix of solar wind ions (Wurz et al. 2007). Heavier ions have sputter yields even larger than 1, but because their abundance in the solar wind is very low their contribution to the total sputter yield of the solar wind is negligible. The He/H ratio in the normal solar wind is about 0.04 (Aellig et al. 2001), with He abundance varying from about 0.02 at solar minimum to 0.06 at solar maximum. For solar wind speed below 350 km/sec the average He/H is 1.8%. Increasing solar wind speed implies increasing He abundance in the solar wind, where $\mathrm{He/H} = a + bv_{\mathrm{sw}}$, where a and b depend on the solar cycle (Aellig et al. 2001).

During coronal mass ejections (CMEs) the He/H ratio can be enhanced to about 0.2 in a CME (Sarantos et al. 2007), which will increase the sputter yield accordingly. Moreover, the abundance of heavy elements can also be significantly increased in CMEs with respect to undisturbed solar wind (Wurz et al. 2001, 2003), which may become important for the sputter yields. Heavy ions are also highly enriched in SEP events (e.g., Wiedenbeck et al. 2005; Cohen et al. 2005); however, at these energies the sputter yields are very low since the particles penetrate far into the solid.

It is expected that the sputter yield on Mercury's surface will be about the same as that on the moon. The sputter yield has to be reduced by the porosity of the surface (Cassidy and Johnson 2005), thus we estimate that the actual sputter yield for Mercury's surface is between 0.02 and 0.025 surface atoms per impinging ion for the typical mix of solar wind ions.

The heavy ions in the solar wind are highly charged because of the million-degree hot solar corona. Oxygen, for example, is present in the solar wind with charge states of typically +6 and +7; iron is present with charge states in the range from +8 to +12. These high charge states mean that the ions have high internal energies (potential energies), for example, 295 eV for O^{6+} and 1055 eV for Fe^{10+}, as compared to singly or doubly charged ions. The charge state affects the sputtering yield due to the potential (ionization) energy available, hence the term "potential sputtering". However, these high internal energies (potential energies) have to be compared to their kinetic energies in the solar wind of typically 16 keV for oxygen and 56 keV for iron. It has been argued that the sputter yield for highly charged ions impacting on a planetary surface is increased by a factor of 10 to 1,000 as a result of their high internal energy (Shemansky 2003). The laboratory data on sputter yields for highly charged ions have been reviewed by Aumayr and Winter (2004), and we will briefly summarize their findings here. For metallic surfaces and semiconductors (Si and GaAs) no deviation of the sputter yield for highly charged ions from the sputter yield of singly charged ions was found, with the highest charge states investigated being Ar^{9+} and Xe^{25+}. Moreover, all the measured sputter yields agree with the TRIM calculations, a software package which considers only the kinetic energy of the impacting ion (Ziegler and Biersack 1985).

For ionic crystals (NaCl and LiF) a pronounced increase with ionic charge state was observed; for NaCl the sputter yield increased by a factor of 4 for Ar^{8+} ions compared to Ar^{+} ions, for LiF the sputter yield increased by a factor of 25 for Ar^{14+} ions compared to Ar^{+} ions. Note that Ar charge states in the solar wind range from +8 to +11.

For oxides, which are the best analog for Mercury's surface, a clear signature of a sputter yield increase for highly charged ions was observed for SiO_2 and Al_2O_3. For SiO_2 this increase was about 3 for Ar^{8+} ions compared to Ar^{+} ions, and about 65 for Xe^{25+} ions compared to Ar^{+} ions. Similar enhancements were found for the Al_2O_3 surface. Measured sputter yields of 1.5 keV Xe^{q+} onto Al_2O_3 show an approximately 40-fold increase in the sputter yield for Xe^{28+} over that of Xe^{9+}. Both of these materials appears to have a finite sputter yield at zero kinetic energy of the projectile. On the other hand, for a highly ionic oxide such as MgO, even though potential energy greatly increases the sputter yield, potential energy does not induce sputtering in the absence of kinetic energy of the projectile.

However, this enhancement is strongly depending on the ion dose the surface has been exposed to. After a removal of about a monolayer from the oxide surface the sputter yield for highly charged ions drops to about the values for singly charged ions. Removal of a monolayer of surface material corresponds to a heavy ion flux of a few 10^{13} ions cm^{-2} s^{-1} at solar wind energies, which takes about two weeks at Mercury's orbit. This reduction in sputter yield is attributed to the very surface becoming reasonably conductive (by preferential loss of oxygen and the creation crystal defects) and thus the highly charged ions become decharged; that is, they lose their internal energy when they approach the surface.

To model ion sputtering it is important not only to model Mercury's magnetosphere but also to understand the composition of the solar wind at Mercury and its variability. These effects are being considered to correctly characterize the ion sputter source (Sarantos et al. 2007).

3.5 Surface Maps of Particle Fluxes and Energies

Sputtering of Na by solar wind ions impinging onto the surface of Mercury through the cusps of the magnetosphere was first suggested by Potter and Morgan (1990) to explain rapid variations in the observed Na exosphere, with high- to mid-latitude enhancements appearing and disappearing on intervals of less than a day. Such variations cannot be attributed to PSD which varies slowly with true anomaly angle of the planet, and which would be characterized by a sub-solar maximum in the distribution. Variations in the sodium exosphere during a week-long sequence in November 1997 were shown to correlate with possible variations in Mercury's magnetosphere such that increased ion sputtering correlated with opening of the cusp regions and an increased ion flux to the surface (Killen et al. 2001). The role of the precipitation of the solar wind plasma has received a noticeable interest because ion sputtering is proposed as a potential candidate to explain rapid temporal variations in Mercury's Na exosphere observed in Earth-based remote sensing measurements (e.g., Potter et al. 1999; Wurz and Lammer 2003; Leblanc et al. 2003b).

Sputtering occurs mostly due to solar wind precipitation, even if planetary ions may contribute as well (Delcourt et al. 2003). Solar wind particles are expected to precipitate in the dayside cusps (Massetti et al. 2003; Kallio and Janhunen 2003); during this motion, a large fraction ($\sim$90%) of the protons are bounced by the increasing magnetic field, the others (10%) reach the surface of Mercury and lead to ion-sputtering, or (1%) are neutralized due to charge-exchange effect (Mura et al. 2006a). During this motion, protons do not exactly follow magnetic field lines: particles are drifted northward by the $\mathbf{E} \times \mathbf{B}$ drift and westward by the grad-$\mathbf{B}$ drift (Mura et al. 2005).

The former is energy-independent; the latter is more efficient for the highest energies. Moreover, non-adiabatic effects may become of crucial importance for most of the ion magnetospheric transport (Delcourt et al. 2003; Massetti et al. 2007). Figure 28 shows an example of maps of surface precipitation for high- (1–10 keV) and low-energy (100 eV–1 keV) protons; high-energy protons (up to several keV), accelerated by the reconnection mechanism, precipitate at lower latitudes with respect to low-energy ones (see Massetti et al. 2003).

The intensity and the shape of the H^+ flux depend on the magnetospheric configuration which, in turn, depends on both the intrinsic magnetic field of Mercury and variable external parameters, such as the interplanetary magnetic field (IMF), and solar wind velocity and density (Kabin et al. 2000; Kallio and Janhunen 2003; Massetti et al. 2003).

Even if Mariner 10 measurements revealed the existence of an intrinsic magnetic field, this estimation has a considerable uncertainty, because it is difficult to separate the internal and external magnetic field components (Connerney and Ness 1988). Nevertheless, the di-

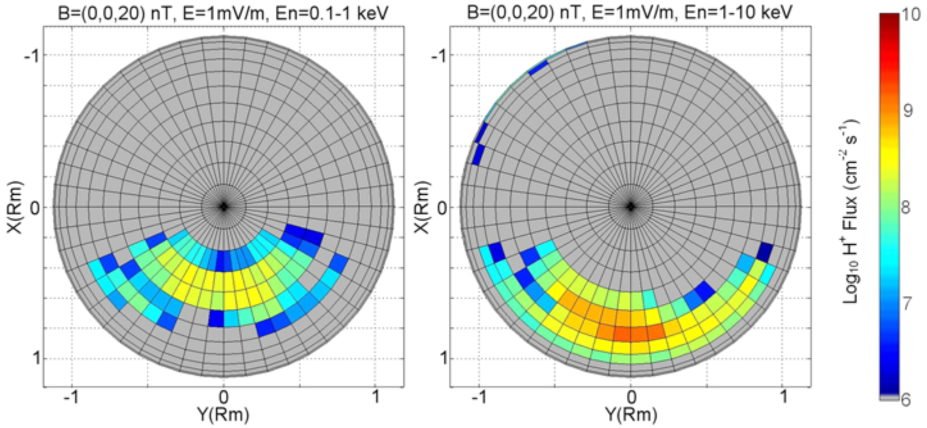

Fig. 28 Example of solar wind proton precipitating flux onto the north hemisphere, in an open magnetospheric configuration ($B_{\mathrm{IMF}} = [0, 0, -20]$ nT). *Left panel*: low energy (<1 keV) protons; *right panel*: high energy (>1 keV) protons. Adapted from Mura et al. (2006c)

pole moment is probably between 284 and 358 nT R_{M}^3 (Ness et al. 1975); for comparison, the Earth's dipole is approximately 3×10^4 nT R_{E}^3. Peculiarities in Mercury's magnetosphere arise also from the specific conditions of the solar wind at Mercury's orbit (0.31–0.47 AU), which differ substantially from the average conditions present at 1 AU.

Parker spiral forms an angle of about 20° with the solar wind radial direction, while it is approximately 45° at the Earth. This implies a change of the relative ratio of the IMF components with respect to the near Earth conditions, and a modified solar wind–magnetosphere relationship. The average solar wind density is about ten times higher than at the Earth, and this value varies considerably due to the high eccentricity of the orbit of the planet, with average densities from 34 cm^{-3} at the aphelion, to 83 cm^{-3} at the perihelion. The dynamic pressure is, on average, approximately 16 nPa (Massetti et al. 2003). By applying all the above parameters, it has been estimated that the sub-solar point, where the internal and external pressures balance, is about 1.5 R_{M} out from Mercury's center (Siscoe and Cristofer, 1975; Goldstein et al. 1981), while at the Earth this value is 11 R_{E}. In this respect, the scale-length of Mercury's magnetosphere is 1/7 compared to the Earth's.

Ion precipitation at Mercury has been a subject of several analyzes motivated by Mariner 10 magnetic field and electron measurements made in 1974–1975. Unfortunately, there are no direct ion measurements available from the Mariner 10 flybys. Many studies of the solar wind-Mercury interaction have focused primarily on analyzing the role of the interplanetary magnetic field (Luhmann et al. 1998; Kabin et al. 2000; Killen et al. 2001; Sarantos et al. 2001; Ip and Kopp 2002; Kallio and Janhunen 2003; Massetti et al. 2003), and on the solar wind dynamic pressure (Sarantos et al. 2007), the motion of ions in the Hermean magnetosphere produced from the Hermean exosphere and emitted the surface (Ip 1987; Delcourt et al. 2003, 2002; Killen et al. 2003), and the motion of the solar wind protons injected from the tail (Lukyanov et al. 2001).

Both uncertain quantities and the large number of possible configurations make it very difficult to include all of them in a model of proton precipitation. Evaluation of H^+ flux on the surface may be obtained from MHD simulations (Leblanc et al. 2003a), quasi-neutral hybrid MHD simulations (Kallio et al. 2003), single particle models (Mura et al. 2005) and loss-cone estimations (Massetti et al. 2003); in the first two cases, the magnetic field is obtained from the model; in the other cases, it must be provided separately (for example, it may be reconstructed by adapting a magnetic field model of the Earth to Mercury's case (Massetti et al. 2003), assuming proper values for the IMF, the solar wind density and velocity). These precipitation models generally prescribe two areas of intense precipitation, roughly corresponding to the cusps regions, or a big area of precipitation located in the planetary dayside, depending on external conditions or simulation assumptions.

Table 8 summarizes some relevant quantities related to solar wind proton and planetary ion precipitation.

The H^+ flux onto the surface of Mercury may exceed values of 10^9 $\mathrm{cm}^{-2}\,\mathrm{s}^{-1}$, and the total integrated H^+ flux onto the surface of Mercury can be estimated as about 10^{25} s^{-1}. During solar energetic particle (SEP) events, high-energy integrated proton flux may be up to 10^{26}–10^{27} s^{-1} (Leblanc et al. 2003a). Alpha particles exhibit a smaller flux (approximately one tenth) but the yield for sputtering is considerably higher, so that they are expected to contribute to this process as well. The flux of the exospheric ions, like sodium, is much lower, and can reach 10^6–10^7 $\mathrm{cm}^{-2}\,\mathrm{s}^{-1}$ (Delcourt et al. 2003; Leblanc et al. 2003b); those ions can precipitate and generate sputtering also in the nightside. The maximum sputtering flux due to this process has been estimated by Delcourt et al. (2003) and is around 10^4 $\mathrm{cm}^{-2}\,\mathrm{s}^{-1}$. The flux of ions to the Hermean surface depends strongly on solar wind dynamic pressure and on IMF (e.g., Kallio and Janhunen 2003; Delcourt et al. 2003), and strong disturbances such as SEP or CME events (e.g., Cohen et al. 2005).

Table 8 Flux related to solar wind proton and planetary ion precipitation

Quantity	Value	References, notes
Flux ($cm^{-2}\,s^{-1}$)	1.5×10^8	McGrath et al. (1986) (H^+)
	4×10^8	Massetti et al. (2003) (H^+, IMF = [0, 0, −10] nT)
	2×10^9	Massetti et al. (2003) (H^+, upper limit)
	2×10^9	Mura et al. (2005) (H^+, upper limit)
	10^5–10^6	Delcourt et al. (2003) (Na^+, perihelion-aphelion)
Integrated flux (total), (s^{-1})	8×10^{24}	Leblanc et al. (2003b) (SEP, H^+, 10 keV – 10 MeV)
	3×10^{23}	Leblanc et al. (2003b) (SEP, $He2^+$)
	1.1×10^{25}	Massetti et al. (2003) (H^+, IMF = [0, 0, −10] nT)
	4×10^{25}	Mura et al. (2005) (H^+ IMF = [0, 0, −20] nT)
	3.9×10^{25}	Kallio and Janhunen (2003) (H^+, IMF = [0, 0, 10] nT)
	3.4×10^{25}	Kallio and Janhunen (2003) (H^+, IMF = [0, 0, −10] nT)
	2.7×10^{25}	Kallio and Janhunen (2003) (H^+, IMF = [32, 10, 0] nT)
	30×10^{25}	Kallio and Janhunen (2003) (H^+, High USW)
Fraction of precipitating ions	8%	Leblanc et al. (2003b) (SEP, H^+, 10 keV – 10 MeV)
	11%	Leblanc et al. (2003b) (SEP, other species)
	10%	Mura et al. (2005) (H^+)
Open field area (cm)	7.3×10^{16}	Killen et al. (2001) (H^+)
	2.8×10^{16}	Massetti et al. (2003) (H^+, IMF = [0, 0, −10] nT)
	1.8×10^{17}	Mura et al. (2005) (H^+ IMF = [0, 0, −20] nT)

One criticism of this source process is that the sputtering efficiency of protons, the dominant ion in the solar wind, is quite small and cannot account for significant sputtering (Koehn et al. 2003). When the IMF has either a negative B_z or a strong B_x component, magnetic reconnection occurs between IMF and the Hermean magnetic field. In this case, H^+ particles from the magnetosheath can cross the magnetopause, enter the magnetosphere and precipitate following open field lines. The shape of proton flux onto the surface (and, hence, of the ion-sputtering flux) approximately mimics the shape of the reconnection at the MP.

In a purely IMF-B_z case, reconnection occurs only if B_z is negative; however, the B_x component plays a substantial role in the magnetosphere solar wind coupling (Kabin et al. 2000; Sarantos et al. 2001; Kallio and Janhunen 2003; Massetti et al. 2007). In fact, the different angle of the Parker spiral at Mercury compared to the Earth suggests that the B_x component could be dominant. Non-zero B_x values introduce a north–south asymmetry in the H^+ surface precipitation; this feature is very important because it can easily explain the north–south asymmetries in the earth-based observation of some exospheric components (e.g., sodium).

An asymmetry in impacting ion flux translates into an asymmetry in the neutral atmosphere only when ion sputtering is a strong comparative source of atmospheric neutrals. This generally happens when the IMF is southward ($B_z < 0$). Since southward fields were observed roughly only half the time in Helios I and II data, a north–south asymmetry in impacting proton flux should be expected for only 16–28% of Mercury's lifetime. Still, visible asymmetries could sometimes result from a northward IMF when photon-stimulated desorption is weak—namely at aphelion. At a first look, this result implies that north–south asymmetries in impacting ion flux might be quite frequent at Mercury.

When the radial component of the IMF is dominant, most of the precipitating solar wind ions impact on one hemisphere: for a sunward-pointing component ($B_x > 0$) most ions reach the surface of Mercury's southern hemisphere; the opposite is true for an anti-sunward-pointing field ($B_x < 0$). This north–south asymmetry was first pointed out by Sarantos et al. (2001) who qualitatively showed that, for a negative B_x, solar ions have a velocity component parallel to Mercury's (open) magnetic field configuration in the northern hemisphere but antiparallel in the southern hemisphere, and vice versa. Sarantos et al. (2007) analyzed the Helios I and II magnetic field data collected while the spacecrafts were within Mercury's orbital range. A dominant B_x was defined as one being at least twice that of either of the other two components. Results show that the B_x was "dominant" according to the above definition between 32–57% of all time. (Each set of data is defined as one spacecraft pass between 0.31 AU to 0.47 AU. The lowest occurrence of a dominant B_x in a set was 32%, while the highest was 57%.)

To quantify this, Kallio and Janhunen (2003) tested one case of a Parker IMF ($B_x = 32$ nT, $B_y = 10$ nT, $B_z = 0$ nT). They found that in that case only 36% of the total proton flux impacted the northern hemisphere. This result implies that when there is a north–south asymmetry of the sputtering emissions in the atmosphere, an upper limit of a $2:1$ ratio of total content in each hemisphere should be expected.

Figure 29 shows a numerical, single-particle simulation of the H^+ flux onto the dayside surface, as a function of IMF-B_x: in the figure, the $B_x > 0$ case is shown, and in this configuration the proton flux on the surface is expected to be higher in the southern hemisphere. To find how often the radial component of the IMF is dominant, Sarantos et al. (2007) implemented an analysis of the Helios data collected while the spacecrafts were within Mercury's orbital range. These authors used 40-second averages of the IMF and computed the probability density (normalized occurrence rate) estimate (see Fig. 30) At first look, this result implies that north–south asymmetries in impacting ion flux might be quite frequent at Mercury.

However, an asymmetry in impacting ion flux translates into an asymmetry in the neutral atmosphere only when ion sputtering is a strong comparative source of atmospheric neutrals. This generally happens when the IMF is southward ($B_z < 0$). Since southward fields were observed roughly only half the time in Helios I and II data, a north–south asymmetry in impacting proton flux should be expected for only 16–28% of Mercury's lifetime. Still, visible asymmetries could sometimes result from a northward IMF when photon-stimulated desorption is weak—namely at aphelion. Figures 31 and 32 show the precipitating flux of solar wind ions impacting Mercury's surface for likely aphelion and perihelion conditions. The relative recycling and escape rates of ions of Hermean origin has been a long-standing question (e.g., Ip 1987).

Global tracings of magnetospheric ions (Na^+ and K^+) in static magnetic field configurations given by the modified TH93 model (Killen et al. 2004a; Sarantos 2005) indicate that impacts dominate, while the escape rate of these species to the solar wind responds very slightly to external conditions: between aphelion and perihelion the escape ratio was seen to range from 30% to almost 40% (Sarantos 2005, PhD thesis). While long-term recycling is very strong, it is reduced by about a factor of 1.5 at perihelion. This prediction could help explain why the sodium atmosphere is observed to be denser at aphelion. In contrast, Delcourt et al. (2003) and Leblanc et al. (2003a) found significantly reduced relative recycling rates of $\sim$10%.

The sodium ion precipitation in Delcourt et al. was found to be similar to auroral precipitation at the Earth. We can only speculate about the reasons for these differences. The

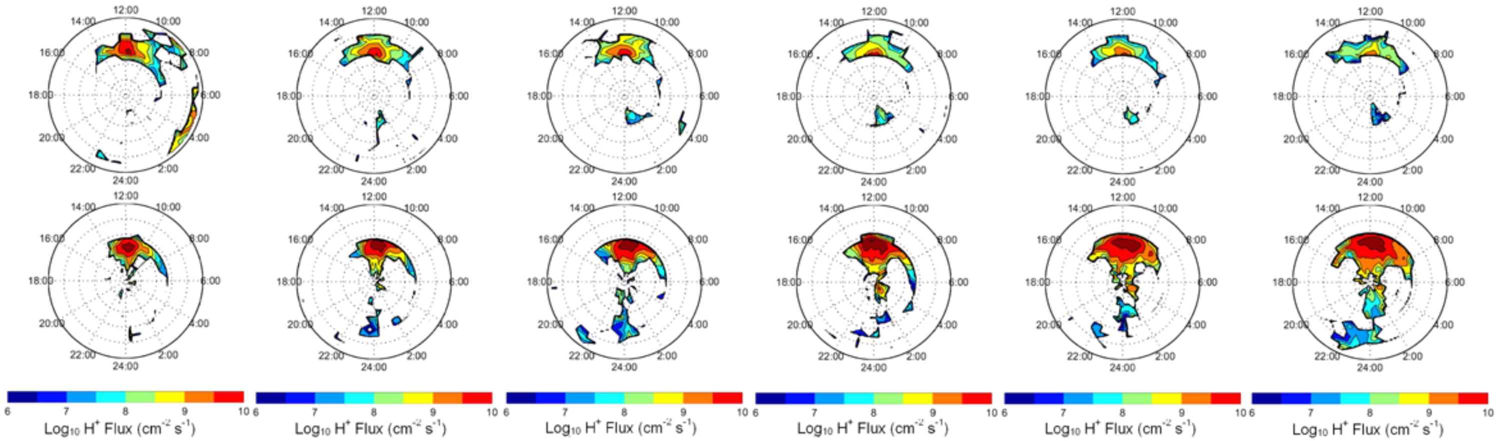

Fig. 29 Solar wind H$^+$ fluxes on the surface of Mercury, with different IMF-B_x external condition, from 5 nT (*left*) to 30 nT (*right*). *Top panels*: northern hemisphere; *bottom panels*: southern hemisphere. As a positive IMF-B_x component increases, higher fluxes are expected in the southern hemisphere. From Mura et al. (2006c)

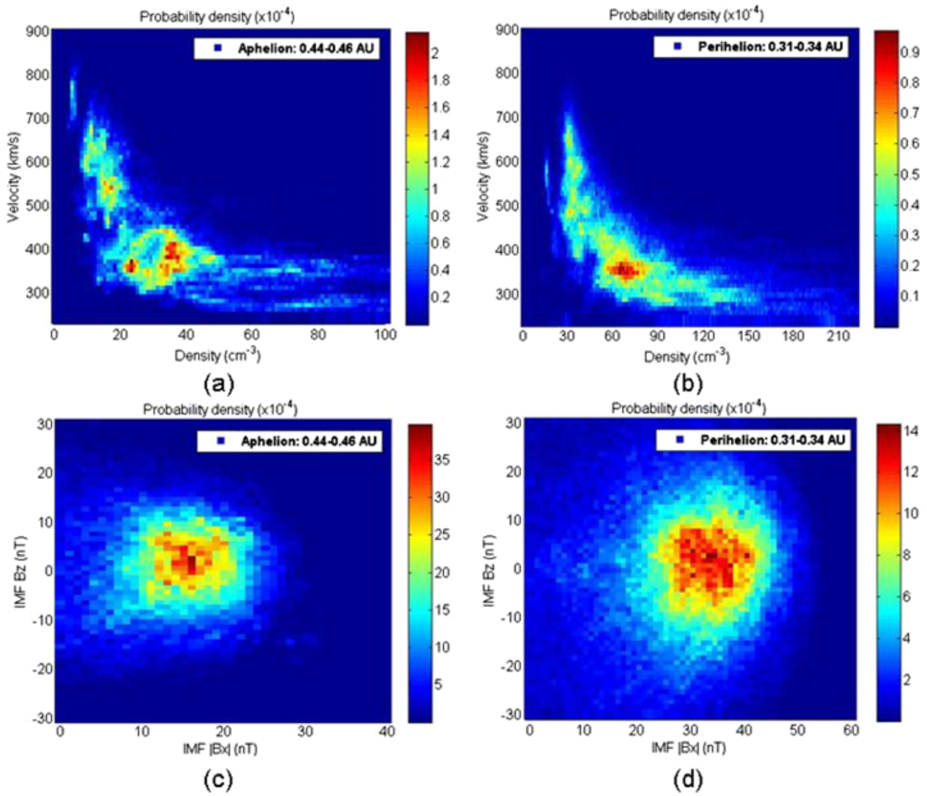

Fig. 30 Probability density estimates for important solar wind parameters from Helios 40-second data around the Hermean aphelion and perihelion (Sarantos et al. 2007)

models were run for different input conditions, with different resolutions and, most importantly, using different exosphere models which provided the initial ion distribution to be tracked. Possible explanations for these differences include pitch-angle and IMF B_x inclusion effects.

A pitch-angle effect may be related to the location of photoionization events by different exosphere models: the loss cone angle for particles launched below or at scale-height (e.g., Killen et al. 2004a; Sarantos 2005) is wider than for particles launched in the exoionosphere, so the latter may mirror instead of impact the surface.

On the other hand, the inclusion of IMF B_x in the TH93 model widens the open area, that is, the area of auroral precipitation, and makes it asymmetric. In conclusion, both investigations were limited in scope as they tested one case at aphelion and one at perihelion. These differences point to the need for more comparative simulations, with single input and boundary conditions.

Figure 33 (upper panel) illustrates the effect of likely solar wind conditions at perihelion versus aphelion on the fraction of surface area open to the solar wind.

At perihelion the solar wind is more dense than at aphelion, and the IMF is more radial, both of which act to create a more open magnetosphere. For the same B_z, the perihelion magnetosphere is more likely to have a larger surface area exposed to the solar wind. The likely precipitating solar wind flux (lower panel) is proportional to the open area and the

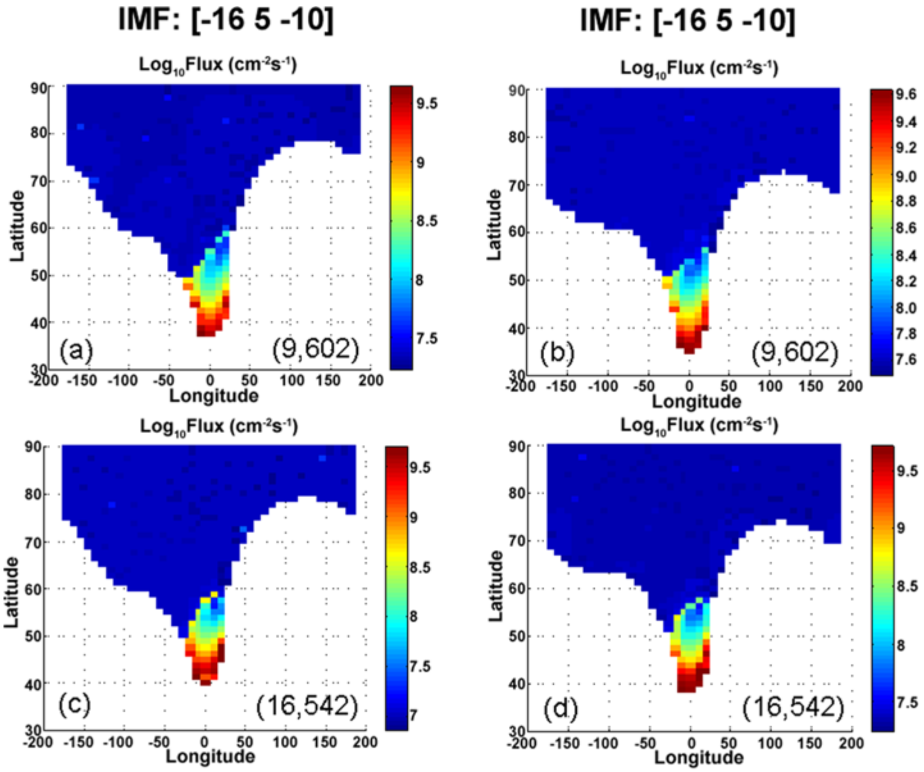

Fig. 31 Precipitating flux (*log scale*) of solar wind ions impacting Mercury's surface for likely aphelion conditions. These maps were produced with the modified TH93 model of the Hermean magnetosphere. Input conditions were selected by analyzing probability density estimates that are consistent with the Helios 40-second data in the 0.31–0.47 AU range. *Vertical columns* address the effects of increasing pressure on the cusp location and precipitation flux for the same IMF, while *horizontal rows* illustrate the effects of a more southward IMF for given pressure. The open-closed boundary exhibits a strong dawn–dusk asymmetry for the $B_z = -5$ nT cases as a result of the dominant B_x. In turn, the cusp becomes more symmetric as B_z grows comparable to B_x (cases with $B_z = -10$ nT). (Adapted from Sarantos et al. 2007)

dynamic pressure. For a precipitating integrated flux of 1.4×10^{26}, the upper and lower limits of ion sputter yield averaged over the solar wind species (0.05 and 0.15, respectively, give a yield averaged over the entire surface of the planet of 9×10^6 and 2.6×10^7 cm^{-2} s^{-1}, respectively. These yields are comparable to or greater than the PSD yields.

Heavy ions of planetary origin may be relatively energetic due to the centrifugal acceleration during $E \times B$ transport over the polar cap (Delcourt et al. 2003). Most of the Na$^+$ ions are lost into the dusk flank, but a localized region of energetic Na$^+$ precipitation develops at the planet's surface, and extends over a large range in longitude at mid-latitudes (30°–40°). These ions may sputter additional material. Characteristics of precipitating Na photoions are shown below in Fig. 34.

3.6 Extreme Solar Events

Because dense or fast solar plasma features could compress Mercury's magnetosphere so that more surface elements can be released due to sputtering into the exosphere, it is impor-

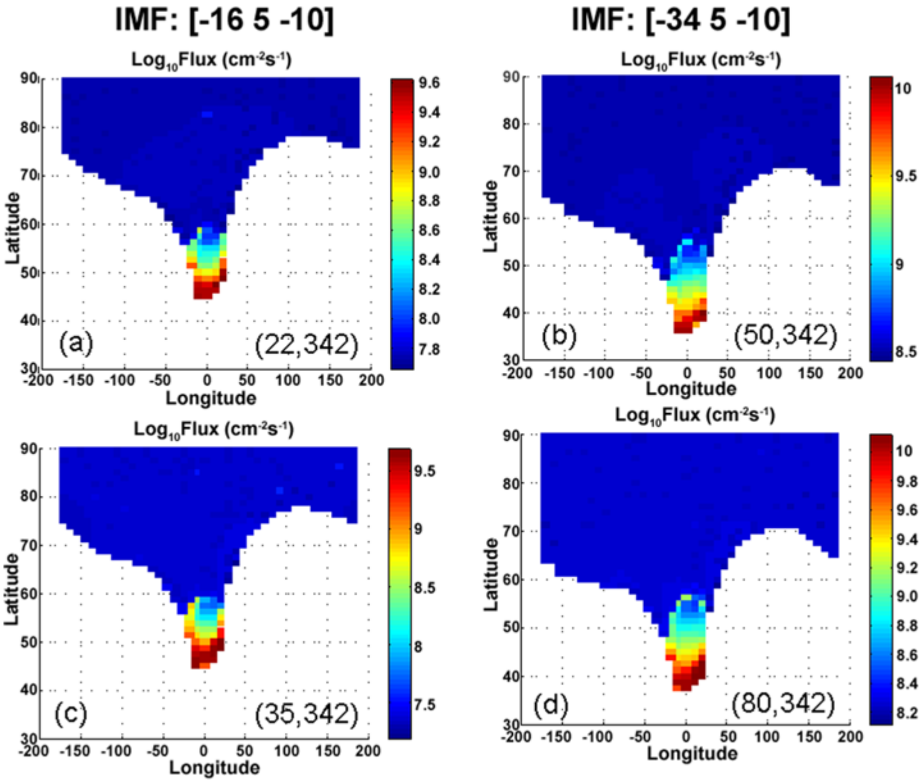

Fig. 32 Maps of the solar wind flux (*log scale*) that precipitates onto the Hermean surface for likely conditions at aphelion (**a**, **c**) and perihelion (**b**, **d**). Shown in *parentheses* are the density (cm^{-3}) and velocity (km/s) tested in each case. The open-closed boundary moves equatorwards by about 10 degrees for perihelion conditions. Responding to the denser plasma and stronger field magnitude, the precipitating flux at perihelion clearly increases both in the dayside and in the tail. The modeled integrated precipitating source (s^{-1}) increases fourfold, while the open area available to the solar wind doubles. (Adapted from Sarantos et al. 2007)

tant to study collisions with extreme solar particle events on Mercury's magnetospheric and surface environment.

Leblanc et al. (2003b) studied the interaction of a solar energetic particle (SEP) event reported by Reames et al. (1997) of protons with energy larger than 10 keV with Mercury's magnetospheric-surface environment. They expected that if a SEP encounters Mercury, a significant f1ux of energetic particles will reach Mercury's surface which may refill the exosphere. The simulations indicate that after the arrival of a SEP at Mercury, a population of quasi-trapped energetic ions and electrons is expected close to Mercury, which is stable for hours after their arrival. A significant dawn/dusk charge separation is observed and a fraction of about 10% of the initial energetic particles may impact the surface with a spatial distribution that exhibits north/south and dawn/dusk asymmetries. Furthermore, Leblanc et al. (2003a, 2003b) found that the flux of particles impacting Mercury's surface and the ability of a quasi-trapped population to be maintained near Mercury are highly dependent on the B_z sign of the interplanetary magnetic field. Leblanc et al. concluded that impacting SEPs can eject a non-uniform distribution of Na atoms into Mercury's exosphere,

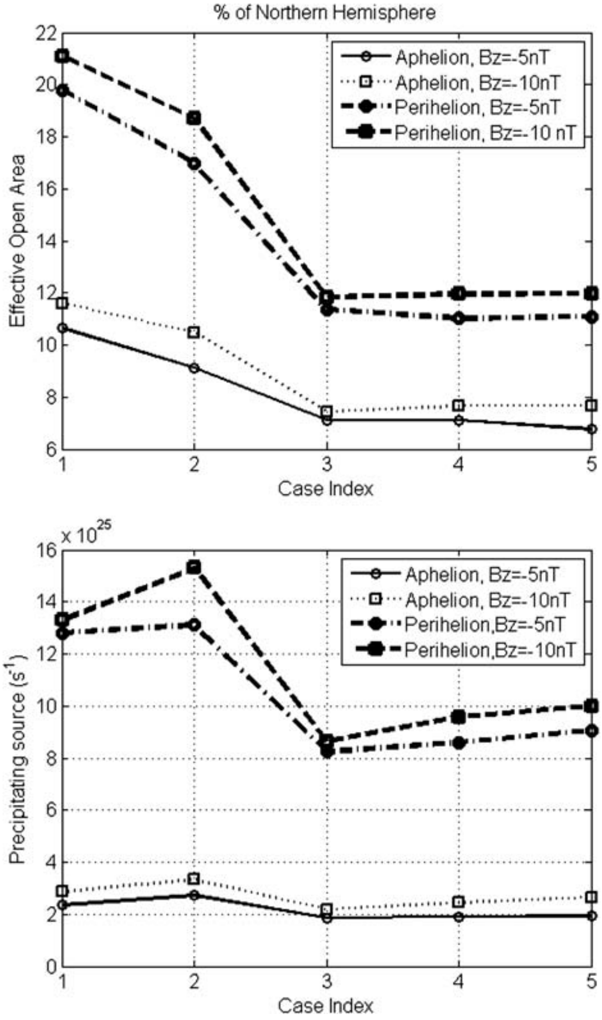

Fig. 33 Effective open area (*upper panel*) and precipitating flux (*lower panel*) for likely aphelion and perihelion conditions, respectively (Sarantos et al. 2007)

which may be the origin of several unexplained observed exospheric features, although they could not explain the total amount of Na atoms needed to reproduce the observations of Potter et al. (1999). However, much stronger SEP events than the one used in this work have been observed at the Earth (Mason et al. 1999) during the same month as the Potter et al. (1999) observations, and may have sufficient intensities. These authors proposed that the encounter of Mercury with CME or magnetic cloud (MC) events could cause such an enhancement.

Significant advances in the study of CMEs have been made by the Large Angle and Spectrometric Coronagraph (LASCO) on board of ESA's Solar and Heliospheric Observatory (SoHO), which observed more than 8,000 CMEs since January 1996. The observational data on CMEs are related to two spatial domains: the near-Sun region (up to 30 $R_{\text{Sun}} \approx 0.14$ AU) remotely sensed by coronagraphs; and the outer region, including the geospace and beyond, where in situ observations are made by spacecraft. At the larger distances such as at Mercury's orbit or beyond CMEs are traditionally called as Interplanetary CMEs or mag-

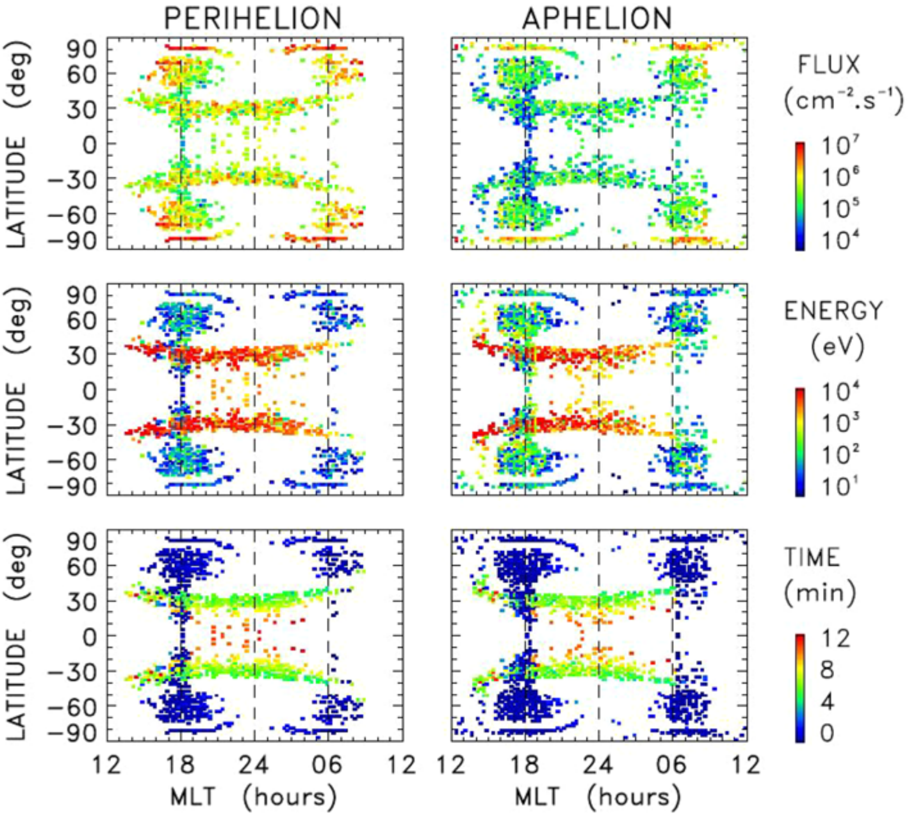

Fig. 34 Characteristics of precipitating Na^+ ions (*left*) at perihelion and (*right*) at aphelion. The panels from top to bottom show ion flux, average energy, and residence time in the magnetosphere (Delcourt et al. 2003)

netic clouds. CMEs are associated with flares and prominence eruptions and their sources are usually located in active regions and prominence sites. The basic characteristic of CME producing regions is closed magnetic structure. Recent studies on temporal correspondence between CMEs and flares provide arguments in favor of the so-called common-cause scenario, according to which flares and CMEs are different manifestations of the same large-scale magnetic process (Zhang et al. 2001). Although the details of this process still remain unclear, it definitely can be stated that an intensive flaring activity of a star should be accompanied by an increased rate of CME production. The probability of CME-flare association increases with the duration of a flare (Sheeley et al. 1983): $\approx$26% for flare duration $<$1 h; and $\approx$100% for flare duration $>$6 h. Multi-thermal structure of CMEs includes 1) coronal material in the front region ($\approx$2 MK); and 2) possibly a core from solar prominence material ($\approx 10^4$ K), or hot flare plasma ($\approx$10 MK).

The basic and widely considered characteristic of CMEs is their velocity, determined by tracking a CME feature in coronagraph image frames taken with a certain time cadence. According to the data from SoHO/LASCO, the velocity of solar CMEs ranges from tens of $\mathrm{km\,s^{-1}}$ to $>$2,500 $\mathrm{km\,s^{-1}}$ near the Sun, with an average value of about 490 $\mathrm{km\,s^{-1}}$ (e.g., Gopalswamy 2004). Due to the relatively large statistics ($>$8,000) of the considered SoHO/LASCO CMEs, the average ejecta velocity value can be considered as a representative quantity. It is also consistent with the results of other velocity measurement techniques applied to separate CME phenomena (Lindsay et al. 1999; Gopalswamy et al. 2001a, 2001b, 2004; Lara et al. 2004). Halo CMEs, a subclass of CMEs propagating toward the Earth, are currently believed to be the main drivers of space weather disturbances at the Earth. Compared to the general population of CMEs, halos have much higher average speeds of 1,004 km/s (Yashiro et al. 2004).

Besides the velocity of CMEs an additional important parameter for studying the plasma interaction with Mercury's magnetospheric-surface environment is the plasma density. Estimates of CME plasma density from white light (Vourlidas et al. 2002), radio (Gopalswamy and Kundu 1993), and UV observations (Ciaravella et al. 2003) give similar values of about 10^6 cm^{-3} at the distances ≈ 3–$5 R_{\mathrm{Sun}}$ which are consistent with the assumption of the coronal value of density of a CME material at the moment of ejection. At larger distances >30 R_{Sun} (i.e., >0.14 AU), the density and duration of ICMEs and associated MCs are measured in situ by spacecraft (Henke et al. 1998; Lepri et al. 2001). For the plasma density in MCs observed between 0.3–1 AU by the Helios satellites, Bothmer and Schwenn (1998) found a power law

$$n_{\mathrm{MC}} = n_{\mathrm{MC}}^0 \left(\frac{d}{d_0}\right)^{-2.4\pm 0.3}, \tag{21}$$

where d is the radial distance to the Sun in units of AU, quantity $n_{\mathrm{MC}}^0 = 6.47 \pm 0.95$ cm^{-3} is the MC plasma density at the near-Earth orbit, and d_0 is at 1 AU (Bothmer and Schwenn 1998). By using this power law one gets CME number density values at periherm of about 80–260 cm^{-3} and about 45–130 cm^{-3} at about 0.38 AU.

Finally, another important characteristic of CME activity and its influence of Mercury's environment is the CME occurrence rate. The data from Skylab, SMM, Helios, Solwind, and SoHO indicate a correlation between sunspot numbers (SSN) and the CME occurrence rate (Hildner et al. 1976; Howard et al. 1986; Webb and Howard 1994; Cliver et al. 1994; Cyr et al. 2000; Gopalswamy et al. 2003). At the same time, SoHO/LASCO observations found that although there is an overall similarity between the SSN and the CMEs occurrence rates, there are some differences in details. The most recent SoHO/LASCO observations give a CME occurrence rate ≈ 0.8 CMEs/day for solar minimum and ≥ 6 CMEs/day for solar maximum.

These numbers are consistent, but a bit higher as compared to previous estimations (Hildner et al. 1976; Webb and Howard 1994; Cliver et al. 1994), which is attributed to the better sensitivity and the high dynamic range of the LASCO coronagraphs. Focusing on halo and fast-and-wide CMEs may help estimate the occurrence rate of ICMEs at Mercury. First, full halo CMEs account for about 3.5% of all CMEs detected by SOHO. Second, the fraction of fast-and-wide CMEs ranges from 2% (1996) to 6% (2003, past solar maximum) of the total SOHO count (Gopalswamy 2004). Combining the observed occurrence rates of all CMEs originating at the Sun with the aforementioned fraction of fast-and-wide CMEs, and assuming that a typical halo has angular width of 120 degrees, we should expect 2–3 ICMEs/year at solar minimum and about 44 ICMEs/year (one every nine days) at solar maximum to impact Mercury.

Kallio and Janhunen (2003) studied the precipitation of the protons related to a MC or CME event with a proton density of about 75 cm^{-3} and a velocity of about 800 km s^{-1} with a self-consistent quasi-neutral hybrid model. In their simulation the particle flux of the plasma protons was calculated self-consistently with the kinetic model. By increasing solar wind dynamic pressure to about 10^{-5} Pa it was possible to push the magnetopause toward Mercury's surface, in agreement with MHD model runs of Kabin et al. (2000). In such a

Fig. 35 3D exosphere calculation by using the test particle model for sputtered Ca atoms as a function of planetary distance in units of km for ordinary solar wind conditions (*left panel*) and during a simulated MC collision with Mercury with a plasma density of 75 cm^{-3} and a velocity of about 800 $\mathrm{km\,s}^{-1}$

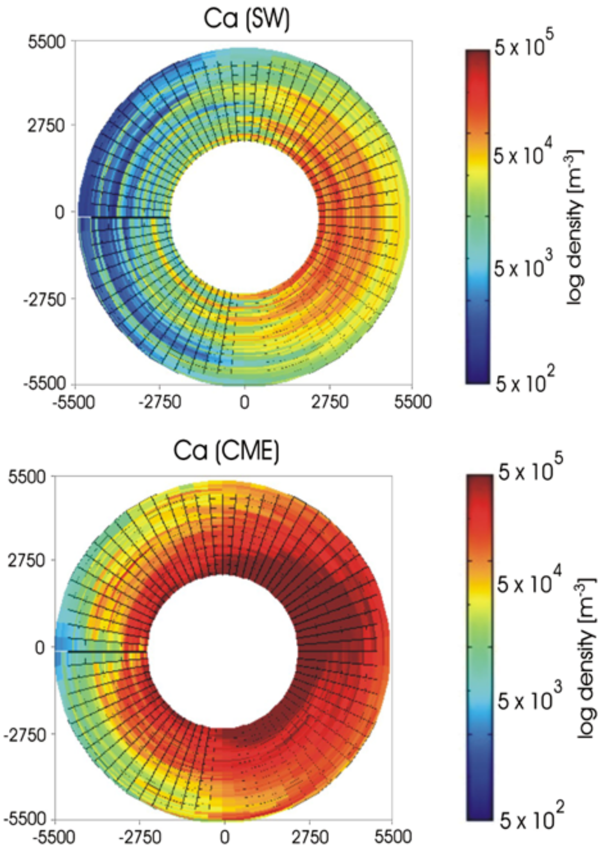

case an intense H^+ ion precipitation with fluxes up to about 10^9 $\mathrm{cm}^{-2}\,\mathrm{s}^{-1}$ was found near the subsolar point.

Figure 35 shows an equatorial cut of sputtered exospheric Ca atoms during ordinary solar wind conditions where larger fluxes of solar wind protons only precipitate to the surface around Mercury's cusp regions (Massetti et al. 2003; Kallio and Janhunen 2003) and the MC event discussed earlier and studied by Kallio and Janhunen (2003). One can see that due to the large affected surface area the exosphere should be refilled by Ca atoms during the MC collision.

One can see from Fig. 35 that the results which give much denser and more distributed exospheric number densities of sputtered surface elements during expected collisions with CMEs or MCs are pertinent to future measurements on the Messenger and BepiColombo missions, which will be instrumented to observe the released exospheric particles.

Kinetic energies of solar wind ions are, on average, 1 keV/amu, where the sputtering efficiency peaks. Sputtering by H^+, which accounts for 85% of the total kinetic energy carried by the solar wind, is relatively inefficient. On average, He^{2+} accounts for about 13% of the kinetic energy carried by the solar wind, and is generally assumed to account for most of the space weathering effects. However, although heavy ions ($Z > 6$) account for only about 2% of the kinetic energy carried by the solar wind, they also carry ∼1 keV each in potential energy due to ionization into a high charge state. The charge state of the impinging ion has little effect on the sputter efficiency of highly conducting targets (conductors and semiconductors), but has considerable effect on some insulators as discussed earlier (Aumayr and Winter 2004).

3.7 Sputter Effects on Surface Chemistry

Sputtering of the surface by any of the mechanisms discussed earlier may affect the topmost layer of the regolith. Ion implantation of solar wind ions occurring for billions of years may change the predominant apparent chemistry to more reflect the solar wind than the pristine composition from Mercury's origin. In addition, new chemical compounds may be made. Production of sodium and water by proton sputtering of sodium-bearing silicates was considered by the following mechanism (Potter 1995)

$$2\mathrm{H} + \mathrm{Na_2SiO_3} \rightarrow 2\mathrm{Na} + \mathrm{SiO_2} + \mathrm{H_2O}. \tag{22}$$

The supply rate of water molecules is half the supply rate of Na by this process. Since the free energy of this reaction is -4.7 kcal/mole, it will proceed spontaneously; however, the activation energy is unknown. Chemical reactions, either on the surface or in the atmosphere, can enhance the loss rates of the reaction products if the reaction products are created with enough energy to escape. Very little work has been done to quantify rates for chemistry as a source or loss process in the context of planetary sciences.

In laboratory research such processes are investigated and are referred to as plasma-assisted etching, or chemically enhanced physical sputtering (e.g. Winters et al. 1983; Winters and Coburn 1992). These processes are used for a large variety of industrial and laboratory applications. Energetic ions and electrons of the plasma induce strong changes in the surface chemistry. Plasma-assisted etching involves the interaction of a plasma discharge with a solid surface to produce a volatile product. Laboratory research aims to produce product molecules at the surface that are weakly bound to the surface to enhance the sputter yield for micro-fabrication. The reaction can be divided into three steps: 1) the adsorption/implantation of external particles, 2) the product formation, and 3) the removal of the product from the surface.

Physical sputter theory predicts that the sputter yield is inversely proportional to the binding energy of the species to the surface (Sigmund 1969). Energy distributions under the conditions of chemical sputtering have been measured in the laboratory (Haring et al. 1982) and two components in the energy distribution have been identified (Winters and Coburn 1992). The first component is very well described by the energy distribution for physical sputtering (see (15)). The second component, however, peaks at energies between 0.1 and 0.5 eV (indicative of a low surface binding energy) and can be described by a Maxwellian distribution, and shows higher yield. Thus, the chemical alteration increased the total sputter yield from the surface. In laboratory experiments the interaction of halogens is studied mostly, but there are a few investigations where the increased sputter yield of silicon by hydrogen ion impact is reported (Winters and Coburn 1992, and references therein).

Such a low binding energy means that the created species can also be released via thermal desorption, as is the case for the example of Na and water given above. Thus the chemical alteration of Mercury's surface by precipitating ions and the later release of volatiles (e.g., Na and water) can also occur with considerable delay. A possible scenario is ion implantation when the surface is cold (e.g., at the nightside). At a later time, when the surfaces warms up because of solar insolation, the thermal release of the such created volatiles may occur.

Chemical reactions induced by solar wind ions impinging on the surface undoubtedly occur on Mercury. Earlier, we discussed the example of a source for water molecules and atomic sodium. The study of chemistry on the surfaces of bodies exposed to the solar wind is in its infancy, and more so the effects this has on the sputter yields.

4 Thermal Vaporization of Alkali Atoms

The vapor pressure of a gas in thermal equilibrium with a liquid is given by

$$P = P_0 \exp\left(-\frac{l}{RT}\right), \tag{23}$$

where l is the latent heat per mole, R is the gas constant and T is the temperature in Kelvins. In the case of vaporization of an adsorbed volatile from a solid surface, the rate constant for thermal desorption is described as

$$k_{\mathrm{des}} = A_{\mathrm{des}} \exp\left(-\frac{E_{\mathrm{des}}}{kT}\right), \tag{24}$$

where A is a pre-exponential vibrational frequency, and E_{des} is the desorption energy. The value of the pre-exponential, the vibrational frequency, most often used is 10^{13} s^{-1} (e.g., Hunten et al. 1988) but in fact it can vary from 10^4 to 10^{23} s^{-1} (Holmlid 1998). The extremely large range for the preexponential term is due to the large number of physical processes actually involved in thermal desorption: including diffusion to and from the bulk rock or grains, surface diffusion between sites with different desorption energies, electronic excitation and de-excitation, jumps during the near-desorption in excited states.

Spatially resolved studies of iron-rich minerals show the complexity of real metal oxide surfaces: for instance, the desorption energy of alkali atoms is changed radically by the addition of other atoms in low concentrations. The thermal barrier for K desorption from the same type of mineral can range from 0.83 eV to 2.35 eV by adding 2 wt% Mn to the material (Kotarba et al. 2004). Values quoted in the literature for desorption energy of Na atoms range from 1.1 eV (Hunten and Sprague 1997), 1.8 eV (Madey et al. 1998) and 2.7 eV for metal and metal oxide surfaces (Holmlid and Olsson 1977). In the Monte Carlo study of Leblanc and Johnson (2003) an average desorption energy of 1.85 eV was used with a preexponential of 10^{13} s^{-1}. Holmlid (2006) suggested that this pre-exponential is much too large, and that the desorption energy of alkali atoms from any real oxide mineral is unlikely to be much smaller than 2 eV.

The rate of thermal desorption from a surface is in fact rate limited by the slowest process acting in the chain of events leading to desorption (see Fig. 36). For the surface of Mercury, Killen et al. (2004b) concluded that the rate-limiting process for thermal desorption from the surface of Mercury is diffusion of atoms from the bulk of the grains. This conclusion is consistent with the conclusions of Leblanc and Johnson (2003) that thermal desorption rapidly depletes most of the sunlit surface of Mercury of adsorbed atoms.

The measured temperature for the sodium atmosphere is high, about 1,200 K, whereas a high adsorption energy would imply efficient sticking at the surface, and hence rapid thermal accommodation to the surface temperature (Holmlid 2006). However, observations of the variation of sodium D2 intensities with true anomaly angle imply that the sticking coefficient is quite small, on the order of 0.15 (Potter et al. 2006). This seems to be inconsistent with a high adsorption energy. It is not inconsistent with a lower adsorption energy, and an efficient

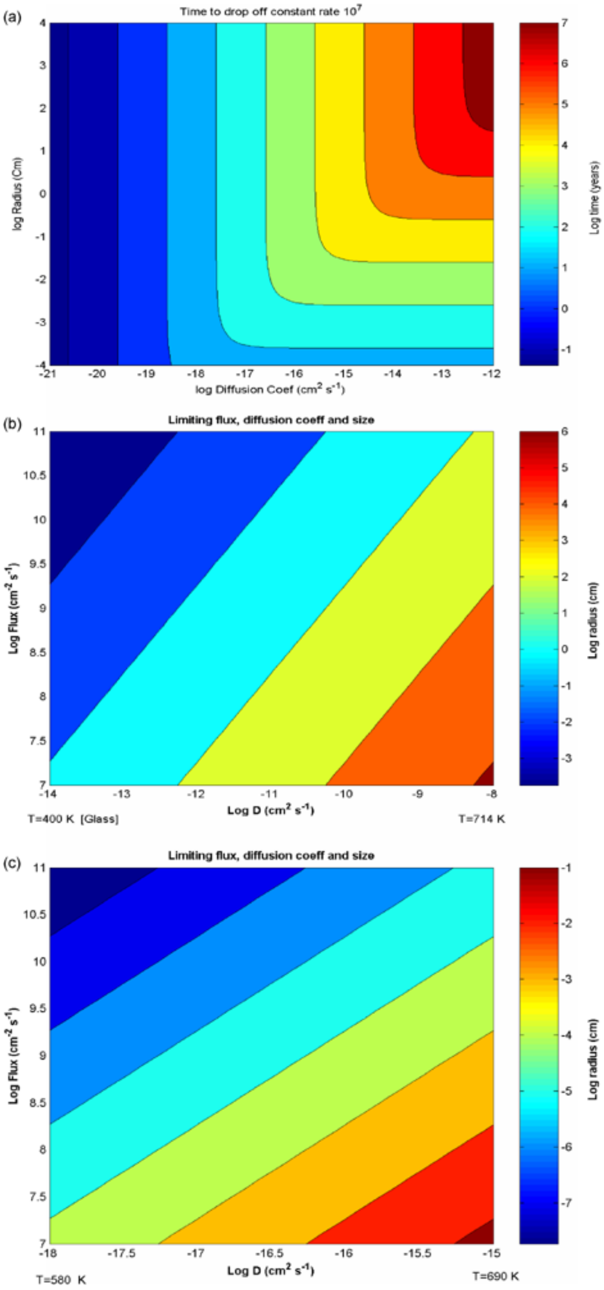

Fig. 36 (**a**) Shows the time required for the flux of solute from the grain interior to the grain surface to fall below a constant value of 10^7 cm^{-2} s^{-1} (the maximal required at the subsolar point to maintain the exosphere) as a function of temperature (diffusion coefficient) and grain radius. We show the limiting size grains (radius in cm, color coded) that can maintain the thermal fluxes until half the solute is depleted for (**b**) glass and (**c**) crystalline minerals: 100 cm (glass) and 1 μm (mineral) at perihelion, and 10^3 cm (glass) and <1 μm (mineral) at aphelion (Killen et al. 2004b)

loss of adsorbed states, as described by Killen et al. (2004b) and by Leblanc and Johnson (2003).

In this case the source process for Na and K to the exosphere would be dominated by PSD, ion-sputtering and impact vaporization, which are all capable of ejecting the atoms from the bound state. The source rates for all processes other than impact vaporization, which accesses a depth equal to several impactor diameters, depends on the availability of atoms at the extreme surface. To maintain a long-term supply to the exosphere by PSD or ion-sputtering, atoms must diffuse from the bulk of the rock or grain to the extreme surface.

The long-term source rates are therefore limited by the diffusion rates. These are dependent not only on temperature, but grain size and lifetime of the grain on the surface. Thermal vaporization at the subsolar point on Mercury is very efficient, given a supply of adsorbed atoms at the extreme surface (e.g. Leblanc and Johnson 2003). Fluxes are calculated using (Crank 1975)

$$\frac{Dt}{a^2} = \frac{2}{\pi} - \frac{2}{\pi}\left(1 - \frac{\pi F}{3}\right)^{1/2} - \frac{F}{3}, \tag{25}$$

where F is the fraction of solute lost at time t from a sphere of radius a. D is the diffusion coefficient and the solute is assumed to be initially uniformly distributed.

To obtain the flux per unit surface area of the planet at time, t, we solved (25) for F, took the time derivative of F and multiplied by the initial amount of solute and divided by the cross-sectional area of the grain. Thus the loss rate per unit cross-sectional area is given by

$$\frac{\mathrm{d}n}{\mathrm{d}t} = \frac{\frac{4}{3}\pi a^3 f_{\mathrm{Na}} \rho \frac{\mathrm{d}F}{\mathrm{d}t}}{\pi a^2}. \tag{26}$$

Once the adsorbed atoms have evaporated, the source rates drop to the values at which atoms can be supplied to the surface by diffusion. Results show that large thermal fluxes could be maintained by diffusion from hot glassy spheres as long as a mechanism exists for desorption of the atoms from the surface.

Any glass sphere smaller than the limiting size would be able to maintain the flux. For high fluxes, unreasonably small grains or high diffusion coefficients are required. Progressively smaller grains supply atoms to the surface at faster rates but for shorter periods of time, as the grains become depleted of volatiles (Killen et al. 2004b). The upper few µm of the Moon is turned over about once in 10^3 years (Heiken et al. 1991). We expect the turnover rate at Mercury to be about ten times that at the moon, since the impact flux is about ten times that at Earth orbit.

Thus a µm-sized grain will sit on the surface of Mercury for about 100 years. If the diffusion rate of a µm-sized grain drops to 10^7 cm^{-2} s^{-1} in one month, then a “thermal” vaporization rate of 10^{11} cm^{-2} s^{-2} is sustainable for less than 0.1% of the µm-sized grains on the surface, and none of the larger grains (Figs. 36a,b). It is concluded that the exospheric rate required to maintain the observed exosphere 10^7 cm^{-2} s^{-11}, is therefore the limiting value governed by diffusion of atoms to the surface of grains and by the gardening rate.

Radar bright spots near the poles of Mercury discovered in 1992 (Harmon and Slade 1992) were attributed to water ice. Numerous studies concluded that water ice is stable in permanently shadowed craters near the poles of Mercury (Paige et al. 1992; Ingersoll et al. 1992). It is intriguing that 13 radar bright features were found between 70° and 80° latitude (Harmon et al. 2001). All of these features are small, consistent with the limited amount of permanent shading expected at these latitudes. It has been suggested that the volatile in the cold traps is not water ice but in fact may be sulfur (Sprague et al. 1995) or cold silicate (Starukhina 2000).

We should ask ourselves the question: Is thermal vaporization a loss process for water? In other words, is evaporation a reversible or irreversible process? One must in fact show that vaporization is an irreversible process to rule out the possibility of its presence at a given latitude since atoms cannot be carried away by winds or other processes on an atmosphereless body. Unless the atoms are lost by an irreversible process such as ionization and entrainment into the solar wind, or chemical reactions, they must eventually return to the cold traps. Further, as pointed out by Holmlid (2006), the adsorption energy and preexponential terms are highly influenced by the local composition and charge state of the surface, which changes rapidly near the terminator for instance.

5 Loss Processes

Loss of atoms from the exosphere must be defined into categories of loss: reversible loss processes (sticking to the surface or ionization followed by impact with the surface and neutralization) and irreversible loss processes (Jeans escape and ionization followed by crossing the magnetopause boundary and entrainment into the solar wind). Reversible loss processes must be further characterized as long-term loss, such as burial or chemical reaction into a bound state with a large binding energy, or short-term loss such as adsorption on the surface of grains. Jeans escape is an irreversible loss process, but photoionization may or may not result in permanent loss. Sticking to the surface results in loss from the exosphere but not from the regolith. These different types of loss processes will be discussed in the following.

5.1 Jeans Escape

Only H and He have significant rates of Jeans escape at the ambient surface temperature on Mercury (Hunten et al. 1988). However, with the exception of thermal vaporization, the source processes populating the Hermean exosphere create non-thermal populations and the mean energy is species dependent. The mean velocities of atoms ejected by ion-sputtering may be above escape velocity, 4.25 km/s, and will depend on the binding energy of the atom in the substrate, and its mass (Table 9). As pointed out by Holmlid (2006) the binding energy of a given atom will depend not only on the particular mineral in which it is found, but also on the surrounding conditions. This is particularly important for a surface that is highly subject to space weathering.

The mean velocity of Ca atoms observed in the Hermean exosphere is about 3.5 km/s (Killen et al. 2005), consistent with the expected mean velocity for an ion-sputter source. If the main source of Mg and Al to the exosphere is ion-sputtering, then the bulk of the source would be lost by Jeans escape. Killen et al. (2005) suggested that dissociation of a calcium oxide could also account for the high velocity observed for calcium in the Hermean exosphere.

The temperature of meteoritic vapor is often described as being quite hot, perhaps as high as 6,500 K. However, only the initial vapor plume seen by the Deep Impact spacecraft in the first few seconds was hot (1,000–3,000 K), implying that a rapid cooling takes place in the dense fireball and possibly in the regolith (A'Hearn et al. 2005). The bulk of

Table 9 Mean velocity of an ion-sputtered source for selected atomic species

Species	v_{mean} [km/s]
Mg	4.5
Al	4.3
Ca	3.5
Fe	3.0

the vapor—that in the ejecta curtain—which is composed of excavated material, was at ambient temperature. The vapor resulting from micrometeoritic bombardment may cool by multiple collisions with the regolith as the micrometeoroids deposit their energy below the surface.

5.2 Photoionozation

Photoionization is an irreversible loss process if the ions cross the magnetopause and become entrained in the solar wind. Killen et al. (2004a) suggested that half of the photoions produced near the surface return to the surface where they are neutralized. An east-west electric field produces an asymmetric escape pattern such that those ions created on the dusk side reimpact on the dawnside, and those ions created on the dawnside escape across the magnetopause boundary or impact the nightside. However, the escape rate is higher as the ions are produced at successively higher altitudes.

Photoionization rates of many likely exospheric species are known. Rates for He, C, N, O, F, Na, S, Cl, Ar, Xe, OH were published by Huebner et al. (1992) and for Ca by Killen et al. (2005). Photoionization rates for most refractory species (e.g., Mg) have not been published. In any case, the energy with which refractory species are ejected by the two mechanisms capable of ejecting refractory species, ion-sputtering and meteoritic vaporization, will be energetic enough to eject most of the atoms at velocities exceeding escape velocity. Those refractories that do not directly escape will probably stick to the surface on impact. Thus their photoionization rates are not pertinent to their lifetimes in the exosphere.

The sodium ionization rate is controversial because of the discrepancy between the experimental and theoretical cross-sections, and further because there are theoretical calculations that agree with the experimental value. The Combi et al. (1997) value is quoted because it is commonly used in the cometary community, and the observed cometary abundances agree with calculations when this value is used for the ionization rate. However, the discovery of the sodium tail on comet Hale-Bopp (Cremonese et al. 1997) and the high-resolution spectroscopy performed along the tail was used to calculate a new value of photoionization lifetime for the neutral sodium atom that confirmed the value suggested by Huebner et al. (1992). The model used for the comet works also on the sodium tail of Mercury showing that it does not depend on the object observed.

The rates for sulfur are theoretical (Huebner et al. 1992). Rates from Kumar (1982) are 50% higher. The calcium ionization rate was calculated by Walter Huebner and communicated to the author. All other rates are from (Huebner et al. 1992). The photoionization rate is not the limiting rate if atoms stick to the surface.

5.3 Charge Exchange

A charge-exchange process may occur when an energetic ion collides with a exospheric neutral particle (target). In the interaction, an electron and a small amount of kinetic energy are exchanged between the neutral and the ion; the net result is an energetic neutral atom (ENA) and a thermal ion. The target (ionized) is scattered at an approximately perpendicular angle with respect to the projectile path; the newly created ENA retains approximately both the energy and the direction of the colliding energetic ion. The energy defect of the process is equal to the difference of the two atomic ionization potentials (for complete discussions see, e.g., Hasted 1964). Charge-exchange is a resonance process, which can be symmetrical (if the species of the ion and the neutral are the same) or accidental (Stebbings et al. 1964; Hasted 1964). The cross-section varies with species and energy and is of the order of 10^{-14}–10^{-17} cm^{-2}.

Table 10 Solar photo ionization rates at 1 AU

Species	Rate coefficient (quiet sun) $[\mathrm{s}^{-1}]$	Rate coefficient (active sun) $[\mathrm{s}^{-1}]$
H	7.26×10^{-8}	7.1×10^{-8}
He	5.25×10^{-8}	1.51×10^{-7}
$O(^3P)$	2.12×10^{-7}	5.88×10^{-7}
$O(^1D)$	1.82×10^{-7}	5.04×10^{-7}
$O(^1S)$	1.96×10^{-7}	5.28×10^{-7}
Na	1.62×10^{-5}(e) 5.92×10^{-6}(t) 5.40×10^{-6}(a)	1.72×10^{-5}(e) 6.42×10^{-6}(t)
$S\ (^3P)$	1.07×10^{-6}	2.44×10^{-6}
$S(^1D)$	1.08×10^{-6}	2.46×10^{-6}
$S(^1S)$	1.05×10^{-6}	2.31×10^{-6}
Ar	3.05×10^{-7}	6.90×10^{-7}
K	2.22×10^{-5}	2.36×10^{-5}
Ca	7.0×10^{-5}(b)	7.8×10^{-5}
$OH \rightarrow O(^3P) + H$	6.54×10^{-6}	7.17×10^{-6}
$OH \rightarrow O(^1D) + H$	6.35×10^{-7}	1.51×10^{-6}
$OH \rightarrow O(^1S) + H$	6.71×10^{-8}	1.64×10^{-7}
$OH \rightarrow OH+$	2.47×10^{-7}	6.52×10^{-7}

(e)experimental

(t)theoretical

(a)Combi et al. (1997)

(b)Huebner (personal communication, unpublished)

Charge exchange at Mercury may occur due to solar-wind plasma (Mura et al. 2005) as well as due to planetary ions. Generated neutrals have typical energies of 1 keV or more; hence, such neutrals are no more trapped in ballistic orbits and the result is a net loss from the planet. This process mostly occurs in the dayside and dawnside regions close to the planetary surface (Mura et al. 2005); in general, the H-ENA production rate for unit length reaches values up to 10 ($\mathrm{cm}^{-2}\,\mathrm{s}^{-1}\,\mathrm{sr}^{-1}\,\mathrm{m}^{-1}$), close to the dayside planetary surface. It has been estimated that, approximately, less than 1% of the solar wind plasma circulating inside the magnetosphere of Mercury experience charge-exchange (Mura et al. 2005); the related CE loss rate, cumulated on all neutral species, is between 10^{22} and 10^{24} s^{-1}, which is, on average, small if compared to other loss mechanisms.

Figure 37 shows simulated fluxes of ENA coming from different directions (ENA images), as "seen" from a vantage point in the nightside, in a "fish-eye" projection. The fluxes are integrated between 1–10 keV. The intense fluxes coming from the dawnside of the planet (right side of the picture) are generated from westward drifting solar wind protons.

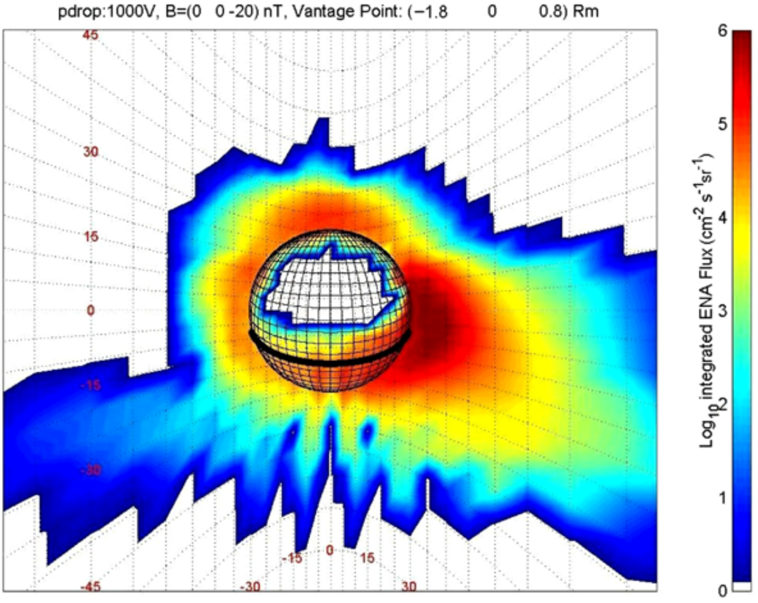

Fig. 37 Simulated ENA images, from a vantage point in the nightside (1.8, 0, 0.8 R_{M}). Color is coded according to ENA flux, integrated between 1 and 10 keV. From Mura et al. (2005)

5.4 Gardening

Gardening, fragmentation and burial of the regolith, has been studied extensively for the Moon (Heiken et al. 1991). Repetitive impacts agitate the surface by fragmenting, tumbling, burying and exhuming individual grains. The layer called the regolith is continuously churned. Although numerous small impacts homogenize the upper part of the regolith, a major role is played by the larger impacts in excavating previous sedimentary layers, fragmenting rock layers and depositing fresh material onto the surface. The number of times the lunar regolith has been turned over versus depth was calculated using results of laboratory cratering experiments in fine grained unconsolidated targets (Gault et al. 1974), and is given as a turnover versus depth as a function of time.

On the Moon, a depth of almost 1 cm is overturned once in 10^6 years with 50% probability (Heiken et al. 1991, p. 87). If the meteoritic influx scales as $1/R^2$ with distance from the Sun, then the rates at Mercury are on average 6.7 times those at the Moon, and the turnover times would scale as 0.15. Thus a layer of regolith 1 cm deep on Mercury should be overturned in 1.5×10^5 years with 50% probability. Turnover rates are important for long-term renewal of material at the extreme surface. Survival times versus grain size were estimated for the Hermean surface by Killen et al. 2004b, and compared with the time at which the diffusive flux of sodium from the grain interior to the surface would drop to 50% of its initial rate at a given prescribed rate (Fig. 38). This figure shows that the observed sodium exosphere would be sustainable, even if all of the volatile loss were irreversible, because fresh material will be supplied by regolith turnover before the volatiles are removed.

Fig. 38 Time it takes for a grain of a given radius to lose 50% of its solute at a given rate between 10^4–10^7 $cm^{-2}\,s^{-1}$. The *open circles* are lifetimes of grains on the Moon, and the *crosses* are the estimated lifetimes on the surface of Mercury, with the assumption that rates are approximately an order of magnitude faster on Mercury. This plot is a two-dimensional cut through a three-dimensional therefore temperature may vary across the plot

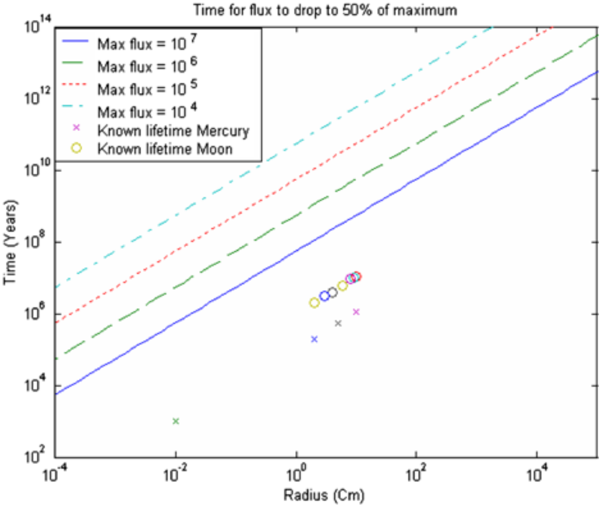

6 Space-Based Observations and Expected Results

The ESA cornerstone BepiColombo/MPO is planned to fly around Mercury in a polar orbit, with 400 km periherm and 1,500 km apoherm; the orbital period is about 2.3 hours. Two instruments in the MPO payload are mainly devoted to observing the exosphere: the FUV-EUV spectrometer, PHEBUS, and the comprehensive suite for particle detection, SERENA. The combination of these two experiments on BepiColombo will be an unprecedented opportunity to perform a detailed analysis of the exosphere composition and vertical profiles.

6.1 The BepiColombo/MPO/PHEUBUS UV Spectrometer

The BepiColombo/MPO/PHEBUS UV spectrometer PHEBUS is a dual FUV-EUV spectrometer (see the ESA BepiColombo webpage: http://www.rssd.esa.int/index.php?project=BEPICOLOMBO) working in the wavelength range from 55 to 315 nm plus a small two-channel detector used to measure potassium and calcium at 404 nm and 422 nm, respectively. This instrument is devoted mainly to the characterization of Mercury's exospheric composition and dynamics. In addition, some ionized species have emission lines in the spectral window; hence, this instrument will potentially contribute to the identification and characterization of the exo-ionosphere.

Thanks to the remote sensing of the exosphere, PHEBUS will provide measurements of density of many species (see Fig. 39) and their profiles at altitudes below the spacecraft periherm. Observations of the low altitude exosphere are particularly important for the characterization of the heavier atoms, such as N, C, Ne, Si, Fe, Mg and molecules like CO, that are unlikely to arrive at the BC/MPO orbit and that can be observed, most probably, solely by a remote-sensing instrument. PHEBUS will observe Na at 268 and 285.3 nm.

Since the observable emission lines are generated by the interaction between the solar photons and the exospheric atoms, the PHEBUS can only observe by looking toward the dayside or the terminator. In this sense, the two instruments, PHEBUS and the mass spectrometer, SERENA/STROFIO (see next subsection), are completely complementary. In fact, the combination of the PHEBUS remote sensing and the SERENA/STROFIO in situ measurements will provide a complete view of the day–night exosphere for almost all the foreseen components in a wide range of altitudes and Hermean conditions.

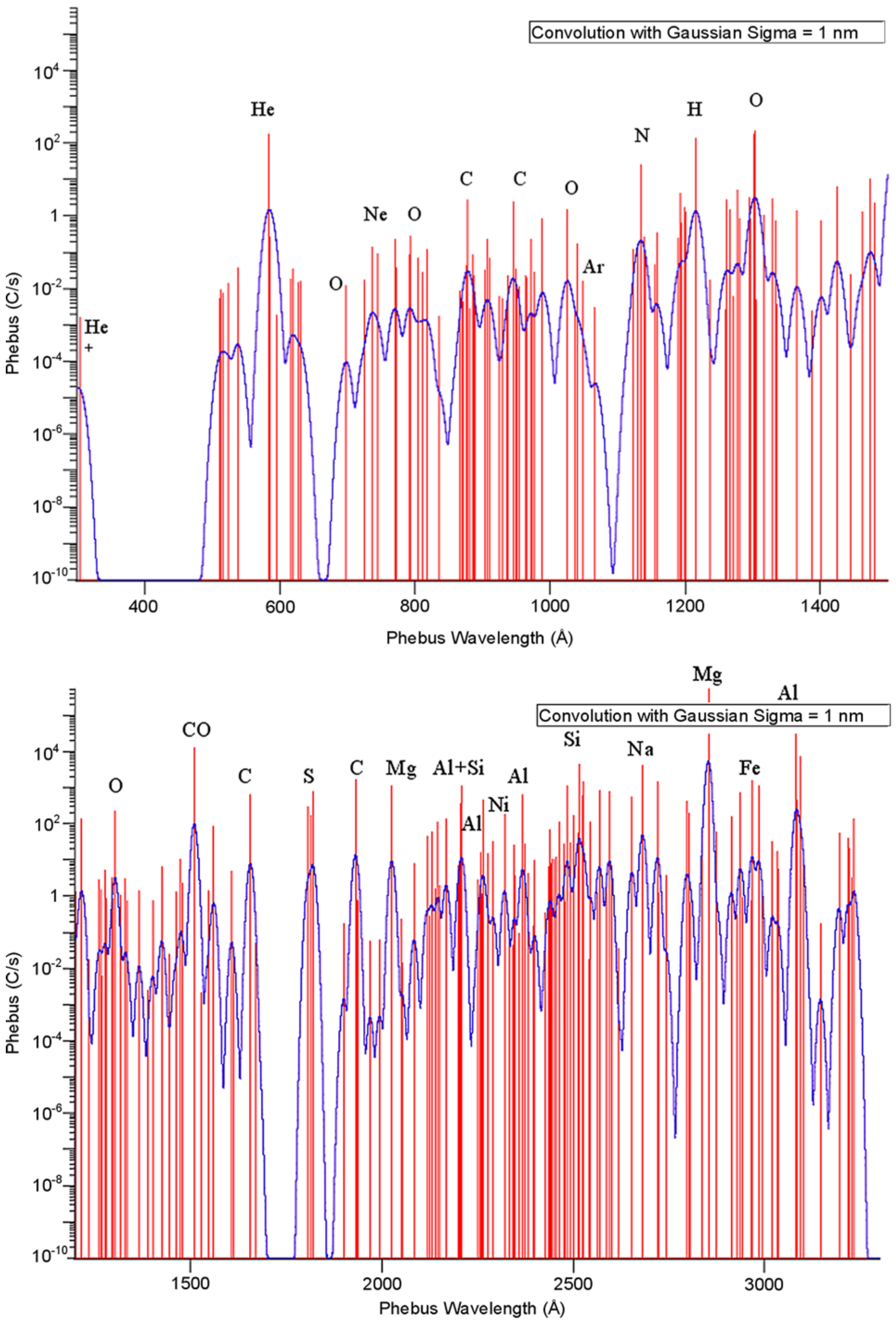

Fig. 39 PHEBUS EUV spectrum convolved with a Gaussian ($\sigma = 1$ nm)

6.2 The BepiColombo/MPO/SERENA Neutral Particle Detectors

A comprehensive suite for particle detection in the Mercury's environment, the SERENA instrument (see the ESA BepiColombo webpage: http://www.rssd.esa.int/ index.php?project=BEPICOLOMBO), is included in the MPO payload of the mission. This package consists of four units: STROFIO and ELENA will detect the neutral particles and measure their energies in the range from fractions of eV to a few keVs; MIPA and PICAM will measure and analyze ionized particles of planetary and solar wind origin from tens eV to tens of keV. ELENA (Emitted Low-Energy Neutral Atoms) is a neutral particle camera that investigates neutral gases escaping from the surface of Mercury, their dynamics and the properties of the related source processes. The ELENA sensor is a Time-of-Flight (TOF) detector, based on state-of-the-art choppers and mechanical gratings. The new development in this field allows unprecedented performances in timing and angular discrimination of low-energy neutral particles. STROFIO is a mass analyzer able to measure the neutral composition of the non-directional, thermal component of the exosphere.

The ELENA FOV (see Fig. 40, left panel) is always nadir-pointing, and most sectors look towards the planetary surface. In this way, the ELENA sensor will be able to detect the neutral flux coming from two different sources: charge-exchange ENAs, resulting from the interaction of solar wind and planetary plasma with the neutral exosphere, and ion-sputtering ENAs resulting from the precipitation of solar wind and planetary plasma onto the surface of Mercury. In general, it is possible to discriminate the neutral flux coming from those sources, since they have different typical energies and different generation regions.

In fact, instrumental simulations show that ELENA has both energy and angular resolution able to discriminate between those sources. The STROFIO FOV (see Fig. 40, right panel) points in the ram direction, so that low-energy exospheric particles will enter the sensor head due to the spacecraft motion. Regardless of the source generation process (provided that particles will have enough energy to reach the instrument location, see Fig. 41), STROFIO will count and identify the local exospheric components along the BepiColombo MPO orbit.

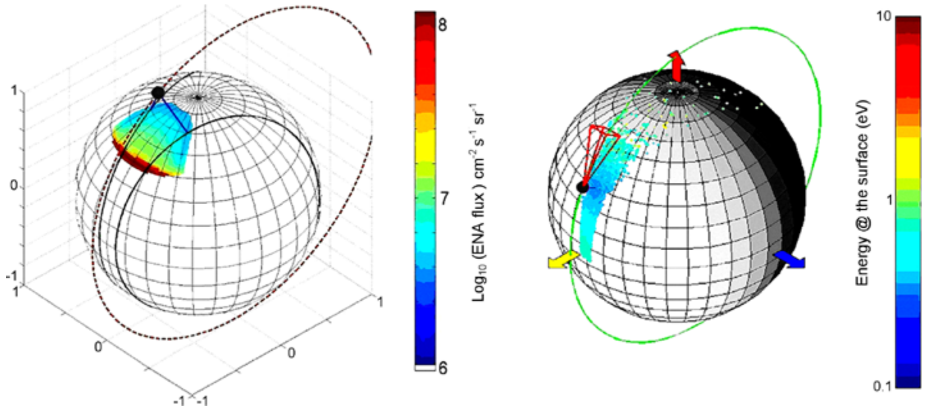

Fig. 40 ELENA and STROFIO field-of-views along the BC-MPO trajectories. *Left panel*: MPO orbit (*red dashed curve*); example of ELENA FOV (*blue lines*); boundaries of the projection of ELENA FOV onto the planetary surface (*green curves*); sample of the sputtering flux, due to s/w precipitation inside cusps, emitted from the surface (*color-coded map*). *Right panel*: MPO orbit (*green curve*; example of the STROFIO FOV (*red lines*) and source location of observable particle with the related energy are indicated

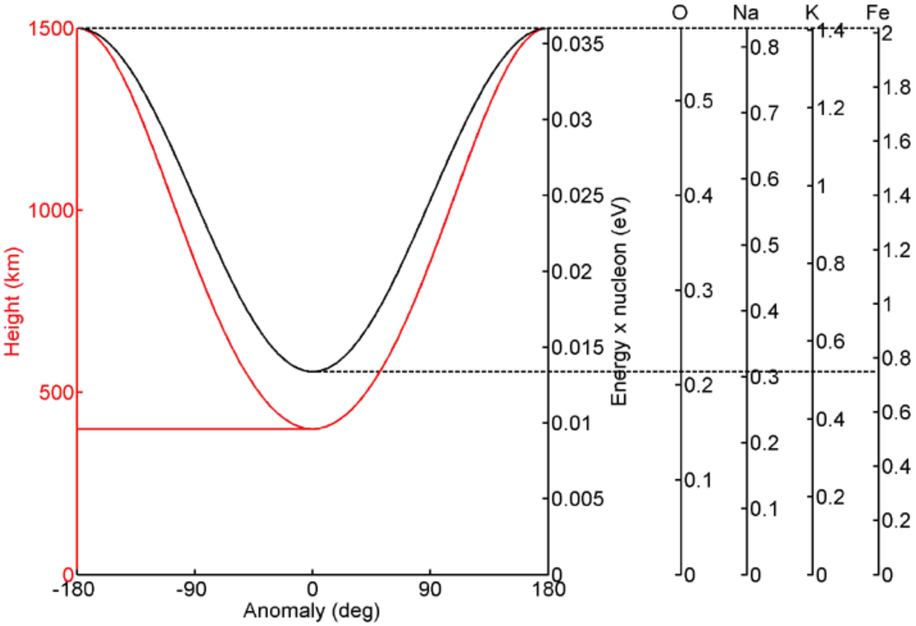

Fig. 41 MPO height function of anomaly angle (*red scale*, LHS). *Black scales* (RHS): minimum release energy necessary for a particle to get from the surface up to MPO orbit, for different species (O, Na, K, Fe), function of the anomaly angle

The major processes causing surface emission at Mercury are listed in Sect. 2. Among these processes, ion sputtering is the most effective in transporting exospheric gas up to BC-MPO orbit, and hence it is worth simulating the signal measured by SERENA. The ion-sputtering energy distribution function (f_s) (15) of the ejection energy usually peaks at few eV (Sigmund 1969; Sieveka and Johnson 1984), with a high-energy tail, up to approximately one hundred of eV. The value of the binding energy E_b determines the position of the spectrum peak, which is located at $E_b/2$; the projectile impact energy E_i determines the spectrum cut-off energy.

The spectrum differs from species to species but, in general, most of the ejected particles are able to reach the BC-MPO altitude. For sodium, as an example, the energy needed to reach the satellite altitude goes from 0.3 eV at S/C periherm, to 0.8 eV at S/C apoherm. If we assume the distribution given by (15), then a fraction above 90% of the ejected sodium is able to reach such altitudes. The detection of ion-sputtering ENAs deals with several scientific objectives of BC-MPO/SERENA (Milillo et al. 2005):

(1) particle loss-rate from Mercury's environment and surface emissivity;
(2) analysis of ion-sputtering process, since its yield, at high energy, is not well known; and
(3) analysis of proton precipitation, as a function of external conditions, performable in addition to other ion measurements.

The SERENA-STROFIO unit, in principle, is able to reveal sputtered neutral particles, depending on the relative composition of the S/C and particle velocity (see Fig. 42). Since the process is, with some approximation, stoichiometric, the mass analysis of the flux coming from a certain region on the surface gives information about the composition of the soil in that region.

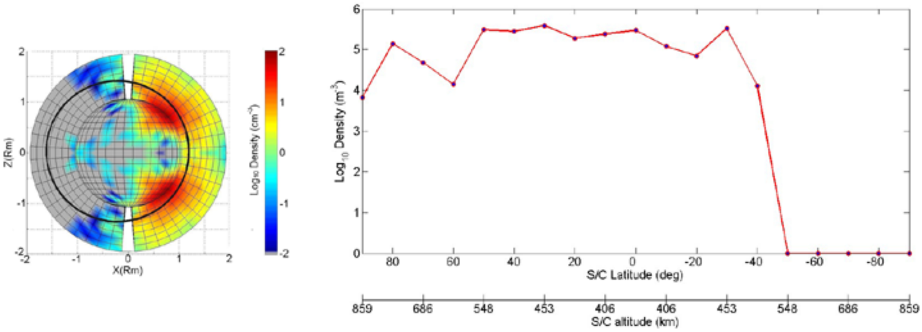

Fig. 42 *Left*: sample of ion sputtering density contours on the x–z plane (with trace of the MPO orbit). *Right*: actual STROFIO simulated data, according to instrument constraints. From Mura (2005)

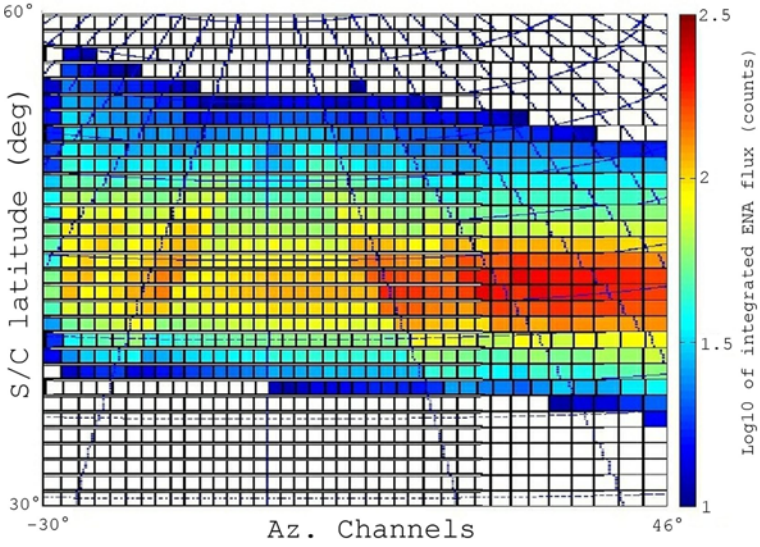

Fig. 43 2-D image of surface oxygen emission, obtained by the superimposition of 31 ELENA simulated measurements. Color is coded according to ELENA 30 s count rates, integrated over all energies above Oxygen escape energy. From Mura et al. (2006a)

On average, approximately 50% of the particles have more energy than the escape energy (few eV); those particles travel along quasi-linear paths, allowing a remote-sensing of the process via the SERENA-ELENA unit. The measurement of the total neutral flux, compared to the precipitating ion flux (observed by SERENA-MIPA), gives information about the effectiveness of the process (i.e., the process yield Y) and on the ion flux onto the surface, including its spatial and temporal distribution (see Fig. 43).

The 2D image of surface oxygen emission is obtained with the help of S/C motion, as a superimposition of 31 ELENA simulated measurements as the S/C is orbiting from 30°N to 60°N at 12:00 MLT (the periherm is at 0°, 12:00 MLT). The intense proton precipitation in the dayside, northern hemisphere results in an intense O-ENA production in the center of the global 2D image. In general, it is possible to have a global view of proton precipitation by means of ion-sputtered directional ENAs, with surface spatial resolution between 15 and

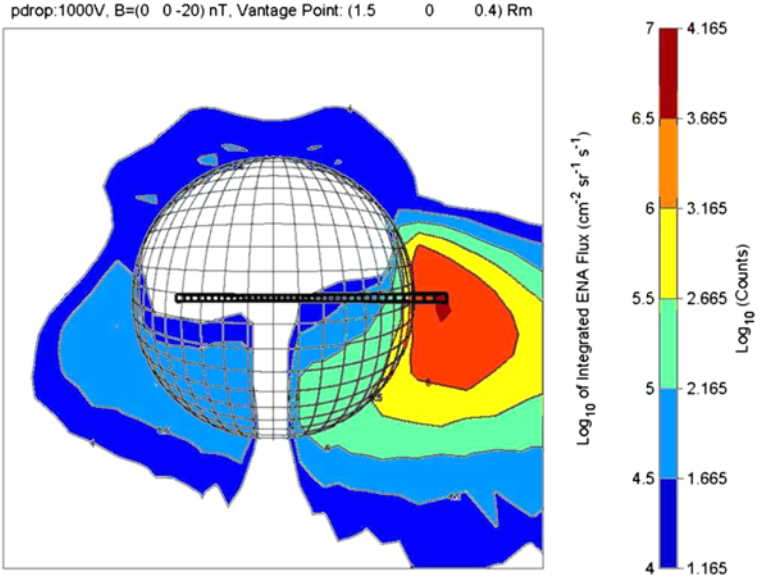

Fig. 44 Simulation of ELENA measurement, according to ENA flux in Fig. 37. FOV is shown by the *black bold grid*; each square represents an instrument sector (2° × 2°). From Mura et al. (2006b)

50 km, depending on S/C altitude. The color is coded according to ELENA 30 s count rates, integrated over all energies above Oxygen escape energy.

Under different IMF conditions, the configuration of the Hermean magnetosphere changes, so that the area of Solar Wind proton precipitation (and subsequent neutral release) consequently drifts and changes in size (see, e.g., Massetti et al. 2003; Kallio and Janhunen 2003). According to the simulations shown, the ion-sputtering ENA signal from the dayside is high enough to be detected by ELENA. In fact, the spatial and time resolution is good enough to monitor instantaneous changes of the magnetospheric configuration; the spatial resolution permits discrimination of surface emissivity variations. The intensity of the directional ENA signal originating from ion-sputtering depends on both proton precipitation flux and surface properties (composition and yield).

However, our simulations show that it is possible to discriminate between these two factors. In fact, proton surface precipitation has a typical spatial scale factor of about 100 km (Mura et al. 2006b). Since ELENA spatial resolution is lower (between 15 and 50 km), any small-scale spatial change in ion-sputtering ENA signal would be probably due to surface property variations. Moreover, temporal variability in the ENA signal should be ascribed only to modifications in the proton circulation properties.

Charge exchange neutrals have typical energies of 1 keV or more (see Sect. 5.4); this process mostly occurs in the dayside and dawnside regions (Mura et al. 2005), up to altitudes of hundreds of km (see Fig. 37). The H-ENA production rate for unit length reaches values up to 10 ($\mathrm{cm^{-2}\,s^{-1}\,sr^{-1}\,m^{-1}}$), close to the dayside planetary surface. This value, in some cases (depending also on the *line-of-sight* length), could lead to high values of H-ENA flux per steradian (up to 10^6 $\mathrm{cm^{-2}\,s^{-1}\,sr^{-1}}$). To facilitate the detection of such H-ENAs, the ELENA central axis is tilted, with respect to the S/C nadir axis, by 8°. In this way, at least three sectors point away from the planet, if the S/C is in a ∼15° orbital arc centered at the apoherm (see Fig. 44). In fact, the H-ENA signal is lower within sectors looking towards the planet, because the integration path is shorter. The S/C apoherm position will move, in longitude, during the MPO mission, thus allowing different, optimal vantage points.

As an example, from a nightside vantage point it is possible to detect the H-ENA signal generated from two different H^+ populations: the first one originates from protons that are precipitating into the cusp regions or circulating over the North pole. The second population originates from protons that have been drifted westward by the grad-B drift, from dayside to nightside through the dawn region. They reach low altitudes at their mirroring points, where exospheric densities are higher: they may produce an intense ENA signal that can be seen in the right side of the pictures. Charge-exchange ENA will be observed also by the other ENA sensor onboard the BC MMO satellite, with a more extended view due to the more distant apocenter (about 15,000 km).

The occurrence of impacts on Mercury by projectiles of the radius of 1 m seems to be not infrequent (2 events/year); such large projectiles would vaporize the regolith and reach a depth of meters, depending on the density and porosity of the regolith itself (Mangano et al. 2005). For the surface deeper layers are believed to be less contaminated by space weathering (Hapke 2001), the detection of the vaporized soil due to such impulsive events could be the only way to remote sense the real Hermean endogenous material.

One of the most interesting goals of the SERENA-STROFIO observations is the identification and detection of meteoroid impact vaporization process. In fact, as stated in Sect. 2, among the release processes active on Mercury, refractory species are released most efficiently by impact events (Gerasimov et al. 1998); hence, MIV could be a valid mechanism by which species like Mg, Al, and Si will be detected. Furthermore, larger projectiles (for instance, 1 m radius meteoroids that have a probability of two impacts/year) would vaporize the regolith reaching a depth of meters, hence layers less contaminated by space weathering (Hapke 2001), the detection of the vaporized soil due to such impulsive events could be the only way to remote sense the real Hermean endogenous material.

The frequent impact of meteoroids 10 cm in radius (more than two events/day, (Marchi et al. 2005)) makes them particularly interesting. In this case, the enhancement, depending from the considered species, varies from 1 to 4 orders of magnitude higher than the mean exospheric background values (Mangano et al. 2007). Durations are generally larger than 2,000 s, and their extension larger than 50° (calculated with respect to the center of the planet).

Such event will be observable by SERENA-STROFIO when the spacecraft flies over the impact zone during the event, and also by the UV spectrometer PHEBUS when the event happens in the daylight and along the instrument look direction. Figure 45 shows the simulated Na density observed by STROFIO as a function of time after impact and spacecraft position with respect to impact point. The signal is stronger when the impact is toward the ram direction (i.e., the look direction of the instrument); when the spacecraft pass the impact point fewer particles reach the instrument FOV.

In Fig. 46 the estimated counts rate of STROFIO for O, Mg and Na versus time in the case of a meteoritic impact under the spacecraft position are shown. These simulations seem to assure very high detectability, reaching almost the 100% of probability after only one month of monitoring from a probe in polar orbit and periherm at 400 km, apoherm at 1,500, as planned to be for the BepiColombo/MPO mission (Mangano et al. 2007).

Note that exospheric spatial inhomogeneities of refractory species with similar time scales could be generated by ion-sputtering. In this case the shape and intensity of the cloud would be significantly different as previously mentioned. Furthermore, the sputter-generated cloud would be characterized by an energy spectrum reaching higher energies (Wiens et al. 1997). The energy resolution of SERENA will allow discrimination between these two processes.

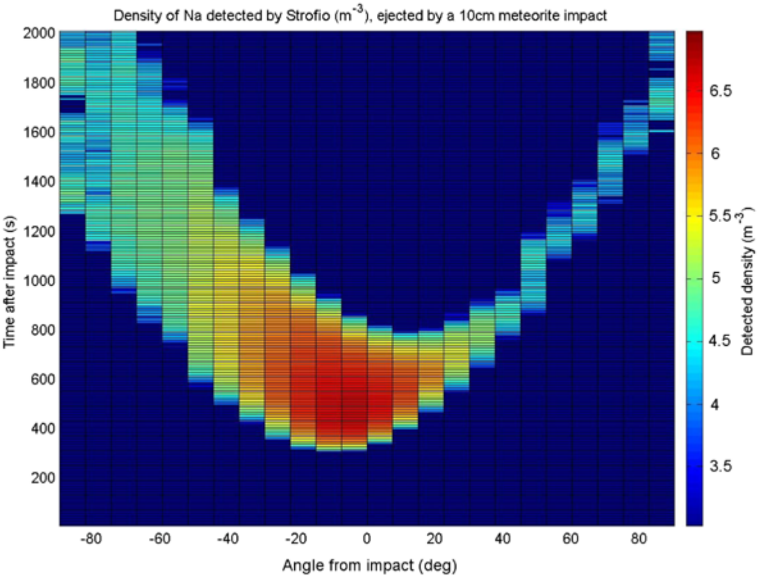

Fig. 45 Simulated Na density observed by STROFIO as a function of time after impact and spacecraft position with respect to impact point. The field of view of the instrument (20° × 20° in the ram direction) and the particle trajectories have been considered

6.3 3D Exospheric Modeling and Measurement Feedback

Mercury's exosphere consists of particles in ballistic orbits which originate from various release processes like thermal release, particle/photon sputtering and micrometeorite impact. The spatial distribution of a neutral exospheric component can be obtained by using a Monte Carlo single-particle model. In these models, it is assumed that the trajectory of a relatively small, but statistically representative, amount of test particles can reproduce the trajectories of all the real exospheric particles. A weight w is associated to each test particle, which takes into account the number of real particles that it represents.

For a given source process, the surface S where the process occurs is defined, then some number (N_{tp}) of test particles (usually some millions) are launched from randomly chosen starting points P_0 within $S : \Delta A = S/N_{tp}$, $w = j_0 \Delta A$, with j_0 being the initial flux through the surface element ΔA. The starting velocity $\mathbf{v}_0$ must be randomly chosen according to the velocity distribution function of the source; for an arbitrary velocity distribution function this can be done by using a Von Neumann (1951) algorithm. Alternatively, the surface of the planet can be divided into a number of elements and the initial flux of the sputtered particles can be prescribed for each element according to the composition of the soil and the sputter agents considered. In this case, several thousand particles are launched from each element corresponding to the initial conditions associated with the surface element and the contribution of each particle to the total number density is weighted according to the distribution function conforming to the release process considered. The initial elevation angle is determined via a given distribution while the azimuth angle is chosen randomly within the interval of 2π. Although the number of particles launched from each surface element is rather limited, their statistics are expected to approximately represent that of the many more particles forming the real exosphere of Mercury.

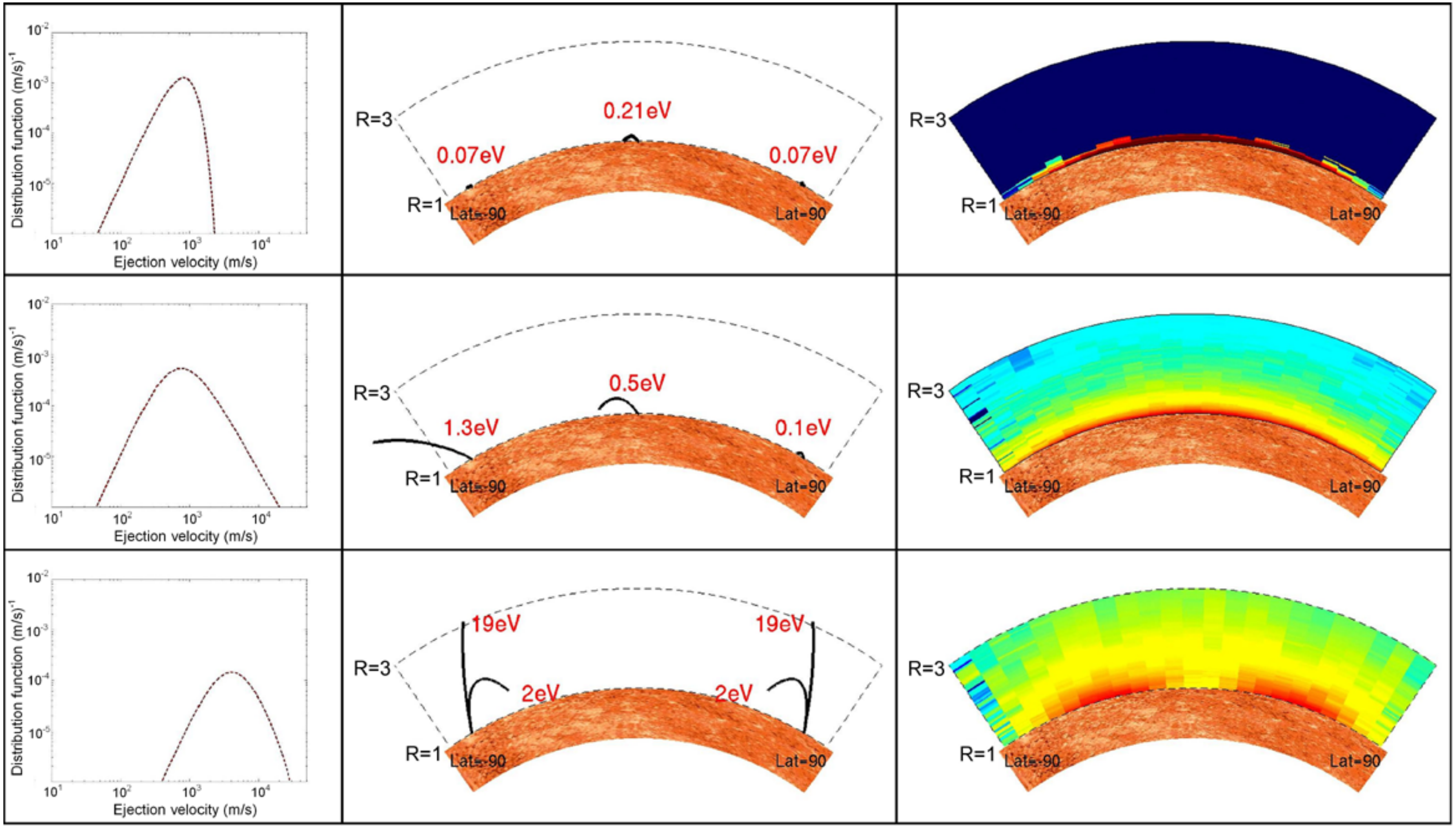

Fig. 46 Schematics of a Monte Carlo model simulation at Mercury. From the *left column*: Energy spectra of the source process; examples of trajectories, and simulated exospheres for different release processes (based on Mura et al. 2007). *Top row*: thermal desorption; *middle row*: photon-stimulated desorption; *bottom row*: ion sputtering. The planetary surface (*in brown*) represents a cut from −90° to 90° of latitude; the curvature is not to scale

The equations of motion are solved in spherical coordinates (r, Θ, ϕ) and are given by:

$$\begin{aligned} \ddot{r} - r\dot{\theta}^2 - r\sin^2\theta\dot{\phi}^2 &= -\frac{GM}{r^2}, \\ \ddot{\theta} + \frac{2}{r}\dot{r}\dot{\theta} - \sin\theta\cos\theta\dot{\phi}^2 &= 0, \\ \ddot{\phi} + \frac{2}{r}\dot{r}\dot{\phi} + 2\cot\theta\dot{\theta}\dot{\phi} &= 0, \end{aligned} \tag{27}$$

where M is the mass of Mercury and G the gravitational constant. The trajectories of the particles are followed until they either leave the simulation box or hit the surface of the planet. Particles falling back onto the surface are assumed to be trapped in the soil and are therefore excluded from further calculations. If necessary, additional forces can easily be incorporated into the model, for example, radiation pressure is expected to significantly affect the trajectories of Na and K and should therefore be taken into account. On the other hand, due to the slow rotation period of Mercury ($P \sim 59$ days) the acceleration caused by the Coriolis force might be neglected. Finally, exospheric species may eventually become ionized and removed from the exosphere. Such loss processes can be taken into account both by removing test-particles, or by decreasing w:

$$\frac{\mathrm{d}w}{\mathrm{d}t} = w(t)\sum_i \frac{1}{\tau_i}, \tag{28}$$

where τ_i is the lifetime of process i. To obtain the particle density, it is necessary to define a spatial grid Q. Each time a test particle crosses a grid cell, a quantity q is deposited there:

$$q = w(t)\Delta t, \tag{29}$$

where Δt is the time elapsed inside the cell. After all trajectories have been simulated, the spatial dependent number density n can then be determined by dividing Q by the volume of the cells:

$$n(r, \theta, \phi) = \frac{Q(r, \theta, \phi)}{\Delta V}, \tag{30}$$

further dimensions of the spatial grid can be used, as an example, to store the information about the energy of the particles.

At Mercury, several Monte Carlo models (e.g. Smith et al. 1978) have been proposed to reproduce the exospheric density due to relevant source processes such as thermal and photon-stimulated desorption, ion sputtering or micro meteoritic impact vaporization; as far as it concerns particle losses, it is necessary to include at least photo-ionization, being charge-exchange process negligible as a neutral loss mechanism Milillo et al. 2005; Mura et al. 2006b. Figure 46 shows an example of Monte Carlo modeling of the Hermean exosphere (based on Mura et al. 2007).

In Fig. 46, samples of exospheric vertical profiles related to various release processes are shown. TD produces a very dense exosphere, but at very low altitudes and only in the dayside. This process is not effective in global loss from the planet, since the fraction of particles that escape is well below 1% on average. In the case of PSD, the fraction of particles that are lost varies between 1% to 20% (Mura et al. 2007), while for IS it is found to be between 50% and 80%.

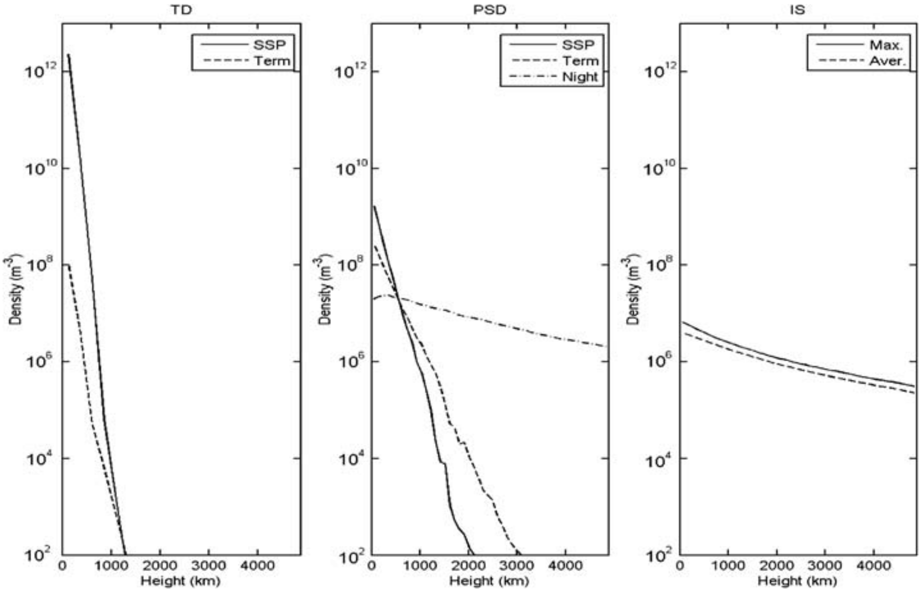

Fig. 47 Examples of Monte Carlo simulations of Na vertical profiles in the exosphere of Mercury. From the left: Thermal desorption (over sub-solar point (SSP) and over the terminator (Term)); Photon-stimulated desorption simulated using a Maxwellian-flux distribution with $T = 1{,}500$ K (over the sub-solar point, the terminator and over the anti-sun point (Night)); Ion-sputtering (over the point of maximum ion precipitation (Max) and averaged (Aver.) over all the dayside surface). Mercury–Sun distance is 0.38 AU, radiation pressure as estimated by Smyth and Marconi (1995) included. Adapted from Mura et al. (2007)

Figure 47 shows examples of Monte Carlo simulations of Na vertical profiles released from the surface due to thermal desorption, PSD and ion sputtering.

The Mercury exosphere simulations do provide significant background information, useful for the understanding of the "real" measurements which will be taken by the forthcoming in situ missions, like Messenger and BepiColombo. To deduce the physical meaning of these future observations, it could be worth deriving some functional forms—based on a best-fit approach of the available simulations—and link them to the basic physical exospheric parameters. In the future, such parameters could be properly tuned to best-fit the real data, and immediately provide a reliable signature of the planet's exospheric global characteristics.

In the simplified case of a surface with uniform concentration of a given component, the exospheric density generated from both PSD and TD has a cylindrical symmetry around the x axis (planet to Sun direction), and peaks at the sub-solar point. In this case, the vertical profile over this point can be reproduced by the simplified exospheric r-profile model (Rairden et al. 1986) by Chamberlain (1963) (first three terms of (28)). The angular dependence expressed by Rairden et al. (1986) for the Earth cannot be applied at Mercury since the Hermean exosphere is generated directly from the planet surface, and not from the exobase. Moreover, the radiation pressure acceleration can be very effective at Mercury (Smyth and Marconi 1995; Potter et al. 2002a), ranging from 0.2 to 2 m/s for Na, and from 0.3 to 3 m/s for K The remaining terms in (28) take into account the strong variation between day and night conditions, and describe the shape of the tail:

$$\log_{10}(n) = \underbrace{A + Be^{-C(r-1)} - \frac{r-1}{D}}_{\text{Raydern}} - \underbrace{\frac{F/r}{1+e^{-\frac{\alpha-\pi/2}{E}}}}_{\text{day/night modulation}} + \underbrace{G\left(1-e^{-I(r-1)}\right)e^{-\frac{1}{2}\left(\frac{\alpha-\pi}{H}\right)^2}}_{\text{radiation pressure effect}}, \quad (31)$$

where n is the density, α is the solar zenith angle (from the sub-solar point), r is the planetocentric distance. A through I are free parameters depending on the process involved (PSD or TD) and on boundary conditions (Mura et al. 2007); their values have been derived by best-fitting the outcomes from Monte Carlo numerical model previously described.

The shape of the exosphere generated from ion sputtering strongly depends on the ion precipitation pattern onto the surface. Recently, numerical models have taken into account the contribution of protons (Sarantos et al. 2001; Massetti et al. 2003; Kallio and Janhunen 2003; Mura et al. 2007; Leblanc and Johnson 2003), minor s/w components such as alpha particles (Leblanc and Johnson 2003) and planetary ions (Delcourt et al. 2003). According to most authors, in the case of s/w protons, we expect a proton precipitation flux up to 10^9 $\text{cm}^{-2}\,\text{s}^{-1}$ in the cusp regions, located in the dayside at mid latitudes. The flux, the shape and the relative size of these regions depend on the magnetospheric configuration. As stated before, the fraction of particles that escape from the planet is found between 50% and 80%.

Photoionization reduces, in general, the dayside exospheric density. Since the ionized particles are accelerated by the electromagnetic fields, this process produces a net loss from the planet. The estimated effect in exospheric profile, however, can be neglected.

Radiation pressure produces an increase of density in the nightside and a reduction in the dayside. This effect can be easily seen, for example, in the PSD exosphere, since particles generated by this release process have long residence time in ballistic trajectories (10^3–10^4 s); hence, they are efficiently accelerated in the anti-sunward direction.

7 Conclusions

The best-studied constituent in Mercury's exosphere, sodium, displays a rich variety in its spatial and temporal variability. Observations of this constituent have revealed a rapid variation in the ion sputtering component due to a variability in the magnetosphere, possible latitudinal and/or longitudinal variations in composition, long-term variations in photon-stimulated desorption and radiation pressure acceleration, long-term and short-term variations in meteoritic vaporization, and possible sequestration of volatiles on the nightside and at high latitudes. Observations of other species, both by Mariner 10 and by ground-based telescopes, are more sparse. A great wealth of information, both about the surface and about the interaction of high-energy radiation and particles with the surface, is expected to be gained with the advent of the two planned spacecraft, Messenger and BepiColombo, to the Hermean system. We expect to discover many more species in the exosphere in addition to the six currently known, but their expected relative abundances is widely debated. A comparison of simulated data with actual data from these spacecraft will allow us to test our current theories and revise them as appropriate. The abundances of the noble gases will tell us about processes from implantation of solar wind to the abundances in the deep interior. Asymmetries in the abundances of exospheric species will tell us not only how volatiles are sequestered and lost, but about the refractory species as well. We will undoubtedly be surprised by these discoveries, as all explorers have met with surprises in the past.

Acknowledgements A. Mura and H.I.M. Lichtenegger acknowledge support by the Europlanet project (http://www.europlanet-eu.org) for supporting working visits to the Space Science Institute of the Austrian Academy of Sciences in Graz, Austria and to the Istituto di Fisica dello Spazio Interplanetario-CNR, in Rome, Italy.

References

M.R. Aellig, A.J. Lazarus, J.T. Steinberg, in *Solar and Galactic Composition*, ed. by R.F. Wimmer-Schweingruber (2001)
M.A. A'Hearn, M.J.S. Belton, W.A. Delamere, J. Kissel, The Deep Impact Team, Science **310**, 258–264 (2005)
T.J. Ahrens, D.M. Cole, Proc. Lunar Sci. Conf. 5th, (1974), pp. 2333–2345
T.J. Ahrens, J.D. O'Keefe, Moon **4**, 214–249 (1972)
F. Aumayr, H. Winter, Phil. Trans. Roy. Soc. Lond. A **362**, 77–102 (2004)
C. Barbieri, S. Verani, G. Cremonese, A. Sprague, M. Mendillo, R. Cosentino, D. Hunten, Planet. Space Sci. **52**, 1169–1175 (2004)
A. Benninghoven, F.G. Rüdenauer, H.W. Werner, *Secondary Ion Mass Spectrometry: Basic Concepts, Instrumental Aspects, Applications and Trends* (Wiley, New York, 1987), 1227 pp
G. Betz, W. Husinsky, Phil. Trans. Roy. Soc. Lond. A **362**, 177–194 (2004)
T.A. Bida, R.M. Killen, T.H. Morgan, Nature **404**, 159–161 (2000)
D.T. Blewett, P.G. Lucey, B.R. Hawke, G.G. Ling, M.S. Robinson, Icarus **129**, 217–231 (1997)
V. Bothmer, R. Schwenn, Ann. Geophys. **16**, 1–24 (1998)
W.F. Bottke, A. Morbidelli, R. Jedicke, J.M. Petit, P. Levison, H.F. Michel, T.S. Metcalfe, Icarus **156**, 399–433 (2002)
A.L. Broadfoot, D.E. Shemansky, S. Kumar, Geophys. Res. Lett. **3**, 577–580 (1976)
M.E. Brown, Icarus **151**, 190–195 (2001)
P. Brown, R.E. Spalding, D.O. ReVelle, E. Tagliaferri, S.P. Worden, Nature **420**, 294–296 (2002)
T.H. Burbine, T.J. McCoy, L.R. Nittler, G.K. Benedix, E.A. Cloutis, T.L. Dickinson, Science **37**, 1233–1244 (2002)
B. Butler, D. Muhleman, M. Slade, J. Geophys. Res. **98**, 15,003–15,023 (1993)
M. Bruno, G. Cremonese, S. Marchi, Mon. Not. Roy. Astron. Soc. **1**, 1067–1071 (2006)
T.A. Cassidy, R.E. Johnson, Icarus **176**, 499–507 (2005)
J.W. Chamberlain, Planet. Space Sci. **11**, 901–960 (1963)
A. Ciaravella, J.C. Raymond, A. van Ballegooijen, L. Strachan, A. Vourlidas, J. Li, J. Chen, A. Panasyuk, Astrophys. J. **597**, 1118–1134 (2003)
M. Cintala, J. Geophys. Res. **97**, 947–973 (1992)
E.W. Cliver, O.C. St. Cyr, R.A. Howard, P.S. Mc Intosh, in *Solar Coronal Structures*, ed. by V. Rusin, J. Heinzel, C. Vial (VEDA Publishing House of the Slovak Academy of Sciences, 1994), pp. 83–89
C.M.S. Cohen, E.C. Stone, R.A. Mewaldt, R.A. Leske, G.M. Cummings, A.C. Mason, M.I. Desai, T.T. von Rosenvinge, M.E. Wiedenbeck, J. Geophys. Res. **110**, A09S16 (2005)
M.R. Combi, M.A. Disanti, U. Fink, Icarus **130**, 336–354 (1997)
J.E.P. Connerney, N.F. Ness, in *Mercury*, ed. by F. Vilas, C.R. Chapman, M.S. Matthews (University of Arizona Press, Tucson, 1988), pp. 494–513
S.R. Coon, W.F. Calaway, M.J. Pellin, J.M. White, Surf. Sci. **298**, 161–172 (1993)
J. Crank, *The Mathematics of Diffusion*, 2nd edn. (Oxford Univ. Press, Oxford, 1975)
G. Cremonese, H. Boehnhardt, J. Crovisier, H. Rauer, A. Fitzsimmons, M. Fulle, J. Licandro, D. Pollacco, G.P. Tozzi, R.M. West, Astrophys. J. Lett. **490**, L199–L202 (1997)
G. Cremonese, M. Bruno, V. Mangano, S. Marchi, A. Milillo, Icarus **177**, 122–128 (2005)
G. Cremonese, M. Bruno, V. Mangano, S. Marchi, A. Milillo, Icarus **182**, 297–298 (2006)
D.C. Delcourt, T.E. Moore, S. Orsini, A. Millilo, J.A. Sauvaud, Geophys. Res. Lett. **29** (2002). doi:10.1029/2001GL013829
D.C. Delcourt, S. Grimald, F. Leblanc, J.J. Berthelier, A. Millilo, A. Mura, S. Orsini, T.E. Moore, Ann. Geophys. **21**, 1723–1736 (2003)
R.C. Elphic, H.O. Funsten III, R.L. Hervig, Lunar Planet. Sci. Conf. Abst. **24**, 439 (1993)
G. Fjeldbo, A. Kliore, D. Sweetnam, P. Esposito, B. Seidel, T. Howard, Icarus **29**, 439–444 (1976)
B.C. Flynn, S.A. Stern, Icarus **124**, 530–536 (1996)
W.A. Gault, H.N. Rundle, Can. J. Phys. **47**, 85–98 (1969)
D.E. Gault, E.F. Horz, D.E. Brownlee, J.B. Hartung, Lunar. Planet Sci. Conf. **5**, 260 (1974)
M.V. Gerasimov, B.A. Ivanov, O.I. Yakovlev, Earth Moon Planet. **80**, 209–259 (1998)

H. Gnaser, W.O. Hofer, Appl. Phys. A **48**, 261–271 (1989)

B.E. Goldstein, S.T. Suess, R.J. Walker, J. Geophys. Res. **86**, 5485–5499 (1981)

N. Gopalswamy, in *The Sun and the Heliosphere as an Integrated system*, ed. by G. Poletto, S. Suess. ASSL Series (Kluwer, 2004), pp. 201–240

N. Gopalswamy, M.R. Kundu, Sol. Phys. **143**, 327–343 (1993)

N. Gopalswamy, S. Yashiro, M.L. Kaiser, R.A. Howard, J.L. Bougeret, J. Geophys. Res. **106**, 29,219–29,230 (2001a)

N. Gopalswamy, A. Lara, S. Yashiro, M.L. Kaiser, R.A. Howard, J. Geophys. Res. **106**, 29,207–29,218 (2001b)

N. Gopalswamy, A. Lara, S. Yashiro, R.A. Howard, Astrophys. J. **598**, L63–L66 (2003)

N. Gopalswamy, S. Nunes, S. Yashiro, R.A. Howard, Adv. Space Res. **34**(2), 391–396 (2004). doi:10.1016/j.asr.2003.10.054

C.S. Hansen, W.F. Calaway, B.V. King, M.J. Pellin, Surf. Sci. **398**, 211–220 (1998)

C.S. Hansen, W.F. Calaway, M.J. Pellin, B.V. King, A. Wucher, Surf. Sci. **432**, 199–210 (1999)

B. Hapke, J. Geophys. Res. **106**, 10,039–10,073 (2001)

R.A. Haring, A. Haring, F.W. Saris, A.A. de Vries, Appl. Phys. Lett. **41**, 174–176 (1982)

J.K. Harmon, Adv. Space Res. **19**, 1487–1496 (1997)

J.K. Harmon, M.A. Slade, Science **258**, 640–642 (1992)

J.K. Harmon, P.J. Perilat, M.A. Slade, Icarus **149**, 1–15 (2001)

G.B. Hasted, *Physics of Atomic Collisions* (Butterworths, London, 1964), p. 416

G. Heiken, D. Vaniman, B.M. French, *Lunar Sourcebook: A User's Guide to the Moon* (Cambridge Univ. Press, Cambridge, 1991)

T. Henke, J. Woch, U. Mall, S. Livi, B. Wilken, R. Schwenn, G. Gloeckler, R. von Steiger, R.J. Forsyth, A. Balogh, Geophys. Res. Lett. **25**, 3465–3468 (1998)

E. Hildner, J.T. Gosling, R.M. MacQueen, R.H. Munro, A.I. Poland, C.L. Ross, Sol. Phys. **48**, 127–135 (1976)

R.R. Hodges Jr., J. Geophys. Res. **79**, 2881–2885 (1974)

W.O. Hofer, in *Sputtering by Particle Bombardment*, ed. by R. Behrisch, R.K. Wittmaack (1991), pp. 15–90

L. Holmlid, J. Phys. Chem. **102**, 10,636–10,646 (1998)

L. Holmlid, Planet. Space Sci. **54**, 101–112 (2006)

L. Holmlid, J.O. Olsson, Surf. Sci. **67**, 61–76 (1977)

G.P. Horedt, G. Neukum, Icarus **60**, 710–717 (1984)

R.A. Howard, D. Michels, N.R. Sheeley, M.J. Koomen, in *The Sun and the Heliosphere in Three Dimensions*, ed. by R. Marsden, D. Reidel. ASSL, vol. 123 (Norwell, 1986), pp. 107–111

W.F. Huebner, J.J. Keady, S.P. Lyon, Astrophys. Space Phys. **195**, 1–294 (1992)

D.M. Hunten, A.L. Sprague, Adv. Space Res. **19**, 1551–1560 (1997)

D.M. Hunten, A.L. Sprague, Meteorit. Planet. Sci. **37**, 1191–1195 (2002)

D.M. Hunten, L.V. Wallace, Astrophys. J. **417**, 757–761 (1993)

D.M. Hunten, T.H. Morgan, D. Shemansky, in *Mercury*, ed. by F. Vilas, C.R. Chapman, M.S. Matthews (Univ. of Arizona Press, Tucson, 1988), pp. 562–612

A.P. Ingersoll, T. Svitek, B.C. Murray, Icarus **100**, 40–47 (1992)

W.H. Ip, Geophys. Res. Lett. **13**, 423–426 (1986)

W.H. Ip, Icarus **71**, 441–447 (1987)

W.H. Ip, Astrophys. J. **356**, 675–681 (1990)

W.H. Ip, A. Kopp, J. Geophys. Res. **07** (2002). doi:10.1029/2001JA009171

R.E. Johnson, Geophys. Monogr. **130**, 203–219 (2002)

K. Kabin, T.I. Gombosi, D.L. DeZeeuw, K.G. Powell, Icarus **143**, 397–406 (2000)

E. Kallio, P. Janhunen, Geophys. Res. Lett. **30**, (2003). doi:10.1029/2003GL017842

R.M. Killen, Meteorit. Planet. Sci. **37**, 1223–1231 (2002)

R.M. Killen, Publ. Astron. Soc. Pac. **118**, 1347–1353 (2006)

R.M. Killen, W.H. Ip, Rev. Geophys. **37**, 361–406 (1999)

R.M. Killen, T.H. Morgan, Icarus **101**, 294–312 (1993)

R.M. Killen, A.E. Potter, T.H. Morgan, Icarus **85**, 145–167 (1990)

R.M. Killen, A.E. Potter, T.H. Morgan, Science **252**, 474–475 (1991)

R.M. Killen, A.E. Potter, A. Fitzsimmons, T.H. Morgan, Planet. Space Sci. **47**, 1449–1458 (1999)

R.M. Killen, A.E. Potter, P. Reiff, M. Sarantos, B.V. Jackson, P. Hick, B. Giles, J. Geophys. Res. **106**, 20,509–20,526 (2001)

R.M. Killen, A.E. Potter, M. Sarantos, P. Reiff, Mercury, 25th Meeting of the IAU, Joint Discussion 2, Sydney, Australia, 2003. Meeting abstract

R.M. Killen, M. Sarantos, P.H. Reiff, Adv. Space Res. **33**, 1899–1904 (2004a)

R.M. Killen, M. Sarantos, A.E. Potter, P. Reiff, Icarus **171**, 1–19 (2004b)

R.M. Killen, T.A. Bida, T.H. Morgan, Icarus **173**, 300–311 (2005)
P.L. Koehn, A.L. Sprague, Planet. Space Sci. (2007). doi:10.1016/j.pss.2006.10.009
P.L. Koehn, T.H. Zurbuchen, K. Kabin, DPS Abstract, 35.2308, 2003
A. Kotarba, I. Kruk, Z. Sojka, J. Catal. **221**(2), 650–652 (2004)
G.A. Krasinsky, E.V. Pitjeva, M.V. Vasilyev, E.I. Yagudina, Icarus **158**, 98–105 (2002)
H. Lammer, P. Wurz, M.R. Patel, R. Killen, C. Kolb, S. Massetti, S. Orsini, A. Milillo, Icarus **166**, 238–247 (2003)
A. Lara, J.A. González-Esparza, N. Gopalswamy, Geofísica Internacional **43**, 75–82 (2004)
F. Leblanc, R.E. Johnson, Icarus **164**, 261–281 (2003)
F. Leblanc, D. Delcourt, R.E. Johnson, J. Geophys. Res. **108**, (2003a). doi:10.1029/2003JE002151
F. Leblanc, J.G. Luhmann, R.E. Johnson, M. Liu, Planet. Space Sci. **51**, 339–352 (2003b)
F. Leblanc, C. Barbieri, G. Cremonese, S. Verani, R. Cosentino, M. Mendillo, A. Sprague, D. Hunten, Icarus **185**, 395–402 (2006)
S.T. Lepri, T.H. Zurbuchen, L.A. Fisk, I.G. Richardson, H.V. Cane, G. Gloeckler, J. Geophys. Res. **106**, 29,231–29,238 (2001)
G.M. Lindsay, J.G. Luhmann, C.T. Russell, J.T. Gosling, J. Geophys. Res. **104**, 12515–12524 (1999)
K. Lodders, B. Fegley, *The Planetary Scientists Companion* (Oxford University Press, 1998)
J.G. Luhmann, C.T. Russell, N.A. Tsyganenko, J. Geophys. Res. **103**, 9113–9119 (1998)
A.V. Lukyanov, S. Barabash, R. Lundin, P. C:son Brandt, Planet. Space Sci. **49**, 1677–1684 (2001)
T.E. Madey, B.V. Yakshinskiy, V.N. Ageev, R.E. Johnson, J. Geophys. Res. **103**, 5873 (1998)
A. Mallama, D. Wang, R.A. Howard, Icarus **155**, 253–264 (2002)
V. Mangano, A. Milillo, S. Orsini, A. Mura, H. Lammer, P. Wurz, EGU Abstract, EGU05-A-01247, 2005
V. Mangano, A. Milillo, A. Mura, S. Orsini, E. De Angelis, A.M. Di Lellis, P. Wurz, Planet. Space Sci. (2007). doi:10.1016/j.pss.2006.10.008
S. Marchi, A. Morbidelli, G. Cremonese, Astron. Astrophys. **431**, 1123–1127 (2005)
G.M. Mason, J.E. Mazur, J.R. Dwyer, Astrophys. J. **525**, L133–L136 (1999)
S. Massetti, S. Orsini, A. Milillo, A. Mura, E. De Angelis, H. Lammer, P. Wurz, Icarus **166**, 229–237 (2003)
S. Massetti, S. Orsini, A. Milillo, A. Mura, Planet. Space Sci. (2007). doi:10.1016/j.pss.2006.12.008
M.A. McGrath, R.E. Johnson, L.J. Lanzerotti, Nature **323**, 696–696 (1986)
A.S. Milillo, S. Orsini, P. Wurz, D. Delcourt, E. Kallio, H. Rillen, R.M. Lammer, S. Massetti, A. Mura, S. Barabash, G. Cremonese, I.A. Daglis, E. De Angelis, A.M. Di Lellis, S. Livi, V. Mangano, K. Torka, Space Sci. Rev. **117**, 397–444 (2005)
A. Morbidelli, B. Gladman, Meteorit. Planet. Sci. **33**, 999–1016 (1998)
T.H. Morgan, R.M. Killen, Planet. Space Sci. **45**, 81–94 (1997)
T.H. Morgan, H.A. Zook, A.E. Potter, Icarus **74**, 156–170 (1988)
A. Mura, Neutral Atom Emission from Mercury Magnetosphere. AOG, Conference. Singapore, June 20–24, 2005
A. Mura, S. Orsini, A. Milillo, D. Delcourt, S. Massetti, E. De Angelis, Icarus **175**, 305–319 (2005)
A. Mura, S. Orsini, A. Milillo, A.M. Di Lellis, E. De Angelis, Planet. Space Sci. **54**, 144–152 (2006a)
A. Mura, S. Orsini, A. Milillo, D. Delcourt, A.M. Di Lellis, E. De Angelis, S. Massetti, Adv. Geosci. **3** (2006b). ISBN 981-256-983-8
A. Mura, D. Delcourt, S. Massetti, A. Milillo, S. Orsini, A. Di Lellis, E. De Angelis, Geophysical Research Abstracts, vol. 8, 06958, EGU General Assembly, Vienna (Austria), 2–7 April (2006c)
A. Mura, A. Milillo, S. Orsini, S. Massetti, Planet. Space Sci. (2007). doi:10.1016/j.pss.2006.11.028
N.F. Ness, K.W. Behannon, R.P. Lepping, Y.C. Wang, Nature **255**, 204–205 (1975)
H. Oechsner, H. Schoof, E. Stumpe, Surf. Sci. **76**, 343–354 (1978)
J.D. O'Keefe, T.J. Ahrens, Science **234**, 346–349 (1986)
D.A. Paige, S.E. Wood, A.R. Vasavada, Science **258**, 643–646 (1992)
A.E. Potter, Geophys. Res. Lett. **22**, 3289–3292 (1995)
A.E. Potter, T.H. Morgan, Science **229**, 651–653 (1985)
A.E. Potter, T.H. Morgan, Icarus **67**, 336–340 (1986)
A.E. Potter, T.H. Morgan, Icarus **71**, 472–477 (1987)
A.E. Potter, T.H. Morgan, Science **241**, 675–680 (1988)
A.E. Potter, T.H. Morgan, Science **248**, 835–838 (1990)
A.E. Potter, T.H. Morgan, Planet. Space Sci. **45**, 95–100 (1997)
A.E. Potter, R.M. Killen, T.H. Morgan, Space Sci. **47**, 1141–1148 (1999)
A.E. Potter, C.M. Anderson, R.M. Killen, T.H. Morgan, J. Geophys. Res. Planets **107** (2002a). doi:10.1029/2000JE0014937
A.E. Potter, R.M. Killen, T.H. Morgan, Meteorit. Planet. Sci. **37**, 1165–1172 (2002b)
A.E. Potter, R.M. Killen, M. Sarantos, Icarus **181**, 1–12 (2006). doi:10.1016/j.icarus.2005.10.026
A.E. Potter, R.M. Killen, T.H. Morgan, Icarus **186**(2), 571–580 (2007)

R.L. Rairden, L.A. Frank, J.D. Craven, J. Geophys. Res. **91**(A12), 13613–13630 (1986)
D.V. Reames, S.W. Kahler, C.K. Ng, Astrophys. J. **491**, 414–420 (1997)
F.J.M. Rietmeijer, *Advanced Mineralogy* (Springer, Berlin, 1998), pp. 22–28
M. Sarantos, *Ion Trajectories in Mercury's Magnetosphere*, PhD thesis (Rice University, Houston, 2005)
M. Sarantos, P.H. Reiff, T.H. Hill, R.M. Killen, A.L. Urquhart, Planet. Space Sci. **49**, 1629–1635 (2001)
M. Sarantos, R.M. Killen, D. Kim, Planet. Space Sci. (2007). doi:10.1016/j.pss.2006.10.011
H. Schleicher, G. Wiedemann, H. Wohl, T. Berkefeld, D. Soltau, Astron. Astrophys. **425**, 1119–1124 (2004)
N. Sheeley, R.A. Howard, M.J. Koomen, D.J. Michels, Astrophys. J. **272**, 349–354 (1983)
D.E. Shemansky, Mercury Messenger **2**, 1 (1988)
D.E. Shemansky, *AIP Conf. Proc. 63, Rarefied Gas Dynamics 23rd Intl. Symposium*, 2003, p. 687
D.E. Shemansky, T.H. Morgan, Geophys. Res. Lett. **18**, 1659–1662 (1991)
E.M. Sieveka, R.E. Johnson, Astrophys. J. **287**, 418–426 (1984)
P. Sigmund, Phys. Rev. **184**, 383–416 (1969)
G. Siscoe, L. Christopher, Geophys. Res. Lett. **2**, 158–160 (1975)
M. Slade, B. Butler, D. Muhleman, Science **258**, 635–640 (1992)
G.R. Smith, D.E. Shemansky, A.L. Broadfoot, L. Wallace, J. Geophys. Res. **83**, 3783–3790 (1978)
W.H. Smyth, M.L. Marconi, Astrophys. J. **441**, 839–864 (1995)
A.L. Sprague, J. Geophys. Res. **97**, 18257–18264 (1992)
A.L. Sprague, T.L. Roush, Icarus **133**, 174–183 (1998)
A.L. Sprague, R.W.H. Kozlowski, D.M. Hunten, Science **249**, 1140–1142 (1990)
A.L. Sprague, R.W.H. Kozlowski, D.M. Hunten, F.A. Grosse, Icarus **104**, 33–37 (1993)
A.L. Sprague, R.W.H. Kozlowski, F.C. Witteborn, D.P. Cruikshank, D.H. Wooden, Icarus **109**, 156–167 (1994)
A.L. Sprague, D.M. Hunten, K. Lodders, Icarus **118**, 211–215 (1995)
A.L. Sprague, D.M. Hunten, F.A. Grosse, Icarus **123**, 345–349 (1996)
A.L. Sprague, R.W.H. Kozlowski, D.M. Hunten, N.M. Schneider, D.L. Domingue, W.K. Wells, W. Schmitt, U. Fink, Icarus **129**, 506–527 (1997)
A.L. Sprague, W.J. Schmitt, R.E. Hill, Icarus **136**, 60–68 (1998)
A.L. Sprague, J.P. Emery, K.L. Donaldson, R.W. Russell, D.K. Lynch, A.L. Mazuk, Meteorit. Planet. Sci. **37**, 1255–1268 (2002)
L.V. Starukhina, Proc. Lunar Planet. Sci. Conf. **31**, 1301 (2000)
R.F. Stebbings, C.H. Smith, H. Ehrahardt, J. Geophys. Res. **69**, 2349 (1964)
O.C. St. Cyr, R.A. Howard, N.R. Sheeley Jr., S.P. Plunkett, D.J. Michels, S.E. Paswaters, M.J. Koomen, G.M. Simnett, B.J. Thompson, J.B. Gurman, R. Schwenn, D.F. Webb, E. Hildner, P.L. Lamy, J. Geophys. Res. **105**, 18169–18185 (2000)
J. Von Neumann, *Various Techniques Used in Connection with Random Digits*. National Bureau of Standard Applied Mathematics Series, vol. 12. (1951), pp. 36–38
A. Vourlidas, D. Buzasi, R.A. Howard, E. Esfandiari, in *Solar Variability: From Core to Outer Frontiers*, ed. by A. Wilson, ESA SP-506 (ESA Publication, Noordwijk, 2002), pp. 91–94
J. Warell, Icarus **161**, 199–222 (2003)
J. Warell, D.T. Blewett, Icarus **168**, 257–276 (2004)
D.F. Webb, R.A. Howard, J. Geophys. Res. **99**, 4201–4220 (1994)
M.E. Wiedenbeck et al., AGU Fall Mtg 2005, abstract SH11B-0267
R.C. Wiens, D.S. Burnett, W.F. Calaway, C.S. Hansen, K.R. Kykkem, M.L. Pellin, Icarus **128**, 386–397 (1997)
H.F. Winters, J.W. Coburn, Surf. Sci. Rep. **14**(3), 161–269 (1992)
H.F. Winters, J.W. Coburn, T.J. Chuang, J. Vac. Sci. Technol. B **1**(2), 469–480 (1983)
A. Wucher, H. Oechsner, Nucl. Instr. Methods **B18**, 458–463 (1986)
P. Wurz, in *The Dynamic Sun: Challenges for Theory and Observations*. ESA SP-600 (2005), pp. 5.2, 1-9
P. Wurz, H. Lammer, Icarus **164**, 1–13 (2003)
P. Wurz, W. Husinsky, G. Betz, in *Symposium on Surface Science*, ed. by J.J. Launois, B. Mutaftschiev, M.R. Tempère (La Plagne, France, 1990), pp. 181–185
P. Wurz, W. Husinsky, G. Betz, Appl. Phys. A **52**, 213–217 (1991)
P. Wurz, R.F. Wimmer-Schweingruber, K. Issautier, P. Bochsler, A.B. Galvin, F.M. Ipavich, *Composition of Magnetic Cloud Plasmas During 1997 and 1998*. CP-598 (American Institute Physics on Solar and Galactic Composition, 2001), pp. 145–151
P. Wurz, R. Wimmer-Schweingruber, P. Bochsler, A. Galvin, J.A. Paquette, F. Ipavich, in *Solar Wind X* (American Institute Physics, 2003), pp. 679, 685–690
P. Wurz, U. Rohner, J.A. Whitby, C. Kolb, H. Lammer, P. Dobnikar, J.A. Martín-Fernández, Icarus (2007). doi:10.1016/j.icarus.2007.04.034
B.V. Yakshinskiy, T.E. Madey, Nature **400**, 642–644 (1999)

B.V. Yakshinskiy, T.E. Madey, Icarus **168**, 53–59 (2004)

S. Yashiro, N. Gopalswamy, G. Michalek, O.C. St. Cyr, S.P. Plunkett, N.B. Rich, R.A. Howard, *J. Geophys. Res.* **109**(A7) (2004). doi:10.1029/2003JA010282

J. Zhang, K.P. Dere, R.A. Howard, M.R. Kundu, S.M. White, Astrophys. J. **559**, 452–642 (2001)

J.F. Ziegler, J.P. Biersack, *TRIM and SRIM Program Version SRIM-2003.26* (Pergamon, New York, 1985). http://www.srim.org/